INFORMATION TO USERS

This manuscript has been reproduced from the microfilm master. UMI films the text directly from the original or copy submitted. Thus, some thesis and dissertation copies are in typewriter face, while others may be from any type of computer printer.

The quality of this reproduction is dependent upon the quality of the copy submitted. Broken or indistinct print, colored or poor quality illustrations and photographs, print bleedthrough, substandard margins, and improper alignment can adversely affect reproduction.

In the unlikely event that the author did not send UMI a complete manuscript and there are missing pages, these will be noted. Also, if unauthorized copyright material had to be removed, a note will indicate the deletion.

Oversize materials (e.g., maps, drawings, charts) are reproduced by sectioning the original, beginning at the upper left-hand corner and continuing from left to right in equal sections with small overlaps.

Photographs included in the original manuscript have been reproduced xerographically in this copy. Higher quality 6" x 9" black and white photographic prints are available for any photographs or illustrations appearing in this copy for an additional charge. Contact UMI directly to order.

Bell & Howell Information and Learning
300 North Zeeb Road, Ann Arbor, MI 48106-1346 USA
800-521-0600

UMI®

DISSERTATION

TEMPLATE SYNTHESIS AND CHARACTERIZATION OF NANOSTRUCTURED LITHIUM INSERTION ELECTRODES AND NANOGOLD/POROUS ALUMINUM OXIDE COMPOSITE MEMBRANES

Submitted by

Charles J. Patrissi

Department of Chemistry

In partial fulfillment of the requirements

for the Degree of Doctor of Philosophy

Colorado State University

Fort Collins, CO 80523

Summer 2000

COLORADO STATE UNIVERSITY

June 23, 2000

WE HEREBY RECOMMEND THAT THE DISSERTATION PREPARED UNDER OUR SUPERVISION BY CHARLES J. PATRISSI ENTITLED "TEMPLATE SYNTHESIS AND CHARACTERIZATION OF NANOSTRUCTURED LITHIUM INSERTION ELECTRODES AND NANOGOLD/POROUS ALUMINUM OXIDE COMPOSITE MEMBRANES" BE ACCEPTED AS FULFILLING IN PART REQUIREMENTS FOR THE DEGREE OF DOCTOR OF PHILOSOPHY.

Committee on Graduate Work

Adviser

Department Head/Director

ABSTRACT OF DISSERTATION

TEMPLATE SYNTHESIS AND CHARACTERIZATION OF NANOSTRUCTURED LITHIUM INSERTION ELECTRODES AND NANOGOLD/POROUS ALUMINUM OXIDE COMPOSITE MEMBRANES

A membrane-based template synthesis method was used to prepare nanostructured Li-ion battery electrodes and nanogold/porous aluminum oxide composite membranes. Membrane-based template synthesis is a general method for the preparation of nanomaterials which entails deposition of the material of interest, or a suitable precursor, within the nanometer-diameter pores in a porous template membrane. This method allows for control of nanoparticle size and shape and is compatible with many methods of synthesis for bulk materials. The template membranes used in this work were commercially available porous polycarbonate filtration membranes and nanoporous aluminum oxide membranes that were prepared in-house.

Nanostructured electrodes of orthorhombic V_2O_5, prepared using membrane-based template synthesis, were used to investigate the effects of Li-ion diffusion distance and V_2O_5 surface area on electrode rate capability. Nanowires of V_2O_5 were prepared by depositing a precursor in the pores of microporous polycarbonate filtration membranes. The result was an ensemble of

115 nm diameter, 2 μm long nanowires of V_2O_5 which protruded from a V_2O_5 surface layer like the bristles of a brush. The Li^+ storage capacity of the nanostructured electrode was compared to a thin film control electrode at high discharge rates. Results show that the nanostructured electrode delivered three to four times the capacity of the thin film electrode at discharge rates above 500C.

A membrane based template synthesis method was also used to prepare crystalline V_2O_5 electrodes which have high volumetric charge capacities, at high discharge rates, compared to a thin-film control electrode. In order to obtain high volumetric rate capability, the as-received polycarbonate template membranes were chemically etched to increase membrane porosity. Nanofibrous electrodes of crystalline V_2O_5 were then prepared by depositing an alkoxide precursor in the pores of the etched membranes. Electrode volumetric capacity was further increased by addition of the V_2O_5 precursor to the parent nanostructured electrodes. Results on the volumetric and geometric rate capabilities and the cycling performance of these electrodes are presented.

Finally, nanogold was electrochemically deposited in porous aluminum oxide template membranes to study the effect of temperature on the shape and optical properties of the gold nanoparticles. Low aspect ratio nanoparticles were observed, via electron microscopy, to be thin skinned, flakes of Au within the pores. After heat treatment at temperatures well below the melting point of gold (< 400 C) these particles changed shape to become nearly spherical. Visually, the color of these membranes changed from blue to red after the heat treatment.

In contrast, the nanoparticles with an aspect ratio of ca. 3 showed essentially no detectable change in shape or optical properties after exposure to the same heating program. The membranes started red and did not change color with heating.

Charles J. Patrissi

Chemistry Department

Colorado State University

Fort Collins, CO 80523

Summer 2000

DEDICATION

To my parents, Frances O. and Daniel J. Patrissi, for their encouragement, understanding, inspiration and CARE packages.

ACKNOWLEDGMENTS

I am indebted to many individuals who helped shape the course of my research at CSU.

Prof. Charles R. Martin provided the ideas that were the foundation of my projects. In addition, I appreciate the independence and patience that Chuck affords all of his students. Professors Peter Dorhout and Steve Strauss provided much needed instrumental support and scientific consultations for which I am very grateful. I was fortunate to work with Professors Ellen Fisher, Dave Grainger and Nancy Levinger who were both professional and supportive. Dr. Robert Lee and Dr. John Chandler are extremely patient and competent teachers who "taught me all I know" about electron microscopy and worked hard to keep the equipment in excellent shape.

I was lucky to have some great teammates and role models in the Martin lab. Veronica Cepak, Kshama Jirage, and David Mitchell, Naichao Li, Jae-Min Hong, Yoshio Kobayashi, Ranjani Parthasarathy and Vinod Menon are creative scientists who also know the value of cooperation.

Matsuhiko Nishizawa was instrumental in helping start the V_2O_5 work. In 1996 I knew little about insertion compounds or performing electrochemical experiments on Li-insertion compounds in an inert atmosphere. Matsuhiko helped me get a great start on the project that was to become the main focus of this dissertation.

Louis Hornyak, John Hulteen, Elizabeth Oberhauser, and David Minor were critical to my success with the nanogold project. I am especially grateful to Louis for showing me the practical aspects of membrane-based template synthesis and also for some timely comments regarding my first few seminars.

Finally, my family and friends helped me keep a positive attitude. My parents and sisters, Carol, Jane and Sue, and their families were a constant source of support and needed diversion. One of the unexpected benefits of graduate school was forming what I hope will be long-lasting friendships with many students and faculty, especially Lori Wernersbach, Dale Willard, Tom Wynn, Laura Inman Sharp, Francois Pichot, Murielle and Tom Brewer and Kshama Jirage. Last but not least, who could help me keep perspective on things better than the boys from the Park.

Many thanks to all of you.

TABLE OF CONTENTS

LIST OF FIGURES

CHAPTER 1

INTRODUCTION

The field of nanomaterials focuses on the preparation, study, and application of materials with at least one dimension less than 100 nm.[1,2] In his lecture "There's plenty of room at the bottom", Richard Feynman foresaw the enormous potential of nanomaterials in science and technology.[3] Since then it has been shown that reducing the particle size of a material toward molecular dimensions can significantly change its chemical and physical properties from that of bulk material.

The goals of this dissertation research were to explore the rate capability of nanostructured lithium-ion battery electrodes and the thermal properties of nanogold/aluminum oxide composites. The method used to prepare these nanostructured materials is called "membrane-based template synthesis". The nanostructured lithium-ion battery electrodes studied in Chapters 2 and 3 had particles sizes ranging from 115 nm to 1 μm. In Chapter 5, nanometer-sized particles of gold were prepared within a porous aluminum oxide host. The nanostructures in both projects were expected to possess unique properties based on their size.

The remainder of Chapter 1 is divided into three sections which provide background information on membrane-based template synthesis, Li-ion batteries

and vanadium pentoxide. Membrane-based template synthesis (section 1) was the method used to prepare the nanostructured materials for this dissertation. This method is widely used to prepare nanostructured materials of controlled dimensions and shape. Membrane-based template synthesis entails deposition of the material of interest, or a suitable precursor, within the pores of a nanoporous host. The size and shape of the resulting nanomaterial is a function of pore diameter and the conditions used for deposition. This section describes the general concept of template synthesis with special attention given to the properties of the templates used for this work. Finally, examples of membrane-based template synthesis in the preparation, study and application of nanostructured materials are presented.

Section 2 discusses the important theoretical and practical aspects of lithium-ion battery performance. Specifically, this section shows how battery performance depends on the choice of electrode material, on the size of the electrode material particles, and on electrode morphology. This is background information for Chapters 3 and 4 which use nanostructured electrodes to study the effect of particle size and shape on energy output at high discharge current.

Finally, vanadium pentoxide, V_2O_5, was the model compound chosen for the studies combining nanomaterials and Lithium-ion batteries (Chapters 2 and 3). V_2O_5 is a well-characterized Li-insertion compound because of its technological importance as an electrode material in lithium and lithium–ion batteries. This section presents the important aspects of V_2O_5 with respect to electrochemical lithium insertion and lithium diffusion.

In Chapter 2, membrane-based template synthesis was used to prepare nanostructured electrodes of V_2O_5. These electrodes consist of 115 nm diameter, 2 μm long fibrils of V_2O_5 protruding from a Pt foil current collector like the bristles of a brush. It is well known that the size of the insertion material particles in the electrodes critically affects electrode energy output at high discharge currents. These nanoengineered electrodes were used for a quantitative study of insertion material particle size on electrode rate capability. The data show that the specific energy output ($Wh \bullet g^{-1} V_2O_5$) of the nanostructured V_2O_5 was four times higher than for thin-film V_2O_5 control electrodes. The thin film represents a more conventional morphology used in battery electrodes.

Chapter 3 describes the preparation of nanostructured V_2O_5 electrodes which deliver high volumetric energy density at high discharge currents. While the electrodes prepared in Chapter 2 have high *specific* energy output, the volumetric density is low. This is because of the low porosity of the template membranes used in this project. To overcome this problem, the template membranes were chemically etched to increase pore diameter and total membrane pore volume. Using these membranes, high energy density, V_2O_5 electrodes were prepared. These electrodes showed a higher volumetric capacity than the thin-film electrodes at high discharge currents. The intended application of the nanostructured V_2O_5 is as an electrode in high rate lithium and lithium-ion microbatteries.

Chapter 4 shows the change in shape and optical properties of nano-

particles of gold due to low-temperature melting. In this project, gold nanoparticles were electrochemically deposited within the pores of an aluminum oxide template membrane with pores that were nominally 45 nm in diameter. The aspect ratio of the gold particles was varied by controlling the amount of charge passed during the deposition process. Low aspect ratio nanoparticles were observed with transmission electron microscopy (TEM) to be high surface area, flat flakes of Au within the pores. After heat treatment at up to 400 °C they change shape to become more dense, nearly spherical particles. Visually the nanogold/alumina membranes change from blue to red after the thermal treatment. TEM revealed that the thermal treatment changed the size and shape of the gold nanoparticles. In contrast, nanoparticles with aspect ratios of approximately 3 show no color change from thermal treatment. The nanogold/alumina composites were initially red and stayed red after heating. TEM analysis was not able to detect a change in the size or the shape of the nanoparticles due to heating.

MEMBRANE-BASED TEMPLATE SYNTHESIS OF NANOMATERIALS

Introduction. Template synthesis is a general method for the preparation of nanomaterials.[2,4-7] In the template method, the material of interest, or a suitable precursor, is deposited within the nanometer-sized cavities of a host. Thus, the size and shape of the nanomaterial depends on the dimensions of the nanocavities in the host template. If desired, the template may be removed after deposition to allow investigation or integration of the nanomaterial. The method

is termed "general" because nearly any chemical synthesis method used to prepare bulk materials can be adapted so that the synthesis occurs within the cavities of the template. These methods include chemical vapor deposition,[8-10] electrochemical[11-13] and electroless[14,15] deposition, chemical[16] and electrochemical polymerization,[17] and sol-gel chemistry.[18,19]

Membrane-based template synthesis was the method used to prepare the nanomaterials discussed in this dissertation. This method entails deposition of the desired material within nanometer diameter pores in polymeric or inorganic filtration membranes. Reviews of template synthesis[7] and membrane-based template synthesis[2,5,20] can be found elsewhere. What follows illustrates the concept of template synthesis and its usefulness in the preparation, study and application of nanostructured materials. First, a general description of template synthesis is presented showing the categories of templates used in this method. This is followed by information on the membranes used to prepare the nanomaterials for this work. The final section shows selected applications of membrane-based template synthesis.

Categories of Templates. Templates used in this method can be categorized as 1-D (tunnel), 2-D (layered), or 3-D (framework) hosts.[7] Examples of three-dimensional templates are porous glasses. These materials are characterized by a network of monodisperse pores. Pores range from 10 to 50 nm in diameter and their porosities are approximately 25%.[21] Porous glasses have been used in the development of sensors,[22] catalysts[23] and for the investigations of the properties of materials in confined geometries.[24] For

example, work on indium in porous Vycor glass showed that the superconductivity transition temperature was increased by 20% over bulk material.[25] This enhanced T_c is believed to arise from the large surface to volume ratio of the indium nanoparticles. For similar reasons, cryogenic fluids confined in porous glasses have melting and freezing points significantly below the temperature of the non-confined materials.[26]

Two-dimensional templates are inorganic and organic layered hosts, such as Langmuir Blodgett films[27] and clays.[28,29] Montmorillonite clay is a layered mineral that has been used to prepare highly oriented graphite powders and films. Kyotani and Tomita[30] polymerized gaseous acrylonitrile between the layers using γ-ray radiation. The resulting polymer was heat treated under argon and subsequent removal of the template with HF resulted in a powder consisting of 2-dimensional graphite platelets. More recently, Kumizuka et al.[31] formed a continuous film of highly oriented graphite using a phosphate-treated montmorillonite. The film was prepared by casting an aqueous dispersion of clay and a cationic copolymer on a fluorocarbon membrane filter. Because of the phosphate treatment, the positively charged copolymer was readily incorporated between the layers. The polymer/clay composite was dried at ambient temperature, removed from the fluorocarbon filter and subsequently carbonized. The clay was removed with HF to obtain a black, flexible, freestanding film. After thermal treatment, X-ray diffraction showed that the platelets adopted a preferred orientation with their c-axes perpendicular to the film surface. Thus, template synthesis between the layers of the clay resulted in a highly oriented, thin (200

μm thick) film of graphite. Possible applications of these films are in electromagnetic shielding and as electrode materials for lithium-ion batteries.

Examples of one-dimensional templates are carbon nanotubes,[32,33] zeolites,[34], nanochannel glass,[35,36] and polymeric microspheres.[37,38] The nanoporous polycarbonate and aluminum oxide template membranes used to prepare the nanostructures in Chapters 2 through 4 are also examples of one-dimensional hosts. They have been used extensively for the preparation of nanostructured metals,[11,13,39,40] semiconductors,[18] polymers,[17] and carbon.[8,16,33] These membranes are characterized by cylindrical pores (tunnels) that extend through the entire thickness of the membrane. Figure 2.1 shows scanning electron micrographs of the surfaces of these membranes. Because of the cylindrical shape of the pore, a cylindrical nanofiber or nanotube can be obtained depending on the conditions and deposition method. In addition, nanoparticle aspect ratio can be varied by controlling the amount of the material deposited. The pores in these membranes have a narrow pore diameter distribution which is important for quantitative studies on the effects of particle size on nanomaterial properties. Figure 1.1 shows that the aluminum oxide membranes have a much higher porosity than their polycarbonate counterparts. The pore volume of the aluminum oxide membranes is between 30 and 50% of the total membrane volume while the porosity the polycarbonate membranes is between 1 and 12%. Template porosity is important where the volumetric density of the nanomaterial is critical. This was a concern in the preparation of

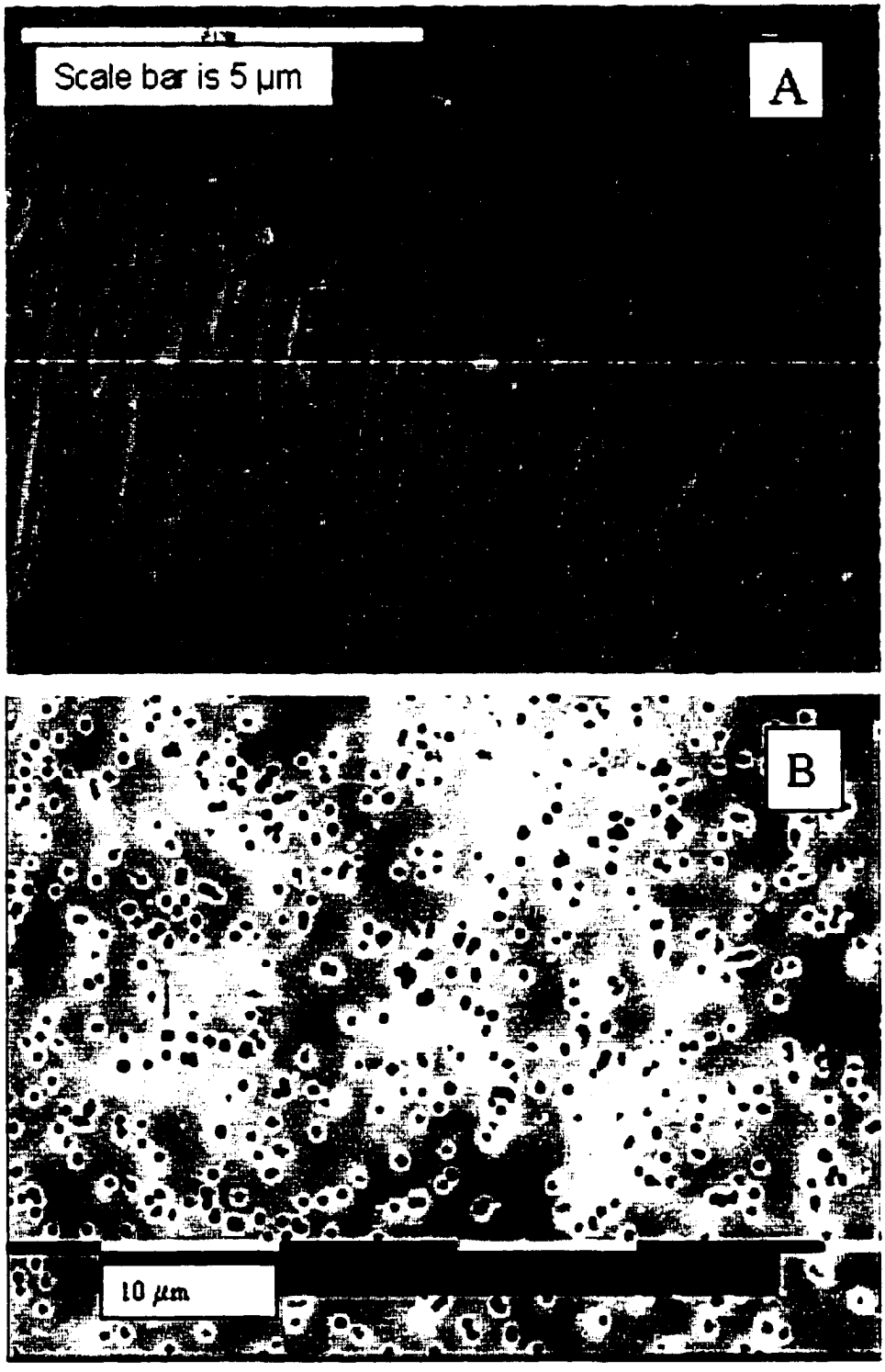

Figure 1.1. Scanning electron micrographs of microporous aluminum oxide (A) and microporous polycarbonate (B) template membranes. The nominal pore diameters in these membranes are 220 nm for alumina and 600 nm for polycarbonate. Figure 1.1A is courtesy of Mr. David Mitchell.

the nanostructured microbattery electrodes in Chapter 3.

Microporous polycarbonate filtration membranes were used for the membrane-based template synthesis of nanostructured vanadium pentoxide cathodes in Chapters 2 and 3. Vanadium pentoxide is well known for its lithium insertion properties and is used as a cathode material in lithium and lithium-ion batteries.[41] The capacity of insertion electrodes at high discharge current critically depends on the diameter of the Li-insertion particles in the electrodes. Membrane-based template synthesis was used to prepare nanofibrous electrodes of V_2O_5. The resulting nanofibers were between 115 nm and 1 μm in diameter, 2 μm to 8 μm long and protruded from a Pt current collector surface like the bristles of a brush. These electrodes were used to study the effect of V_2O_5 particle size on electrode capacity at high discharge current.

In chapter 4, nanoporous aluminum oxide membranes were used as templates for the preparation of nanometer sized particles of gold within the template. The optical absorbance of nanogold is directly related to particle diameter and aspect ratio. Nanoporous alumina was selected for this work because its high optical transmittance (between 400 and 800 nm) and good thermal stability permitted characterization of the optical absorbance changes of the nanogold due to melting at low (< 400 °C) temperatures.

Microporous Polycarbonate Template Membranes. The microporous polymeric template membranes used in Chapters 2 and 3 are sold commercially as filtration membranes (Osmonics, Livermore, CA). They are prepared using a two-step track-etch process.[42] The track-etch process entails exposing a

nonporous polycarbonate sheet to high-energy nuclear fission fragments to create damage tracks. The damage tracks consist of broken polymer chains and free radicals. The number of tracks per square centimeter depends on exposure time. The exposed material is then chemically etched and pores form along the damage tracks because of the faster rate of dissolution for the shorter chains. Pore diameter is controlled by chemical etch time. Polycarbonate membranes are available with nearly monodisperse pore diameters between 10 nm and 20 μm while membrane thicknesses vary between 6 and 11 μm.

Because the fission fragments are not collimated, the damage tracks form at angles normal to the membrane surface. The angled damage tracks result in pore tilt angles as low as 34° with respect to the membrane surface. The consequence is that two or more pores can merge together creating a network of interconnected pores.

Membranes used for the preparation of the nanostructured V_2O_5 electrodes were polycarbonate; however the track-etch process can also be used to prepared membranes from other materials, such as polyester and mica.[43] Removal of the template is an important consideration where the nanomaterial must be freed from the membrane for a particular study or application. Polymeric templates can be removed by solvent dissolution or decomposition either in an oxygen plasma or at high temperatures in air.

Microporous Aluminum Oxide Templates. Anodization of aluminum to obtain porous oxides is a well-established technique and has been reported extensively in the literature.[44-47] Nanoporous aluminum oxide can be obtained

by anodizing aluminum in an aqueous electrolyte of polyprotic acids at constant voltage. During the electrolytic growth step, pore diameter and membrane thickness are controlled by proper selection of anodization voltage and total charge passed, respectively. Membrane pore diameters are between 10 nm and 250 nm with membrane thicknesses as large as 100 μm.[48] Current density is also critical to the ordering of the pores[44] and is controlled by proper selection of four variables: electrolyte concentration, electrolyte temperature, applied voltage, and type of acid. After the growth step, free-standing, aluminum oxide templates can be removed from the aluminum using a process known as voltage reduction.[49]

Figure 1.1A shows a scanning electron micrograph of a microporous alumina template membrane prepared in the Martin research lab. These materials are characterized by a parallel arrangement of cylindrical pores that extend through the membrane thickness. Note that the pores are not tilted with respect to the surface normal and that they do not interconnect. These properties are important where nanoparticle orientation and isolation are important, as in studies on the optical properties of nanogold particles in Chapter 4.

The pore density in alumina templates can be as high as 10^{11} pores per square centimeter of membrane surface resulting in porosities between 30 and 50%. High porosity is an advantage over polymeric membranes in studies where a high volumetric density of the nanomaterial is desired. Recently, Masuda and coworkers prepared porous alumina membranes which combine highly

monodisperse pore diameters with a highly regular hexagonally-packed pore structure.[50] These nanohoneycomb templates have applications where ordering of the nanostructure is critical, for example in magnetic memory devices. In addition to pore diameter and ordering, pore separation distance can also be controlled.[51] This is expected to be important in the fabrication of photonic crystals and in fundamental studies of the effects of electrochemical growth conditions on template structure.

Aluminum oxide is amphoteric so its removal from the nanomaterial is accomplished by dissolution in either aqueous acid or base. This is a disadvantage where it is necessary to free the nanostructure from the membrane and the nanomaterial is soluble in acid or base. Recently, replicas of porous aluminum oxide templates have been prepared that can overcome this problem.[50,52] This concept involves making an exact copy of the alumina template using a material that is more suited to the deposition method or application of the nanomaterial. First, a "negative" is prepared by depositing poly(methylmethacrylate) in the pores of the alumina template. The alumina is then removed by dissolving in acid or base to reveal the polymeric nanofibers that have the same size and shape as the pores. Another material is then cast around the negative and the polymer is removed to form a replica of the porous alumina. In this way, the advantages of monodispersity and high porosity may be extended to the preparation of nanomaterials for which alumina is not suitable. Like polycarbonate templates, porous alumina is sold commercially for

filtration (Whatman, Inc.). However the available thicknesses and pore diameters are limited so that it is typically necessary to prepare this material in-house.

Applications of Template Synthesis. The biological precedent for template synthesis is biomineralization.[38,53,54] Organisms use this process to produce minerals essential for their survival. Biomineralization is not completely understood; however, on the nanometer scale it is thought to entail formation of minerals within self-assembled nanocavities. For example, a few animals use a template biomineralization process to prepare nanocrystals of magnetic iron oxide for the purpose of navigating via the earth's magnetic field. The size of the iron oxide crystal (<100 nm) is critical to ensure that it functions as a single magnetic domain.

Template synthesis using surfactant micelles has, in turn, been used to study the processes involved in biomineralization.[55] The nanocavities used for biomineralization in living organisms are thought to be analogous to self-assembled synthetic surfactants, such as $Cu(AOT)_2$ micelles. A study on the formation of copper nanoparticles in these micelles showed that the water content in these self-assembled surfactant templates is critical in controlling the size and shape of the nanoparticles. The results of this study not only provide a model for biomineralization, but a new template-synthesis strategy for controlling the size and shape of template-synthesized nanoparticles.

Mica was one of the first synthetically prepared templates used for the preparation of nanomaterials.[56] Microporous mica was prepared using the track-etch process where the damage tracks, again caused by exposure to nuclear

fission products, were etched with HF. Nanowires of Zn, Sn, or In were prepared by electrochemical deposition within the pores, demonstrating the usefulness of the template method for the preparation of nanomaterials.

Template synthesis has been used in electrochemical analysis to prepare a nanoelectrode ensemble which shows a dramatically lower detection limit (signal to background current ratio) versus a macroscopic electrode of the same material.[15] For this work, the low porosity of the polycarbonate membranes was an *advantage*. The nanostructured electrode was prepared by filling 30 nm diameter pores in a polycarbonate template membrane with gold using an electroless deposition method. The gold-polycarbonate membrane composite was used for the quantitative determination of an electroactive species using cyclic voltammetry. The pore density of the membrane used was approximately 0.1%; therefore, only a small surface of the membrane was gold. Since the background current in cyclic voltammetry is proportional to gold surface area, it was three orders of magnitude less than for a macroscopic gold electrode with the same geometric area. However, the faradaic current for these nanostructured electrodes is the same as for a bulk electrode. This was due to the spacing of the pores at the surface of the polycarbonate, e.g. the order imparted by the template. The result is a three order-of-magnitude decrease in detection limit.

Nanoporous polymeric template membranes also have applications in chemical separations.[2,57] For example, the size of the nanotube can be adjusted to very small diameters in order to filter molecules based on differences

in size. This was done by depositing gold in the pores of microporous polycarbonate template membranes to form gold nanotubes with an interior diameter of less than 1 nm. Using this microporous filter, a high degree of separation was achieved for methylviologen over $Ru(bpy)_3$ in an aqueous solution. In addition to filtering molecules based on size, the environment of the gold nanotube was modified to filter molecules based on differences in their charge and chemistry.[58]

In addition to separating molecules using the strategies outlined above (size and chemistry), a novel track-etched membrane was recently prepared where the pores can be open or closed based on the surrounding temperature.[59] The pores in these membranes are expected to serve as a model for "intelligent channels" which have the ability to transport molecules in response to an external stimulus.

Porous aluminum oxide membranes have been used to prepare nanostructured metals[12,60] and semiconductors.[18,52] Carbon nanotubes are of fundamental and practical interest because of their high tensile strength, hydrogen storage capability, and tunable electronic conductivity.[61,62] Carbon nanotubes have been prepared in nanoporous aluminum oxide membranes using chemical vapor deposition[8,63] and also via the deposition and subsequent carbonization of polyacrylonitrile nanotubes.[16] In addition, the template-synthesized carbon nanotubes have themselves been used as cavities for the deposition of metals and semiconductors.[32,33] The monodisperse and controllable pore diameter of porous alumina combined with its excellent thermal

stability will allow future studies on the effects of carbon tubule diameter on a wide range of properties.

Conclusions. The study of nanomaterials can provide information on the novel chemical and physical properties of materials with nanoscopic dimensions. These unique properties are expected to dramatically expand our understanding of the fundamental properties of matter and lead to a wide range of technological innovations. Membrane-based template synthesis is a proven method for preparing nanomaterials with precisely controlled particle size and shape. In addition, these nanostructured materials may be prepared with a high degree of spatial order. The wide range of template compositions and nanocavity arrangements allows the fabrication of nanomaterials using almost any method employed to prepare bulk materials.

LITHIUM-ION BATTERIES

Introduction. The development of rechargeable lithium-ion batteries is being driven primarily by the proliferation of portable electronic devices such as laptop computers, cellular phones and camcorders.[64] In addition, they are also being developed for use in electric vehicles[65,66] and spacecraft.[67-69] For these high value devices, run time is more important than the relatively higher cost of present day Li-ion technology. As shown in Figure 1.2, the primary advantage of Li-ion batteries over other rechargeable systems, such as NiCd, Pb acid, and NiMH batteries, is energy density. Li-ion batteries store more energy per unit weight and volume than their competitors, resulting in longer run times, lighter

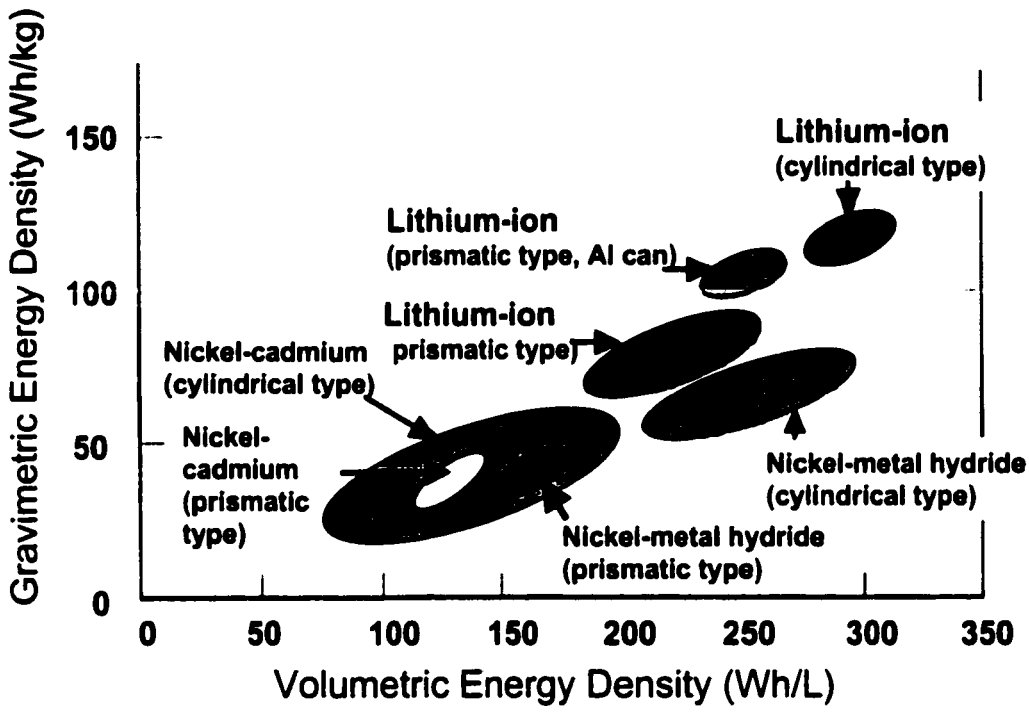

Figure 1.2. The volumetric and gravimetric energy densities of common rechargeable batteries. Adapted from reference 70.

device weight and more efficient use of space. Other reasons for the development of Li-ion systems include the growing environmental concern[71] over Cd and Pb and the low self-discharge rates[72] (loss of voltage and energy during storage) of Li-ion cells.

Batteries consist of one or more electrochemical cells which use chemical reactions to generate electrical energy. The cells can be linked in series or parallel depending on the intended application. The choice of electrode and electrolyte materials critically influences the energy and power output of the battery. The equations relating energy and power output to measurable variables are

$$\text{Energy (Watt-hours)} = \text{Voltage} \times \text{Capacity} \quad (1.1)$$

$$\text{Power (Watts)} = \text{Voltage} \times \text{Current} \quad (1.2)$$

Battery energy output is directly related to the average battery voltage and the amount of charge passed (in ampere-hours) during the discharge process. Battery power output is determined by the average discharge voltage and the current demand placed on the battery by the specific device.

The development of Li-ion technology is an outgrowth of the failure to develop a rechargeable battery based on a Li metal anode.[65,73] As a result, batteries with metallic lithium anodes are sold as primary (one-use) power sources. The majority of Li primary batteries combine a lithium metal anode with a Li-insertion cathode. The problem with this system lies in the instability of the anode during the recharge process. To circumvent this problem, Li-ion batteries have been developed which use a Li-insertion anode instead of the Li metal. Because of their use as electrode materials, Li-insertion compounds control the energy and power performance of both lithium and Li-ion batteries. One such compound is vanadium pentoxide, which was used to prepare the Li-insertion electrodes in Chapters 2 and 3. The remainder of this chapter provides information on the theoretical and practical aspects of lithium and Li-ion batteries and the lithium insertion compounds that critically affect their performance.

Lithium Batteries. Lithium metal is an excellent candidate for use in high energy density batteries because of its high specific charge capacity (Ah/g) and high electrode potential. Metallic lithium reacts rapidly with water and so it is restricted for use with nonaqueous electrolytes. Research on primary batteries

with metallic lithium anodes began in the 1950s after the discovery that lithium metal was stable, from a practical point of view, in a number of nonaqueous electrolyte systems like molten salts, liquid SO_2, and organic solvents like propylene carbonate.[74] Currently, lithium primary batteries are used in a variety of applications from space flight[70] to pacemakers[75] to portable electronic devices.[76] For example, most pacemakers manufactured today use a lithium anode in combination with an iodine-polyvinylpyridine composite cathode.[77] A lithium/I_2 battery can power a pacemaker for over 5 years because of its high energy density. However, the rate at which it can supply electrical energy is limited by the slow diffusion of lithium ions in the solid-state electrolyte. Thus it is contraindicated in other biomedical applications which call for high power. Lithium primary batteries are available for consumer and military applications from many companies including Sanyo (Japan), Ultralife (Newark, NY) and Polystor (Dublin, CA). These batteries typically use lithium in combination with a manganese oxide cathode and a nonaqueous liquid or polymer electrolyte. Data reported by Ultralife shows that the energy density of their Li primary batteries is four times higher than for similar size alkaline batteries.

The first attempt to commercialize a rechargeable lithium battery was announced in 1976 using a lithium insertion compound, TiS_2, as the cathode material.[78] The discharge reactions for this Li/TiS_2 cell are:

$$x\,Li \longrightarrow x\,Li^+ + x\,e^- \quad \text{Anode reaction} \quad (1.3)$$

$$x\,Li^+ + x\,e^- + TiS_2 \longrightarrow Li_xTiS_2 \quad \text{Cathode reaction} \quad (1.4)$$

$$x\,Li + TiS_2 \longrightarrow Li_xTiS_2 \qquad \text{Overall reaction} \quad (1.5)$$

Insertion compounds are open structured materials which act as hosts for the storage or release of lithium. During the discharge process, the lithium anode is oxidized and electrons flow through the external circuit into the electronic structure of the cathode material. At the same time, Li^+ ions dissolve into the electrolyte, migrate through the electrolyte, and enter the cathode atomic lattice. The overall process during discharge is simply transfer of lithium from the anode to the atomic lattice of the cathode material. The driving force for this reaction is the lower chemical potential of lithium within the insertion compound. Ideally, the cell can be recharged simply by reversing the flow of electrons. Thus, the recharge characteristics of the cell depend on the reversibility of the processes at the electrodes.

Lithium-insertion compounds are primarily layered or tunnel structures.[79] Lithium storage and release from insertion compounds is highly reversible because the tunnels or layers can accommodate lithium ions without destruction of the atomic lattice. Ideally, the lithium-host, solid solution has a wide range of stoichiometry resulting in high "x" (Eq. 1.4) values and, consequently, high electrode charge capacities. Also, the insertion compounds used as cathode materials, such as V_2O_5, $LiCoO_2$ and $LiMn_2O_4$, develop cell voltages up to 4 V vs. a lithium anode.[41] After demonstrating the reversibility, high capacity and high voltage of lithium-insertion cathode materials, the development of a high energy density rechargeable lithium battery was attempted.

The limiting factor in the commercialization of lithium rechargeable batteries is the poor cycling efficiency of the lithium metal anode.[64,65,80] The high reactivity of the lithium that results in its high energy density also causes an inherent instability in contact with organic electrolytes, resulting in the formation of a passivation layer. This layer, called the solid electrolyte interface (SEI), is made of products from the reaction of lithium with the salt and solvent in the electrolyte. Constituents of the SEI include Li_2CO_3, LiO_2, LiOH, and LiX compounds, where X refers to the halogen, either chlorine or fluorine, that is a constituent in the anion in the lithium salt. The SEI is ionically conducting and electronically insulating, thus it is stable during rest periods. Figure 1.3A shows a schematic representation of the SEI on lithium metal. It has been postulated that the SEI conducts lithium ions through narrow paths or pores within the layer.

Two mechanisms are considered to contribute to the poor cycling efficiency of lithium anodes. The primary mechanism involves isolation of dendritic lithium from the anode.[64] During charging, the deposited lithium forms dendrites instead of evenly coating the metal surface. Figure 1.3B shows a schematic representation of these dendrites forming in the pores of the SEI. During discharge lithium at the base of the dendrite can dissolve, isolating the projection from the anode (Fig. 1.3C). In addition to reducing capacity, dendrite formation can also be a significant safety hazard. For cells with short distances between the anode and cathode, there is the possibility that the dendrites can reach the cathode resulting in cell shorting. Shorted lithium cells can experience heating and venting of gas with the worse case scenario being fire or explosion

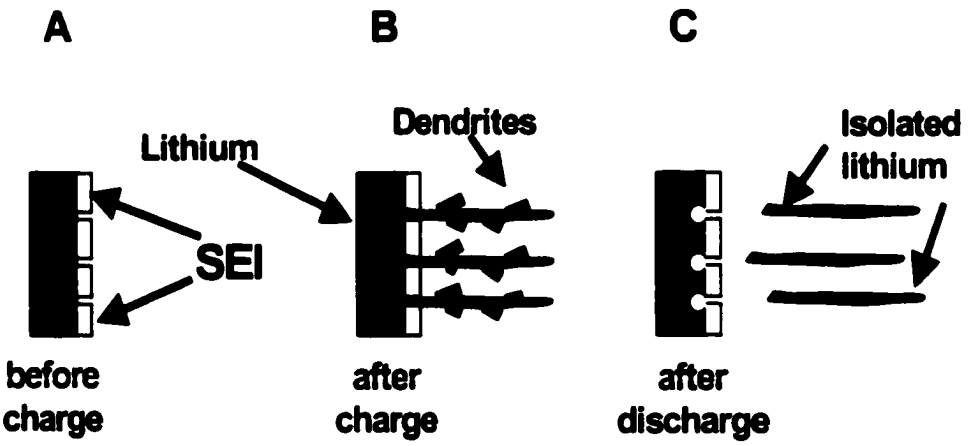

Figure 1.3. Schematic of the solid electrolyte interface (A) on a lithium anode and the formation of Li dendrites (B) during battery charging and the subsequent loss of capacity due to lithium isolation (C) during cell discharge. Adapted from reference 64.

due to decomposition of the organic solvent in the electrolyte. In the second mechanism, lithium is dissolved from or deposited on the lithium surface connected to the SEI during the discharge and charge processes respectively. This causes disruption and then reformation of the SEI, which consumes lithium in the process.

Lithium Ion Batteries. The feasibility of overcoming these problems was demonstrated in the late 1970s by using an insertion compound (graphite) to replace the Li metal anode.[65] Since both electrodes in this cell were insertion compounds, no lithium metal existed because the lithium is always held as a guest in one of the insertion electrodes. Using a lithium insertion anode replaces problematic lithium metal dissolution and plating with the reversible processes of lithium ion (and electron) uptake and release. Replacement of metallic lithium, however, results in a loss in energy density because of the lower specific capacity and lower cell voltages associated with using insertion compounds. A

general schematic of this type of cell is shown in Figure 1.4. The electrochemical processes involve only the transfer of lithium ions (and electrons) between the two electrodes

$$Li_yM_nY_m + A_zB_w \underset{\text{charge}}{\overset{\text{discharge}}{\rightleftharpoons}} Li_{(y-x)}M_nY_m + Li_xA_zB_w \qquad (1.6)$$

As illustrated in Figure 1.4, the lithium ions shown in Equation 1.6 "rock" from one electrode to the other during discharge and charge. Therefore these cells were first termed "rocking chair batteries" by Armand in 1980.[81]

The first commercial battery to use lithium insertion compounds for both the anode and cathode was introduced by Sony in 1990.[72,82] Sony named their product a "Li Ion Rechargeable Battery" since it contained no metallic lithium. The Sony battery used layered carbon as the anode and $LiCoO_2$ as the cathode. Although other materials are being studied, carbon remains the only insertion compound used as an anode for commercially available Li-ion batteries.[83] Data from Sony's initial report showed that the experimental energy density of a size "D" battery was 253 Wh/L compared to 87 Wh/L and 74 Wh/L for similar size NiCd and Pb acid batteries. The cycle life of the Li-ion cell was also better. The number of discharge/charge cycles that were completed to 100 % of the experimentally determined capacity (given above) was 1200 for the Li-ion battery, 800 for the NiCd and 300 for the Pb acid. Based on the high performance of the Sony battery, Li-ion cells have been developed and proposed for an ever increasing number of applications. The following sections will

address theoretical and engineering aspects which control the energy density and power capability of lithium and Li-ion batteries.

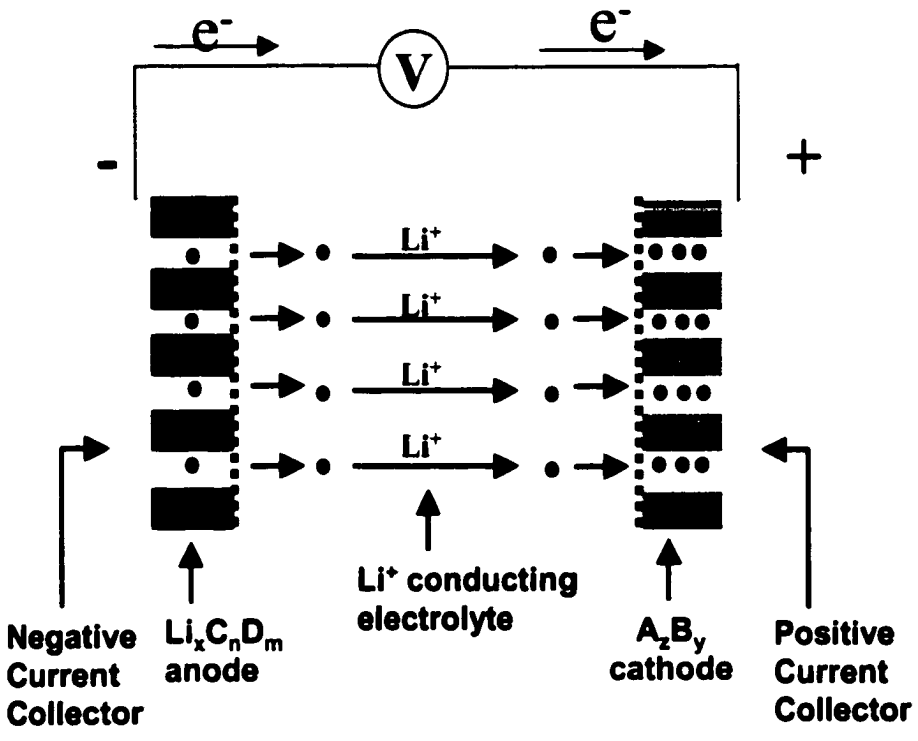

Figure 1.4. Schematic diagram showing the discharge of a $Li_xC_nD_m/A_zB_y$ cell in which both anode and cathode are based on lithium insertion hosts. Adapted from reference 84.

Energy. Battery energy density is controlled by the choice of insertion materials used in the electrodes. To maximize energy density, these compounds must develop a high cell voltage and have high charge capacities (Equation 1.1). Capacity is simply the amount of lithium that can be stored in the insertion electrodes. The limits of reversible stoichiometry are determined experimentally by cycling the material over different ranges of lithium concentration.[85,86] The objective is to determine how electrode or battery capacity is affected by an

extended number of charge/discharge cycles, where the charge and discharge conditions are determined by the intended application. Various factors affect cycling efficiency, and it is impossible to know, a priori, how an insertion material will respond to cycling. For example, batteries using carbon insertion anodes show a drop in capacity over the first few discharge/charge cycles with a stable capacity thereafter. This is due to the formation of a solid electrolyte interface, SEI, layer on the carbon.[87] Similar to the lithium SEI layer (Fig. 1.3), it is composed of Li salts which form due to reduction of the electrolyte at the carbon surface. Once formed, however, the SEI layer is stable during cycling; therefore, there is no dramatic capacity loss with cycling like with Li metal anodes.

Battery cycling can, however, cause other problems that affect both cathode and anode materials and result in a decrease in capacity with cycle number.[85,86] These include separation of the electrode material from the current collector, loss of interparticle contact, electrolyte oxidation or reduction during overcharge, phase changes, and active material dissolution. For example, lithium insertion electrodes are commonly fabricated by pressing a mixture of finely ground insertion material, a polymeric binder and an electronic conductor (such as carbon) onto a current collector under high pressure.[88] If the discharge/charge process causes a phase change, the insertion particles may fracture and lose contact with one another or the current collector. The resulting isolation of the insertion material would result in an irreversible loss in electrode capacity. Ultimately, achieving high battery capacity is a compromise between striving for high Li content and reversibility, e.g. preventing destruction of the

atomic lattice. The reversible insertion ranges for many insertion materials have been studied and reported in the literature.[41] However, the proper balance for each system can only be obtained through testing and careful design engineering.

Cell Voltage. Besides capacity, the choice of electrode materials also controls the maximum free energy of the galvanic reaction, ΔG, and therefore the maximum attainable cell voltage[89] as shown in Equation 1.7

$$\Delta G = -nFE \qquad (1.7)$$

where E is the cell potential, F is Faraday's constant (96485 C mol^{-1}) and n is the number of electrons transferred in the discharge reaction.

An important consequence of using insertion compounds is that the lithium content in the anode and cathode changes during discharge and charge. The free energy of the reaction changes with lithium content in the electrodes and this is reflected in the chemical potential (Equation 1.8),[90,91]

$$\mu_{Li} = \partial G / \partial n = \mu^{\theta} + RT \ln a_{Li} \qquad (1.8)$$

where n is the amount of material present, R is the universal gas constant, T is the temperature in Kelvin, μ^{θ} is the standard chemical potential due to the guest / host interaction, and a_{Li} is the activity of lithium in the insertion material. As these equations show, the value of the chemical potential will become more positive with increasing lithium content.

Under equilibrium conditions, where the composition of Li is the same in the bulk and at the electrode surface, the cell voltage can be defined as shown in Equation 1.9[64,92,93]

$$E = (\mu^{Li}_{cathode} - \mu^{Li}_{anode}) / F \quad (1.9)$$

where μ^{Li} is the chemical potential of lithium at the surfaces of the electrodes and F is Faraday's constant. Thus the cell voltage is a measurable quantity which relates the difference in chemical potential of lithium at the surfaces of the two electrodes.[91] In addition, Equation 1.9 shows that during discharge the chemical potentials of lithium in the anode and cathode will move toward each other resulting in a decreasing cell voltage. Eventually, a voltage is reached, called the cutoff voltage, where the device no longer functions and the discharge terminates and energy output, according to Equation 1.2, is the product of the average voltage and total capacity during the discharge.

Chemical potential can be separated into electronic, μ_{e^-}, and ionic, μ_{Li^+}, components[64,94] as indicated in Equation 1.10,

$$\mu_{Li} = \mu_{e^-} + \mu_{Li^+} \quad (1.10)$$

which serves to highlight the important aspects of insertion compounds with respect to maximizing cell voltage. The electronic term, μ_{e^-}, can be defined as the difference in electron energy between the Fermi level and the vacuum level for the insertion material. Simply put, anode materials should be electropositive where the electron energy and Fermi level are high and cathode materials should be the opposite, strong oxidizers with a low Fermi level energy. The ionic component represents solvation of lithium ions by the insertion material. For cathode materials, solvation is enhanced, and the chemical potential is lowered, by Lewis base interactions within the cathode atomic lattice. The majority of

cathode materials are transition metal oxides and chalcogenides so this solvation stability comes from interaction of the lithium ions with the lone pair electrons on either oxygen or chalcogen atoms.

In summary, cell voltage is a function of the differences in lithium chemical potential at the surfaces of the electrodes. Chemical potential can be separated into electronic and ionic components which show the important selection criteria for insertion electrodes in order to maximize voltage and energy. Cathode materials should be highly oxidizing with the ability to solvate lithium ions through Lewis base interactions within the atomic lattice while the Fermi level of lithiated anodes should be as high as possible.

Power Density. Power output (Equation 1.2) is the product of the current and voltage delivered by the battery. At high current, power losses result from the slow diffusion of lithium ions within the electrolyte and solid insertion compounds.[64,71,95] These mass transport limitations result in an internal resistance and polarizations which reduce the open circuit potential, V_{oc}, of the battery by an amount (Equation 1.11)

$$V = V_{oc} - IR_b - \text{polarization losses} \qquad (1.11)$$

where IR_b is the voltage drop due to the internal resistance of the battery and the polarization losses are due to Li^+ ion concentration gradients in the insertion materials. Thus the delivery of maximum energy output at high current (Equation 1.12)

$$\text{Energy}_{max} = V_{max} \times \text{Capacity}_{max} \qquad (1.12)$$

requires a low internal battery resistance and minimum polarization losses.

The components of battery internal resistance, IR_b, are[92] (Equation 1.13)

$$R_b = R_{el} + R(A) + R(C) + Rc(A) + Rc(C) \quad (1.13)$$

the resistance to mass transport of Li^+ in the electrolyte, R_{el}, the electronic resistances of the anode and cathode insertion materials, R(A) and R(C), and the electronic resistances of the anode and cathode current collectors, Rc (A) and Rc(C), respectively. Electrolyte resistance can be explained as a resistance to diffusion of Li^+ due to interactions with the solvent and other ions in solution.[96] During discharge there is a concentration gradient of Li^+ across the electrolyte as lithium ions insert into the cathode and are released from the anode. Fick's first law of diffusion (Equation 1.14)

$$J_{Li+} = -D\,(dC/dx) \quad (1.14)$$

shows that Li^+ will diffuse through the electrolyte to alleviate this difference in concentration[97] where J_{Li+} is the flux of Li^+ ions through the electrolyte in units of moles sec^{-1} cm^{-2}, D is the diffusion coefficient of Li^+, C is the concentration of Li^+ and x is the distance along the perpendicular between the electrodes. The sign of the flux indicates the direction of movement according to the chosen coordinate system. During diffusion, lithium ions encounter solvent molecules and other ions which limit their rate of travel. These encounters result in an electrolyte resistivity, κ, the magnitude of which is affected by the concentration of Li^+, the solution viscosity and the ionic radius.[97] Electrolyte resistance, R_{el}, is ohmic in nature and is affected by the same parameters that control the resistance to electron flow in the metal current collectors,[97] namely (as shown in Equation 1.15)

$$R_{el} = L \kappa A^{-1} \quad (1.15)$$

the length of ion or electron travel, L, the crossectional area, A, and the resistivity of the material, κ. Using these parameters, battery designers can minimize R_b in order to maximize battery voltage and energy output at high discharge current.

Concentration Polarization. During battery discharge, lithium ions leave the anode and insert into the cathode atomic lattice. Lithium insertion rate density, J, is controlled by[98]

$$J = I (nFA)^{-1} \quad (1.16)$$

the discharge current, I, the active surface area of the insertion material, A, and the number of electrons transferred in the discharge reaction, n. At high discharge current density, the rate of Li ion insertion can be much faster than the rate at which it diffuses into the bulk of the insertion compound. This causes a concentration gradient, or polarization, of Li^+ within the solid insertion material in the electrode. Consider the Li-ion cell shown in Figure 1.5A where the anode and cathodes are solid insertion electrodes separated by an electrolyte. Figure 1.5B shows the concentration gradients that result at the surfaces of the electrodes due to high insertion rate density and slow diffusion. Equations 1.8 and 1.9 show that cell voltage is related to the activity of Li at the electrode surfaces, therefore, large concentration gradients can cause the cell voltage to reach the cutoff value before the entire amount of Li is transferred from the anode to the cathode. The effect of concentration polarization is a significantly lower battery capacity and energy output than is theoretically available.

Concentration polarization can be reduced by increasing the active

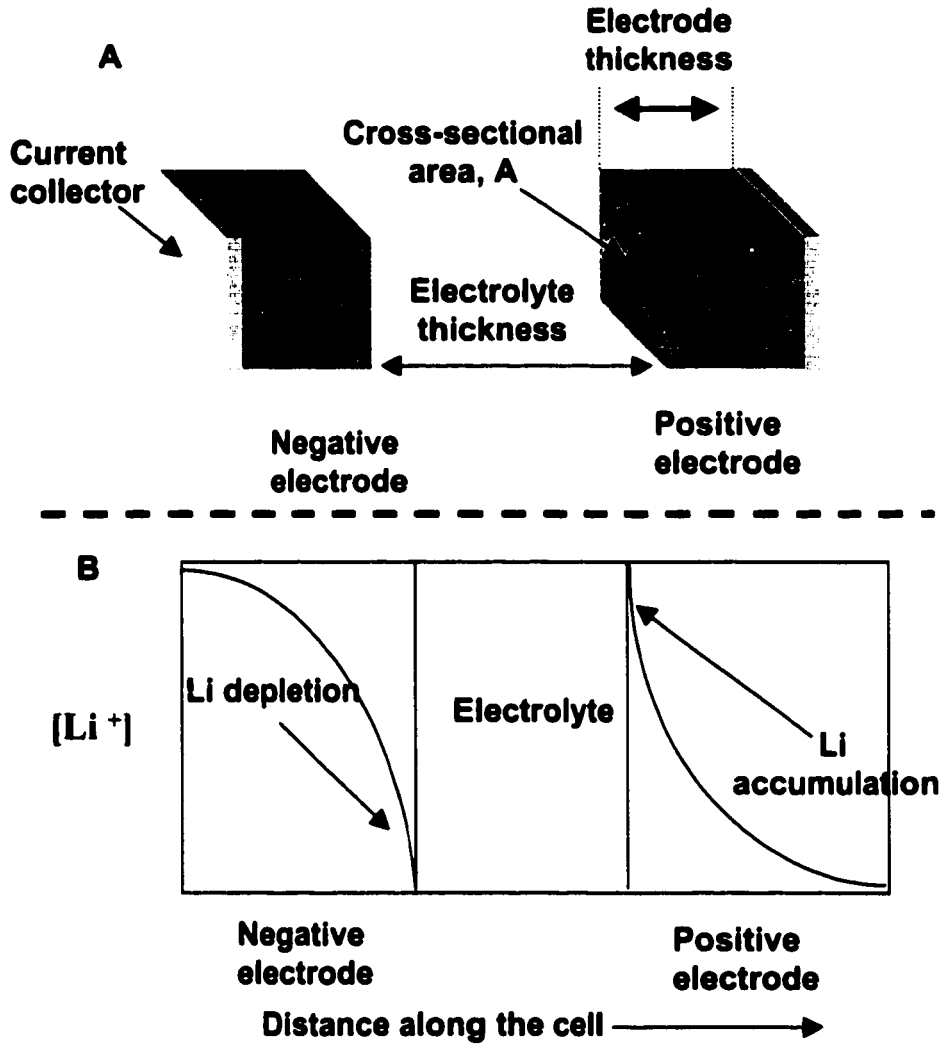

Figure 1.5. Schematic of a Li-ion cell (2.5A) and the resulting concentration gradients of Li^+ in the insertion electrodes (2.5B) at high discharge current. Cell voltage is determined by the Li^+ concentration at the surfaces of the electrodes. Adapted from reference 64.

surface area of the electrode material.[64,92] This has the effect of reducing insertion rate density and the Li^+ concentration gradients at the electrode surfaces. Thus, increasing surface area results in higher cell voltages for the same amount of Li inserted, longer discharge times to the cutoff voltage, and higher electrode and battery capacity.

Another way to look at concentration polarization is to consider the time required for Li^+ ion diffusion through the bulk of the insertion material. This time is related to the diffusion distance, L, and the diffusion coefficient, D_{Li}, where $t = L^2 D_{Li}^{-1}$.[97,99] Consider the positive electrode depicted in fig. 1.5A where L is the distance between the electrolyte/electrode interface and the current collector. If lithium ions are inserted at the same rate at which they diffuse through the bulk, concentration polarization is eliminated. If D_{Li} is known, then "t" can be used to calculate the maximum discharge current (electrode capacity / time) for which there should be no polarization of lithium within the insertion material. Thus decreasing diffusion distance increases the maximum discharge rate of the electrode and provides another means of increasing electrode capacity at high discharge current, e.g. electrode rate capability.

Conclusions. Lithium-ion rechargeable batteries have significantly higher energy storage capabilities than the more ubiquitous NiCd, Pb-acid and NiMH rechargeables. Because of their higher cost however, Li-ion cells are used primarily in high-value devices where runtime is the main concern. Battery energy storage is a function of the choice of the insertion materials used in the electrodes. These materials control the thermodynamics of the discharge reaction as well battery capacity.

Battery energy output at high discharge currents is limited by the slow mass transport of Li^+ ions in the electrolyte and within the solid insertion materials used in the electrodes. Because these are kinetic and not thermodynamic considerations, careful attention to cell design can result in

increased performance at high power. For example, electrolyte resistance can be minimized by reducing the distance between the electrodes, increasing the ionic conductivity of the electrolyte, and increasing the cross-sectional area for ion travel. Concentration polarization of Li^+ within the electrode materials can be obviated by increasing insertion material surface area and reducing Li^+ ion diffusion distances.

VANDIUM PENTOXIDE

Introduction. Vanadium pentoxide, V_2O_5, has technological applications in oxidative catalyses,[100,101], ethanol[102] and humidity[103] sensors, electrochromic devices,[104] and as an insertion electrode in Li-ion batteries.[41] Methods of preparation that are amenable to the template synthesis of nanostructured V_2O_5 include the electrochemical oxidation of $VOSO_4$,[105] thermal treatment of NH_4VO_3,[106] plasma-enhanced chemical vapor deposition from $VOCl_3$,[107,108] and sol-gel chemistry[103]. The nanostructured and thin-film V_2O_5 electrodes used in Chapters 2 and 3 were prepared by combining membrane-based template synthesis and sol-gel chemistry. Powder X-ray diffraction results in Chapter 2 show that the nanostructured electrode material was orthorhombic V_2O_5. These electrodes were used to explore the effect of insertion material surface area and lithium-ion diffusion distance on electrode rate capability in Chapter 2. In Chapter 3, high-energy nanostructured electrodes were prepared to show their potential for use in a high rate lithium microbattery. The following sections describe the sol-gel synthesis, crystal structure, and Li diffusion properties of crystalline V_2O_5.

Sol-gel synthesis of V_2O_5. Sol-gel chemistry is a powerful route for the preparation of crystalline and amorphous oxides.[109-111] The method is based on the hydrolysis and condensation of molecular precursors which are either metal salts or metal-alkoxides. With both precursors, hydrolysis results in formation of reactive M-OH groups which then condense to metal-oxygen-metal bonds. Further condensation results in the formation of a sol, or colloidal dispersion, consisting of oxopolymers and oligomers with the aggregation of the sol resulting in the formation of an aqueous gel. Sols and gels can be processed to obtain powered, films, fibers and monolithic glasses. Sol-gel methods have been reported for many lithium-insertion materials including, $LiCoO_2$,[112] $LiMn_2O_4$,[113] TiO_2,[114] V_2O_5,[111] and TiO_2.[115] The benefits of sol-gel synthesis are as follows:[111]

1) A homogeneous multicomponent system can be obtained simply by mixing the appropriate precursors.

2) Hydrolysis and gel formation occur at low (ambient) temperatures

3) The rheological properties of the sols and gels permit formation of fibers, films, or composites via spin coating, dip coating, or impregnation (template synthesis).

Ammonium metavanadate, NH_4VO_3, and triisopropoxyvanadium (V) oxide, $VO(OC_3H_7)_3$, are typical examples of metal salt and alkoxide precursors, respectively, that can be used to prepare vanadium oxide gels.[103] Metal salt sol-gel chemistry begins by acidification using a proton exchange resin to obtain

vanadic acid, H_3VO_4, which rapidly takes on two water molecules via nucleophilic addition giving $[VO(OH)_3(OH_2)_2]$. Condensation of the hexacoordinated species occurs spontaneously at pH 2 resulting in dark red colloidal solutions or gels. Spin or dip coated films are prepared from solutions with vanadium concentration set at less than 0.1 M to obtain the correct rheology. If dried at ambient temperature, the result is a xerogel (dehydrated) film of composition $V_2O_5 \bullet nH_2O$.

The simplified hydrolysis and condensation reactions for triisopropoxyvanadium (V) oxide (TIVO) can be described as follows[116]

$$VO(OC_3H_7)_3 + 3H_2O \longrightarrow VO(OH)_3 + 3C_3H_7OH \quad (1.17)$$

$$2VO(OH)_3 \longrightarrow V_2O_5 + 3H_2O \quad (1.18)$$

The approach used in Chapters 2 and 3 was to prepare crystalline V_2O_5 electrodes using this alkoxide precursor. Hydrolysis was carried out under ambient humidity and the resulting gel was thermally processed at 400 °C in oxygen. Crystallization of V_2O_5 gels is known to occur between 315 and 325 °C.[117] Powder X-Ray diffraction data shown in Chapter 2 confirms that the final product was orthorhombic V_2O_5.

Crystal Structure. Figure 1.6 shows that the structure of crystalline V_2O_5 is characterized by the packing of V_2O_5 layers along the *c* axis of an orthorhombic unit cell.[118-120] These layers are composed of corner and edge sharing square pyramids of VO_5. The V-O bond distances for the 4 oxygens at the base of the pyramids are approximately 2 Angstroms. The out of plane

(apical) V-O bond distance is 1.54 angstroms and infrared absorption analysis indicates that this is a double bond.[120] The layers are held together by van der Waals forces between vanadium and apical oxygen atoms in the next layer (V ••• O1 in Figure 1.6B). Thus the coordination of vanadium appears as a distorted octahedron with a V-O interlayer bond distance of 2.79 Angstrom which allows ample room for the storage and diffusion of Li^+ ions (ionic radius < 1 Angstrom)[121] between the layers.

Lithium ion diffusion is an activated process which involves hopping between coordination sites along the b direction in channels provided by the apical oxygens.[93,118] Molecular dynamics computer simulations indicate that the barrier for Li^+ ion migration in the <010> direction is 0.87 eV, while in the <001> direction it is 2.47 eV.[122] This work also showed a similar result for Li^+ insertion from the electrolyte. The rate of Li ion insertion was compared for two different orientations of the V_2O_5 crystal lattice with respect to a Li ion containing electrolyte. Simulations showed a faster Li ion insertion rate when the *b* direction was perpendicular to the V_2O_5 -electrolyte interface than for a perpendicular orientation of the *c* direction. This is due to more facile insertion of Li^+ into the tunnel structures provided by the apical oxygens as opposed to insertion through layers of VO_5 square pyramids.

As shown previously (Equation 1.14), the chemical diffusion coefficient is indicative of the rate at which a species moves in a host material. Reported values of the chemical diffusion coefficient for lithium in $Li_xV_2O_5$ for $0 < x < 1$ are between 10^{-11} and 10^{-15} cm^2 sec^{-1}.[123-125] In general, the trend is that Li ion

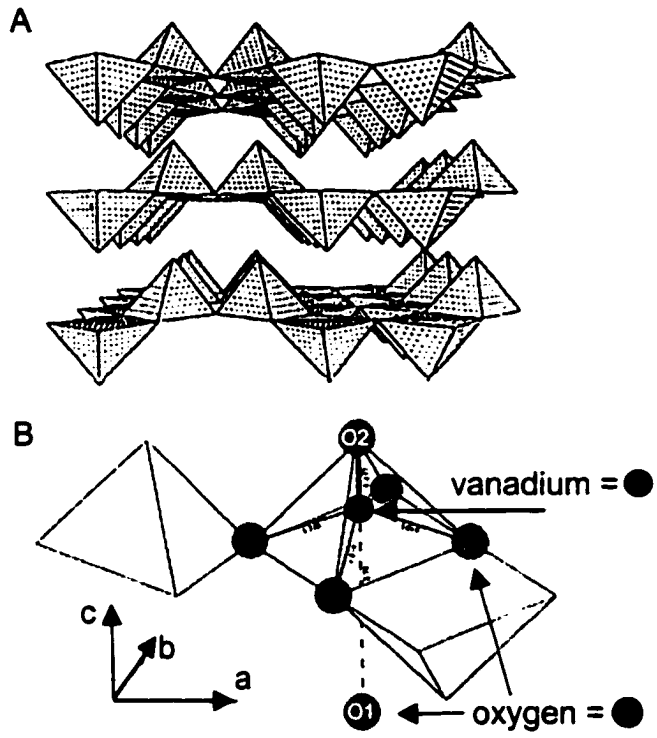

Figure 1.6. V_2O_5 structure showing the layers (A) and coordination around the vanadium (B). Apical (out of plane) oxygens are labeled as "O1" and "O2". Adapted from reference 118.

mobility decreases with increasing Li^+ content in the host lattice. The parameters which control diffusion rate are changing lattice parameters, ionicity of the lattice, and degree of filling.[126] As the Li ion content increases the V_2O_5 layers expand along the c axis, providing more room for Li^+ movement but at a cost of greater ionic repulsion which limits mobility.

Electrochemistry. Chronopotentiometry is widely used to explore the electrochemistry of lithium insertion compounds.[97,98] These experiments are typically performed in a three electrode cell containing the Li-insertion working electrode, lithium counter and reference electrodes, and a non-aqueous

electrolyte composed of a Lewis base organic solvent, such as propylene carbonate, and a lithium-containing salt, such as $LiClO_4$. Chronopotentiometry follows the change in cell voltage with the change in Li content in the insertion material lattice. Lithium content (activity) is controlled by applying a constant current to the insertion electrode. Since the reference electrode is lithium (where $\mu_{Li} = 0$), the voltage measurement shows the change in chemical potential of Li at the working electrode surface with changing Li^+ ion activity. The magnitude of the current controls the *rate* at which the ions move into and out of the lattice, so chronopotentiometry can be used to investigate both the kinetic and thermodynamic aspects of the lithium insertion process.

Figure 1.7 shows a chronopotentiometric curve of open circuit voltage versus lithium content (e.g., x value in $Li_xV_2O_5$) for a lithium/$Li_xV_2O_5$ cell. The curve was obtained by applying brief current pulses to the V_2O_5 cathode followed by long equilibration periods to allow for diffusion and, eventually, a homogeneous distribution of Li^+ ions within the insertion material. The cell reactions during this process are

$$x\,Li \longrightarrow x\,Li^+ + x\,e^- \quad \text{Anode reaction} \quad (1.19)$$

$$x\,Li^+ + x\,e^- + V_2O_5 \longrightarrow Li_xV_2O_5 \quad \text{Cathode reaction} \quad (1.20)$$

$$x\,Li + V_2O_5 \longrightarrow Li_xV_2O_5 \quad \text{Overall reaction} \quad (1.21)$$

During equilibration, the cell voltage changes as the Li ion content at the electrode surface redistributes. Cell voltage is recorded when a constant value is reached and the next short current pulse is then applied. The mass of lithium inserted is equivalent to the total charge passed during the current pulse (current

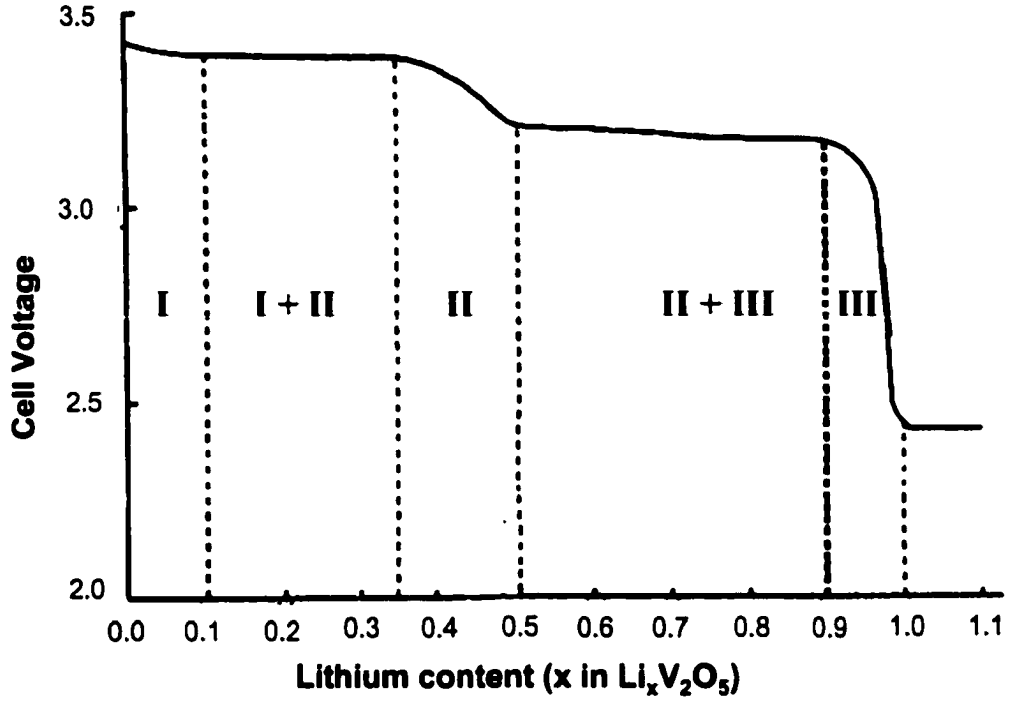

Figure 1.7. Open circuit voltage (OCV) vs. lithium content (x value) for a Li / $Li_xV_2O_5$ cell with an electrolyte of 1M $LiClO_4$ in propylene carbonate. See text for explanation of regions labeled I, II and III. Adapted from reference 127.

x time) and "x" values can be assigned if the mass of V_2O_5 is known. The cell voltages shown in Figure 1.7 are measured at open circuit (current = 0) and therefore are thermodynamic values relating cell potential to lithium activity.

The open circuit voltage curve in Figure 1.7 is characterized by voltage plateaus at 3.4 and 3.2 volts vs. the lithium anode for composition ranges of $0.1 < x < 0.35$ and $0.5 < x < 0.9$ respectively. Sloping regions of voltage occur for $0 < x < 0.05$, $0.35 < x < 0.50$, and $0.9 < x < 1.0$. Regions of sloping potential indicate lithium insertion into single crystalline phases of V_2O_5 labeled I, II and III. In these composition ranges chemical potential (and cell voltage) are expected to

change with lithium content as shown in Equation 1.8. The voltage plateaus, however, indicate regions of $Li_xV_2O_5$ composition where two crystalline phases exist in equilibrium. As predicted by the Gibbs phase rule, the chemical potential of lithium remains constant while these phases co-exist, thus cell voltage is independent of composition. [90,128]

X-ray diffraction studies have shown that the structures of all three phases are very similar to that of the parent V_2O_5.[118,127] The structural consequences of Li insertion are an increase in the interlayer spacing (along the *c* direction) and a slight puckering of the layers. However, no bonds are broken in the atomic lattice. The three phases are metastable and can be readily interconverted. As a result, lithium insertion into crystalline V_2O_5 is highly reversible for $0 < x < 1$ resulting in a high coulombic efficiency, e.g. all of the lithium inserted can be extracted, and a high capacity of 147 mAh/g for $Li_{1.0}V_2O_5$.

Conclusions. V_2O_5 is a technologically important cathode material for lithium and Li-ion batteries. Crystalline V_2O_5 can be prepared using a simple and efficient sol-gel technique. When combined with the template synthesis method, the sol-gel technique was well suited for the preparation of the nanostructured V_2O_5 electrodes discussed in Chapters 2 and 3. Crystalline $Li_xV_2O_5$ is highly reversible for $0 < x < 1$, resulting in good electrode cycle life, and develops a high voltage in combination with a lithium anode. Therefore its Li-insertion electrochemistry has been well characterized, leading to incorporation as a cathode material in both lithium and lithium-ion batteries and making it a good choice for a model compound for these studies.

REFERENCES FOR CHAPTER 1

1. Dutta, J.; Hofmann, H.; Schmid, G. *Adv. Mater.* **1996**, *8*, 555-556.

2. Martin, C. R.; Mitchell, D. T. *Anal. Chem.* **1998**, *70*, 322A-327A.

3. Mehra, J. *The Beat of a Different Drum. The Life and Science of Richard Feynman*; Clarendon Press: Oxford, **1994**.

4. Nanostructured Materials, *Mater. C.* **1996**, *8*, 1569-2188.

5. Hulteen, J. C.; Martin, C. R. *J. Mater. Chem.* **1997**, *7*, 1075-1087.

6. Martin, C. R. *Science* **1994**, *266*, 1961-1966.

7. Ozin, G. A. *Adv. Mater.* **1992**, *4*, 612-649.

8. Che, G.; Lakshmi, B. B.; Martin, C. R.; Fisher, E. R. *Chem. Mater.* **1998**, *10*, 260-267.

9. Bowes, C. L.; Malek, A.; Ozin, G. A. *Chem. Vap. Deposition* **1996**, *2*, 97-103.

10. Shelimov, K. B.; Moskovits, M. *Chem. Mater.* **2000**, *12*, 250-254.

11. C. A. Foss, Jr.; Hornyak, G. L.; Stockert, J. A.; Martin, C. R. *J. Phys. Chem.* **1994**, *98*, 2963-2971.

12. Blondel, A.; Meier, J. P.; Doudin, B.; Ansermet, J.-P. *Appl. Phys. Lett.* **1994**, *65*, 3019-3021.

13. Schwarzacher, W. *Electrochem. Soc. Interface* **1999**, *8*, 20-24.

14. Ang, L.-M.; Hor, T. S. A.; Xu, G.-Q.; Tung, C.-h.; Zhao, S.; Wang, J. L. S. *Chem. Mater.* **1999**, *11*, 2115-2118.

15. Menon, V. P.; Martin, C. R. *Anal. Chem.* **1995**, *67*, 1920-1928.

16. Parthasarathy, R. V.; Phani, K. L. N.; Martin, C. R. *Adv. Mater.* **1995**, *7*, 896.

17. Cepak, V. M.; Martin, C. R. *Chem. Mater.* **1999**, *11*, 1363-1367.

18. Lakshmi, B. B.; Dorhout, P. K.; Martin, C. R. *Chem. Mater.* **1997**, *9*, 857.

19. Patrissi, C. J.; Martin, C. R. *J. Electrochem. Soc.* **1999**, *146*, 3176-3180.

20. Chakarvarti, S.; Vetter, J. *Solid State Phenomena* **1997**, *55*, 80.

21. Uchida, T.; Beinuma, T.; Ishizaki, T. *J. Phys. Chem. B* **1999**, *103*, 3659-3662.

22. Xavier, M. P.; Garcia-Fresnadillo, D.; Moreno-Bondi, M. C.; Orellana, G. *Anal. Chem.* **1998**, *70*, 5184-5189.

23. Sorbin, A. G.; Vargas, M. D.; Alves, O. L. *J. Mater. Chem.* **1999**, *9*, 519-523.

24. Borisov, B. F.; Charnaya, E. V.; Plotnikov, P. G.; Hoffamann, V. D.; Michel, D.; Kumzerov, Y. A.; Tien, C.; Wur, C. S. *Phys. Rev. B* **1998**, *9*, 5329-5335.

25. Graf, M. J.; Huber, T. E.; Huber, C. A. *Phys. Rev. B* **1992**, *45*, 3133-3140.

26. Molz, E.; Wong, A. P. Y.; Chan, M. H. W.; Beamish, J. R. *Phys. Rev. B* **1993**, *48*, 5741-5749.

27. Pike, J. K.; Byrd, H.; Talham, D. R. *Thin Solid Films* **1994**, *243*, 510.

28. Sennett, P.; Dombrowski, T. Clays. In *Kirk-Othmer Encyclopedia of Chemical Technology*; Kroschwitz, J. I. and Howe-Grant, M., Ed.; John Wiley & Sons: New York, **1997**; Vol. 6, pp 381-423.

29. Bruce, D. W.; O'Hare, D. *Inorganic Materials*; Wiley: New York, **1992**.

30. Kyotani, T.; Tomita, A.; Mori, T. *Chem. Mater.* **1994**, *6*, 2138.

31. Kimizuka, N.; Kunitake, T. *Adv. Mater.* **1996**, *8*, 89-91.

32. Guerret-Piecourt, C.; Bouar, Y. L.; Loiseau, A.; Pascard, H. *Nature* **1994**, *372*, 761-765.

33. Kyotani, T.; Tsai, L.-f.; Tomita, A. *Chem. Commun.* **1997**, 701-702.

34. Wu, C.-G.; Bein, T. *Science* **1994**, *266*, 1013-1015.

35. Pearson, D. H.; Tonucci, R. J.; Bussmann, K. M.; Bolden, E. A. *Adv. Mater.* **1999**, *11*, 769-773.

36. Nguyen, P. P.; Pearson, D. H.; Tonucci, R. J. *J. Electrochem. Soc.* **1998**, *145*, 247-251.

37. Wu, M.; O'Neill, S. A.; Brousseau, L. C.; McConnell, W. P.; Shultz, D. A.; Linderman, R. J.; Feldheim, D. L. *Chem. Commun.* **2000**, 775-776.

38. Hotz, J.; Meier, W. *Adv. Mater.* **1998**, *10*, 1387-1390.

39. Schonenberger, C.; Zande, B. M. I. v. d.; Fokkink, L. G. J.; Henny, M.; Schmid, C.; Druger, K.; Bachtold, A.; Buber, R.; Birk, H.; Staufer, U. *J. Phys. Chem. B* **1997**, *101*, 5497-5505.

40. Brumlik, C. J.; Menon, V. P.; Martin, C. R. *J. Mater. Res.* **1994**, *9*, 1174-1183.

41. Hossain, S. Rechargeable Lithium Batteries (Ambient Temperature). In *Handbook of Batteries*; 2nd ed.; Linden, D., Ed.; McGraw-Hill: New York, **1995**, pp Chapter 36.

42. Fleischer, R. L.; Price, P. B.; Walker, R. M. Part I. Principles of Track Etching. In *Nuclear Tracks in Solids*; University of California Press: Berkely, **1975**, pp 3-20.

43. Fleischer, R. L.; Price, P. B.; Walker, R. M. *Nulcear Tracks in Solids*; University of California Press: Berkely, **1975**.

44. Li, F.; Zhang, L.; Metzger, R. M. *Chem. Mater.* **1998**, *10*, 2470-2480.

45. Diggle, J. W.; Downie, T. C.; Goulding, C. W. *Chem. Rev.* **1969**, *69*, 365.

46. Parkhutik, V. P.; Despic, A. *Modern Aspects of Electrochemistry*; Bockris, J. O. M., Ed.; Plenum Press: New York, **1989**; Vol. 20, Chapter 6.

47. Thompson, G. E.; Xu, Y.; Sheldon, P.; Shimizu, K.; Han, S.; Wood, G. C. *Philos. Mag. B* **1987**, *55*, 651.

48. Furneaux, R. C.; Rigby, W. R.; Davidson, A. P. *Nature* **1989**, *337*, 147-149.

49. Furneaux, R. C.; Rigby, W. R.; Davidson, A. P. ; US Patent Number , USA, 1987.

50. Masuda, H.; Fukuda, K. *Science* **1995**, *268*, 1466.

51. Li, A. P.; Muller, F.; Gosele, U. *Electrochemical and Solid State Letters* **2000**, *3*, 131-134.

52. Hoyer, P. *Adv. Mater.* **1996**, *8*, 857-859.

53. Calvert, P.; Rieke, P. *Chem. Mater.* **1996**, *8*, 1715-1727.

54. Addadi, L.; Weiner, S. *Angew. Chem. Int. Ed. Engl.* **1992**, *31*, 153-169.

55. Pileni, M.-P.; Ninham, B. W.; Gulik-Krzywicki, T.; Tanori, J.; Lisiecki, I.; Filankembo, A. *Adv. Mater.* **1999**, *11*, 1358-1361.

56. Possin, G. E. *Rev. Sci. Instrum.* **1970**, *41*, 772.

57. Jirage, K. B.; Hulteen, J. C.; Martin, C. R. *Science* **1997**, *278*, 655.

58. Jirage, K. B.; Hulteen, J. C.; Martin, C. R. *Anal. Chem.* **1999**, *71*, 4913-4918.

59. Yoshida, M.; Asano, M.; Safranj, A.; Omichi, H.; Spohr, R.; Vetter, J.; Katakai, R. *Macromolecules* **1996**, *29*, 8987-8989.

60. Hulteen, J. C.; Patrissi, C. J.; Miner, D. L.; Crosthwait, E. R.; Oberhauser, E. B.; Martin, C. R. *J. Phys. Chem. B* **1997**, *101*, 7727-7731.

61. Odom, T. W.; Huang, J.-L.; Kim, P.; Lieber, C. M. *J. Phys. Chem. B* **2000**, *104*, 2794-2809.

62. Park, C.; Anderson, P. E.; Chambers, A.; Tan, C. D.; Hidalgo, R.; Rodriquez, N. M. *J. Phys. Chem. B* **1999**, *103*, 10572-10581.

63. Kyotani, T.; Pradhan, B. K.; Tomita, A. *Bull. Chem. Soc. Japan* **1999**, *72*, 1957.

64. Owen, J. R. *Chem. Soc. Rev.* **1997**, *26*, 259-267.

65. Broussely, M.; Biensan, P.; Simon, B. *Electrochim. Acta* **1999**, *45*, 3-22.

66. Wilkinson, S. L. *C&E News* **1997**, *75*, 18-24.

67. Bruce, G.; Mardikian, P.; Marcoux, L. *J. Power Sources* **1997**, *65*, 149-153.

68. Erlich, G. M.; Marsh, C. *J. of Power Sources* **1998**, *73*, 224-228.

69. Halpert, G.; Frank, H.; Surampudi, S. *Electrochem. Soc. Interface* **1999**, *8*, 25-30.

70. Oman, H. *MRS Bulletin* **1999**, *24*, 33-39.

71. Scrosati, B. *J. Electrochem. Soc.* **1992**, *139*, 2776-2781.

72. Ozawa, K. *Solid State Ionics* **1994**, *69*, 212-221.

73. Brandt, K. *Solid State Ionics* **1994**, *69*, 173-183.

74. Jasinski, R. *High-Energy Batteries*; Plenum Press: New York, **1967**.

75. Holmes, C. F. *J. Power Sources* **1997**, *65*, xv-xx.

76. Brodd, R. J. *Electrochem. Soc. Interface* **1999**, *8*, 20-23.

77. Clark, W. D. K.; Syracuse, K. C.; Visbisky, M. *J. Power Sources* **1997**, *65*, 101-107.

78. Whittingham, M. S. *Science* **1976**, *192*, 1126-1127.

79. Chippindale, A. M.; Dickens, P. G.; Powell, A. V. *Prog. Solid State Chem.* **1991**, *21*, 133-198.

80. Vincent, C. A. Primary Lithium Cells. In *Modern Batteries*; Vincent, C. A., Scrosati, B., Ed.; John Wiley & Sons, Inc.: New York, **1997**, pp 107-141.

81. Armand, M. *Materials for Advanced Batteries*; Plenum Press: New York, **1980**.

82. Nagaura, T.; Tozawa, K. *Prog. in Batteries and Solar Cells* **1990**, *9*, 209-217.

83. Jacoby, M. *C&EN* **1998**, 37-43.

84. Scrosati, B. Rechargeable lithium cells. In *Modern Batteries*; Vincent, C. A. and Scrosati, B., Ed.; Arnold: London, **1997**, pp 198-242.

85. Matsumura, Y.; Wang, S.; Mondori, J. *J. Electrochem. Soc.* **1995**, *142*, 2914-2918.

86. Arora, P.; White, R. E.; Doyle, M. *J. Electrochem. Soc.* **1998**, *145*, 3647-3667.

87. Imanishi, N.; Takeda, Y.; Yamamoto, O. Development of the Carbon Anode in Lithium Ion Batteries. In *Lithium Ion Batteries*; Wakihara, M. and Yamamoto, O., Ed.; Wiley-VCH: New York, **1998**, pp 99-126.

88. Pistoia, G.; Antonono, A.; Rosati, R.; Zane, D. *Electrochimica Acta* **1996**, *41*, 2683-2689.

89. Linden, D. Basic Concepts. In *Handbook of Batteries*; Linden, D., Ed.; McGraw-Hill: New York, **1995**, pp 1.3-1.11.

90. McKinnon, W. R.; Haering, R. R. Physical Mechanisms of Intercalation. In *Modern Aspects of Electrochemistry*; White, R. E., Bockris, J. O. M. and Conway, B. E., Ed.; Plenum Press: New York, **1983**; Vol. 15, pp 235-304.

91. Weppner, W. Electrode Performance. In *Solid State Electrochemistry*; Bruce, P. G., Ed.; Cambridge University Press: Cambridge, **1995**, pp 199-228.

92. Goodenough, J. B. General Concepts. In *Lithium Ion Batteries: Fundametals and Performance*; Wakihara, M. and Yamamoto, O., Ed.; Wiley-VCH: New York, **1998**, pp 1-25.

93. McKinnon, W. R. Insertion electrodes I: Atomic and electronic structure of the hosts and their insertion compounds. In *Solid State Electrochemistry*; Bruce, P. G., Ed.; Cambridge University Press: Cambridge, **1995**, pp 175-180.

94. Gerischer, H.; Decker, F.; Scrosati, B. *J. Electrochem. Soc.* **1994**, *141*, 2297-2300.

95. Auborn, J. J.; Barberio, Y. L. *J. Electrochem. Soc.* **1987**, *134*, 638-641.

96. Berg, H. C. *Random Walks in Biology*; Princeton University Press: Princton, **1993**.

97. Bard, A. J.; Faulkner, L. R. *Electrochemical Methods*. John Wiley & Sons: New York, **1980**, pp 128-130.

98. Broadhead, J.; Kuo, H. C. Electrochemical Principles and Reactions. In *Handbook of Batteries*; Linden, D., Ed.; McGraw-Hill: New York, **1995**, pp 2.16-2.18.

99. Tran, T. D.; Feikert, J. H.; Pekala, R. W.; Kinoshita, K. *J. Appl. Electrochem.* **1996**, *26*, 1161-1167.

100. Mamedov, E. A.; Corberan, V. C. *Appl. Catal. A General* **1995**, *127*, 1-40.

101. Chary, K. V. R.; Kishan, G.; Bhaskar, T.; Sivaraj, C. *J. Phys. Chem. B* **1998**, *102*, 6792-6798.

102. Micocci, G.; Serra, A.; Tepore, A.; Capone, S.; Rella, R.; Siciliano, P. *J. Vac. Sci. Technol. A* **1997**, *15*, 34-38.

103. Livage, J. *Chem. Mater.* **1991**, *3*, 578-593.

104. Zhang, J.-G.; Benson, D. K.; Tracy, C. E.; Deb, S. K.; Czanderna, A. W.; Crandall, R. S. *J. Electrochem. Soc.* **1994**, *141*, 2795-2800.

105. Potiron, E.; Salle, A. L.; Verbaere, A.; Piffard, Y.; Guyomard, D. *Electrochim. Acta* **1999**, *45*, 197-214.

106. West, K.; Zachau-Charistiansen, B.; Jacobsen, T.; Skaarup, S. *Solid State Ionics* **1995**, *76*, 15-21.

107. Barreca, D.; Armelao, L.; Caccavale, F.; Noto, V. D.; Gregori, A.; Rizzi, G. A.; Tondello, E. *Chem. Mater.* **2000**, *12*, 98-103.

108. Zhang, J.-G.; Liu, P.; Turner, J. A.; Tracy, C. E.; Benson, D. K. *J. Electrochem. Soc.* **1998**, *145*, 1889-1892.

109. Hench, L. L.; Orefice, R. Sol-gel Technology. In *Kirk-Othmer Encyclopedia of Chemical Technology*; Kroshcwitz, J. I. and Howe-Grant, M., Ed.; John-Wiley & Sons: New York, **1997**; Vol. 22, pp 497-528.

110. Mehrotra, R. C.; Singh, A. *Chem. Soc. Rev.* **1996**, *25*, 1-76.

111. Livage, J.; Henry, M.; Sanchez, C. *Prog. Solid St. Chem.* **1988**, *18*, 259-341.

112. Oh, I.; Hong, S.; Sun, Y. *J. Mater. Sci.* **1997**, *32*, 3177-3182.

113. Bach, S.; Henry, M.; Baddier, N.; Livage, J. *J. Solid State Chem.* **1990**, *88*, 325-333.

114. Hamasaki, Y.; Ohkubo, S.; Murakami, K.; Sei, H.; Nogami, G. *J. Electrochem. Soc.* **1994**, *141*, 660-663.

115. Nabavi, M.; Doeuff, S.; Sanchez, C.; Livage, J. *Mat. Sci. & Eng. B3* **1989**, *3*, 203-207.

116. Ozer, N. *Thin Solid Films* **1997**, *305*, 80-87.

117. Davies, A.; Hobson, R. J.; Hudson, M. J.; Macklin, W. J.; Neat, R. J. *J. Mater. Chem.* **1996**, *6*, 49-56.

118. Braithwaite, J. S.; Catlow, C. R. A.; Gale, J. D.; Harding, J. H. *Chem. Mater.* **1999**, *11*, 1990-1998.

119. Cocciantelli, J. M.; Doumerc, J. P.; Pouchard, M.; Broussely, M.; Labat, J. *J. Power Sources* **1991**, *34*, 103-111.

120. Murphy, D. W.; Christian, P. A.; Disalvo, F. J.; Waszczak, J. V. *Inorg. Chem.* **1979**, *18*, 2800-2803.

121. Weast, R. C. *CRC Handbook of Chemistry and Physics*; 66 ed.; Weast, R. C., Ed.; CRC Press, Inc.: Boca Raton, 1986, pp F164.

122. Garcia, M. E.; Garofalini, S. H. *J. Electrochem. Soc.* **1999**, *146*, 840-849.

123. McGraw, J. M.; Bahn, C. S.; Parilla, P. A.; Perkins, J. D.; Readey, D. W.; Ginley, D. S. *Electrochim. Acta* **1999**, *45*, 187-196.

124. Shembel, E.; Apostolova, R.; Nagirny, V.; Aurbach, D.; Markovsky, B. *J. Power Sources* **1999**, *81-81*, 480-486.

125. Vivier, V.; Farcy, J.; Pereira-Ramos, J. *Electrochim. Acta* **1998**, *44*, 831-839.

126. Whittingham, M. S. *Prog. Solid. St. Chem.* **1978**, *12*, 41-99.

127. Dickens, P. G.; French, S. J.; Hight, A. T.; Pye, M. F. *Mat. Res. Bull* **1979**, *14*, 1295-1299.

128. Ceder, G.; Ven, A. V. d. *Electrochim. Acta* **1999**, *45*, 131-150.

CHAPTER 2

SOL-GEL BASED TEMPLATE SYNTHESIS AND LI-INSERTION RATE PERFORMANCE OF NANOSTRUCTURED VANADIUM PENTOXIDE

Introduction Lithium-ion batteries posses high energy density and are promising candidates for applications where high power density is required. Energy density (Equation 2.1)

$$E = \frac{Q\,V}{\text{Volume}} \qquad (2.1)$$

is the product of the total charge stored by the battery (Q) and the discharge voltage (V) normalized by battery volume. At high discharge current, the quantity of electricity that is delivered by the battery, e.g. battery capacity, is critically dependent on the size and shape of the Li-insertion material particles used to prepare the electrodes and on the morphology of the electrode.[1-5] Auborn and Barberio were among the first to show that decreasing the size of the Li-insertion material particles increases electrode capacity at high discharge current.[1] More recently the effect of insertion-material particle size on electrode rate capability was investigated by using the template synthesis method[6,7] to prepare nanostructured electrode materials. These nanostructured electrodes consist of an ensemble of tubular or fibrillar particles of the Li-insertion material which protrude from a current

collector surface like the bristles of a brush. The template method allows for precise control of both the diameter and length of the tubules or fibrils that make up the nanostructured electrodes. These studies explored the rate capabilities of nanostructured TiS_2[2] and $LiMn_2O_4$[3] electrodes prepared via the template-synthesis method.

In these prior investigations, the rate capabilities of the nanostructured electrodes were compared with the rate capabilities of thin-film electrodes containing the same type and quantity of the electrode material. Constant current discharge experiments showed that the nanostructured electrodes delivered higher capacities, at high discharge currents, than the thin-film electrodes. This is because, for the nanostructured electrode, the Li^+ diffusion distances are shorter and the surface areas are higher. Diffusion distance and surface area dramatically affect rate capability because Li^+ diffusion within the electrode material is slow.[8] During the discharge process (Equation 2.2) Li^+ ions and electrons insert into the atomic lattice and electronic structure, respectively, of the insertion material in the cathode. At high discharge rate, high Li^+ insertion-flux density and slow Li^+ transport result in concentration polarization of Li^+ within the electrode material. This causes a drop in cell voltage which results in termination of the discharge before the maximum capacity of the electrode material is utilized.[9] Decreasing the average diffusion distance, while keeping the mass constant, increases the surface area of the electrode and lowers current density. This results in the delay of concentration polarization to higher current values and, consequently, increased electrode rate capability.

Sol-gel chemistry is a simple and efficient route for preparing inorganic compounds such as glasses and ceramics.[10] Recently sol-gel chemistry and template synthesis were combined to prepare micro- and nanostructures of inorganic oxides such as TiO_2, WO_3 and ZnO.[11] In the work described here a sol-gel template method is used to prepare nanostructured electrodes of crystalline V_2O_5. Galvanostatic experiments were used to explore the rate capabilities of the nanostructured electrodes relative to thin-film control electrodes of the same material. The Li^+ storage capacities of the nanostructured and thin-film electrodes are equivalent at slow discharge rates (C/20). However, the capacity of the nanostructured electrode is 3 to 4 times higher at discharge rates above between 200 and 1190C. In addition, it is believed that the specific power of the nanostructure is the highest yet reported for a Li-insertion electrode.

EXPERIMENTAL

Template Synthesis of the V_2O_5 Nanofibers. Template synthesis is a general method for preparing nanomaterials.[6,7] Briefly, template synthesis entails deposition of the material of interest, or a precursor for that material, into the pores of a microporous template membrane. The templates used here were polycarbonate filtration membranes (Poretics, Inc.) with a nominal pore diameter of 50 nm. The pores are cylindrical, nearly monodisperse in diameter and extend through the thickness (6 μm) of the template membrane.

It is well known that crystalline V_2O_5 and other vanadium oxides can be prepared by the sol-gel route via hydrolysis and condensation of alkoxide

precursors.[12] Sol-gel chemistry and template synthesis were combined to prepare the nanostructured crystalline V_2O_5 electrodes. Figure 1 shows a schematic of this template synthesis procedure. A 1.5 cm^2 section of template membrane was placed on a Pt current collector (1.5 x 3 cm) in a glove box purged with argon. Next, a microliter syringe was used to apply 0.6 μL of the V_2O_5 precursor, triisopropoxyvanadium (V) oxide (TIVO) (Strem Chemical, > 98%) to the template membrane surface. The TIVO filled the pores in the template membrane and the space between the membrane and the underlying Pt current collector.

Hydrolysis of TIVO in air is extremely fast and this resulted in cracking of the nascent V_2O_5 nanofibers forming within the template membrane. In order to prevent this, hydrolysis of the precursor was carried out in a glove box under very low water partial pressures. The reaction was allowed to proceed for 12 hours which resulted in the formation of nanofibers of a TIVO gel. After gel formation, the composite was removed from the glove box and heated in air at 80 °C for 2 hours. The template membrane was then removed with an oxygen plasma (15 watts rf power, 100 mTorr O_2, 2 hours). Finally, dehydration and condensation of the precursor to crystalline V_2O_5 was accomplished by heating at 400 °C for 10 hours in 150 psi O_2.

Preparation of the Thin Film Control Electrodes. Thin film control electrodes were prepared by depositing liquid TIVO onto a Pt foil current collector. This was done as above using a glass micropipette to spread the precursor evenly over the Pt foil surface. Again, hydrolysis proceeded for 12 hours in the glove box

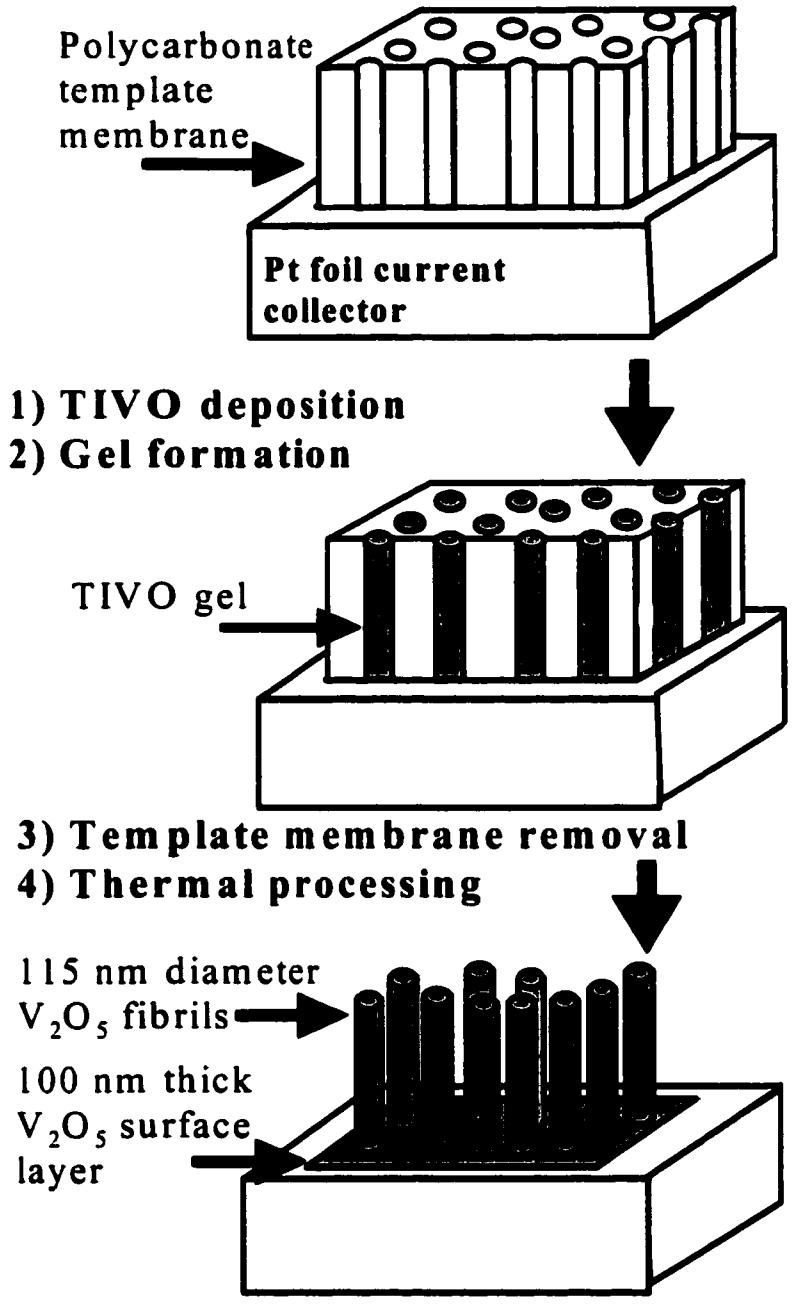

Figure 2.1. Schematic of template synthesis method used to prepare the nanostructured V_2O_5 electrodes. The V_2O_5 precursor was TIVO. Polycarbonate microporous filtration membranes were used as templates.

after which time the liquid had hydrolyzed to a yellow film of TIVO gel. In order to make the geometric area of the thin film control electrode approximately equal to that of the nanostructured electrode, all but 1.4 cm^2 of the TIVO gel film was removed with a water-wet cotton swab. The TIVO gel/Pt composite was then thermally treated in the same way as the nanostructured electrode.

Characterization. V_2O_5 morphology and crystallinity were investigated with a Phillips 505 scanning electron microscope and a Phillips powder X-ray diffractometer (Cu Kα). V_2O_5 mass was determined after all electrochemical experiments were completed by immersing the electrode in 2M H_2SO_4, followed by analysis for vanadium content with a Perkin Elmer Plasma 400 atomic emission spectrometer.

Chronopotentiometry and cyclic voltammetry were performed under argon using a three electrode cell. Li foil counter and reference electrodes were used. The electrolyte was 1M $LiClO_4$ in a 7:3 (v/v) mixture of diethyl carbonate (99%, Aldrich) and ethylene carbonate (battery grade, Ferro Corp.); both solvents were used as received. Chronopotentiometric data was acquired using an EG&G model 263A potentiostat/galvanostat and model 270/250 research electrochemistry software. Cyclic voltammetry was performed with a Bioanalytical Systems CV-27 voltammograph between the voltage limits 3.80 and 2.50 V (vs. Li/Li^+).

RESULTS AND DISCUSSION

Morphology and Crystallinity. Figure 2 shows scanning electron micrographs of a typical nanostructured V_2O_5 electrode. Figure 2A is a lower

Figure 2.2. SEM images of the components of a nanostructured electrode. **A.** Low magnification image of the V_2O_5 nanofibrils. **B.** High magnification image of the nanofibrils. **C.** The underlying V_2O_5 surface layer.

magnification image that shows the V_2O_5 fibrils dispersed across the surface of this nanostructured electrode. Figure 2.2B is a higher magnification image that was used to determine the average length and diameter of the V_2O_5 nanofibrils. The average length was 2 ± 0.25 μm and the average diameter was 115 ± 14 nm. This diameter is more than the nominal diameter of the pores in the template (50 nm as reported by the manufacturer). Such larger-than-expected nanofibril diameters have been observed previously with these polycarbonate template membranes.[13,14] Two explanations have been proposed – that the pore expands during formation of the nanofibril[14] and that the pore diameter is smaller at the surface of the membrane than in the middle[13].

As noted above, the V_2O_5 nanofibrils protrude from a V_2O_5 surface film. This surface film results because the TIVO precursor fills the space between the membrane and the Pt current collector surface. An SEM image of this surface layer is shown in Figure 2.2C. The fibrils that had been attached to this section of the surface layer were removed by lightly brushing with a dry cotton swab. The surface layer is continuous and relatively smooth. Images like that shown in Figure 2.2C were used to obtain the average thickness of the V_2O_5 surface layer. An average thickness of 97 ± 20 nm was obtained.

The length and diameter of the fibrils along with the average thickness of the surface layer allow for a calculation of the relative volumes of the V_2O_5 nanofibrils and the V_2O_5 surface layer. This calculation showed that the volume of the nanofibrils is 1.25 times the volume of the surface layer. This is important because during the charge/discharge experiments (see below) Li^+ intercalates into both the

fibrils and the surface film. Li^+ that intercalates into the fibrils must diffuse approximately 57 nm (the radius of the fibrils), whereas Li^+ that intercalates into the surface film must diffuse approximately 97 nm (the thickness of the film). As we will see below, both of these diffusion distances are small relative to the corresponding distance in the thin film control electrode (Table I).

The thin-film control electrodes represent a more conventional electrode configuration, for example like those developed for thin-film lithium micro-batteries.[15-17] An SEM image of the thickness of such an electrode is shown in Figure 2.3. This image was obtained by bending the underlying Pt foil current collector to 180° and examining the fractured film edge. Images of this type have shown that the thin-film control electrodes are 250 ± 30 nm in thickness. In addition to SEM, profilometry was used to confirm that the film thickness was ≈ 250 nm. Table I shows the important physical characteristics of the electrodes used in this study. The surface area of the thin-film control electrode was calculated from the geometric area of 1.4 cm^2 (1.0 cm x 1.4 cm) and the known mass of the film.

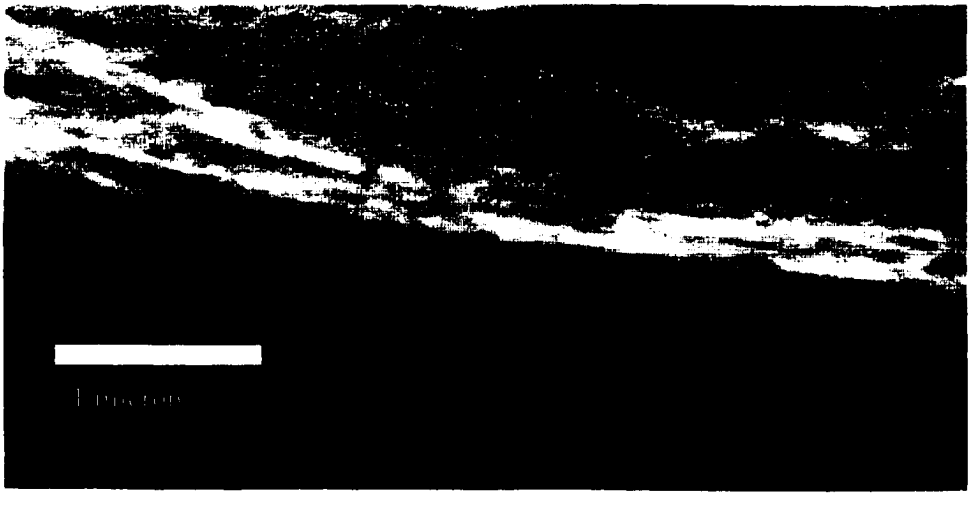

Figure 2.3. Edge view of a typical V_2O_5 thin film control electrode.

Table 1.1. Characteristics of the Nanostructured and Thin-Film Control Electrodes

Electrode Description	V_2O_5 Mass (μg)	V_2O_5 Surface Area ($m^2 g^{-1}$)	Li^+ Diffusion Distance
Nanostructured	99.7	8.0	Surface Layer ca. 100 nm Nanofibrils ca. 57 nm
Thin Film	92.0	1.5	ca. 250 nm

The calculation of the surface area of the nanofibril electrode was based on an average fibril length of 2 μm, a fibril density of $6x10^8$ fibrils cm^{-2}, an average fibril diameter of 115 nm, and the geometric area of the membrane used, 1.5 cm^2. As shown in Table I, the nanostructured electrodes have both higher surface area and shorter Li^+ diffusion distances than the thin-film control electrode. As will be shown below, both of these features allow for greater rate capabilities for the nanostructured electrode.

BET[18] analysis is a well-known and accurate method for determining the surface area of structured materials. The low mass of the nanostructured V_2O_5 , however, is below the detection limit of current instruments. Thus a direct measurement of the surface area of the nanostructure and thin-film specimens was not possible. It is possible that the alcohol which evaporates during hydrolysis of the TIVO may result in a significantly roughened or even porous V_2O_5 surface on a scale that is not detectable by SEM. Thus the calculated values of surface area shown in Table 1 should be considered as approximations and used for a relative comparison of nanostructure and thin-film surface areas.

Powder X-ray diffraction (XRD) patterns for the thin-film control and nanostructured electrodes are shown in Figure 2.4A and 2.4B, respectively. The expected powder pattern for orthorhombic V_2O_5 is shown in Figure 2.4C for comparison.[19] Note that the intensity ratios of the peaks for both the nanostructured and the thin-film V_2O_5 do not correspond exactly to the expected pattern for orthorhombic V_2O_5. The larger than expected 001 peaks in Figure 2.4A and 2.4B indicate that a majority of the crystallites are oriented with their "a" and "b" axes parallel to the surface of the Pt current collector. This preferred orientation is especially pronounced for the thin-film V_2O_5 electrode where the 001 peak is observed almost exclusively (Figure 2.4A). Similar results have been reported previously for V_2O_5 thin films prepared from alkoxides.[20] The starred peaks in Figure 2.4B are due to impurities within the sample chamber.

Electrochemistry. The charge and discharge reactions for V_2O_5 can be written as follows (Equation 2.2):

$$xLi^+ + xe^- + V_2O_5 \underset{\text{charge}}{\overset{\text{discharge}}{\rightleftharpoons}} Li_xV_2O_5 \qquad (2.2)$$

Figure 2.5 shows constant current charge and discharge curves for the nanofibrillar electrode (Figure 2.5A) and the thin-film electrode (Figure 2.5B) at low discharge and charge rates (approximately C/20). The shapes of the discharge curves are similar to those reported previously for Li^+-intercalation into orthorhombic V_2O_5 at low discharge and charge rates.[21-23] For the electrochemical cell used here, cell

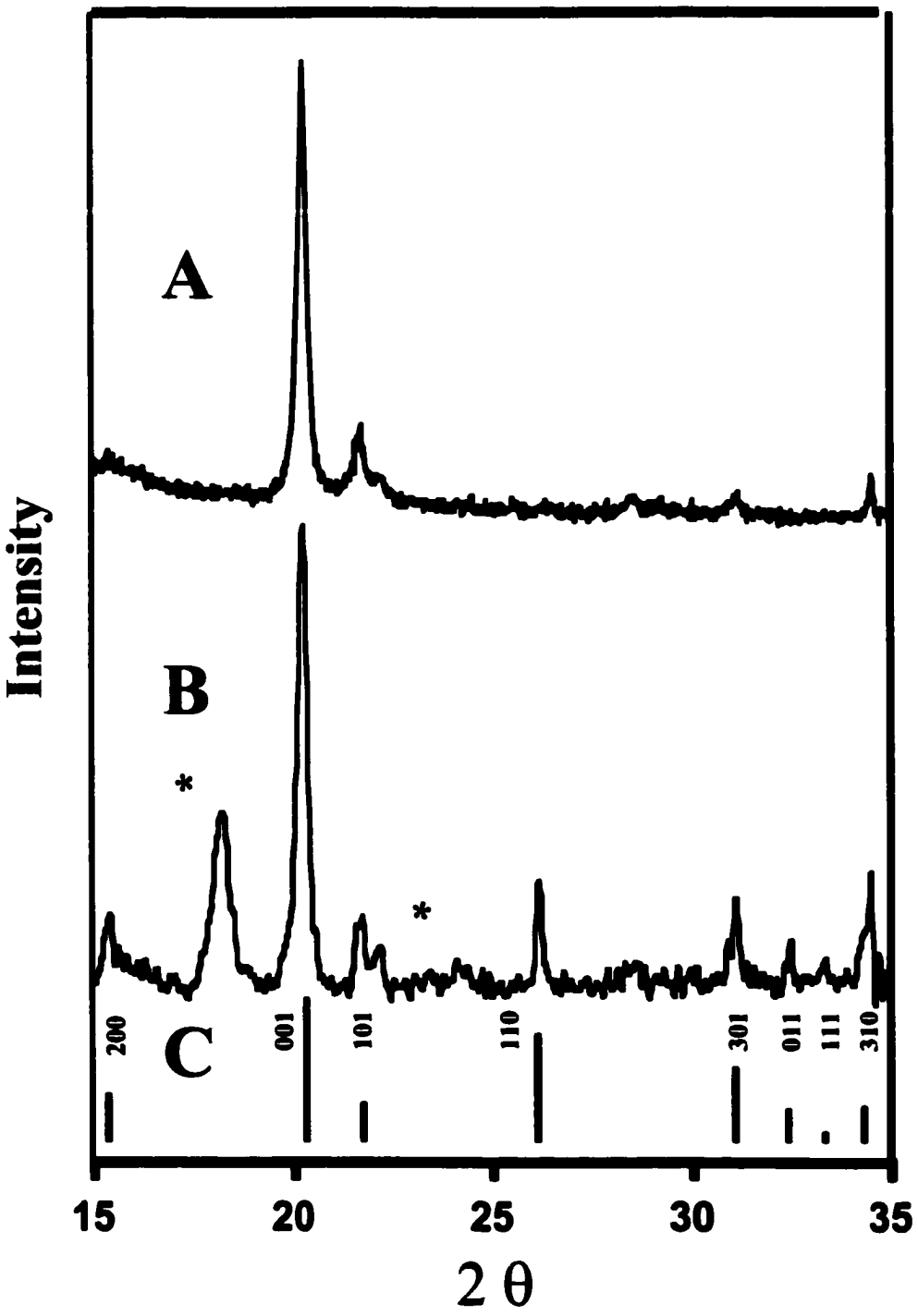

Figure 2.4. X-ray diffraction pattern for thin-film (A) and nanostructured (B) V_2O_5 electrodes on Pt. The vertical lines (C) show the XRD pattern for orthorhombic V_2O_5 as given in ref. 19.

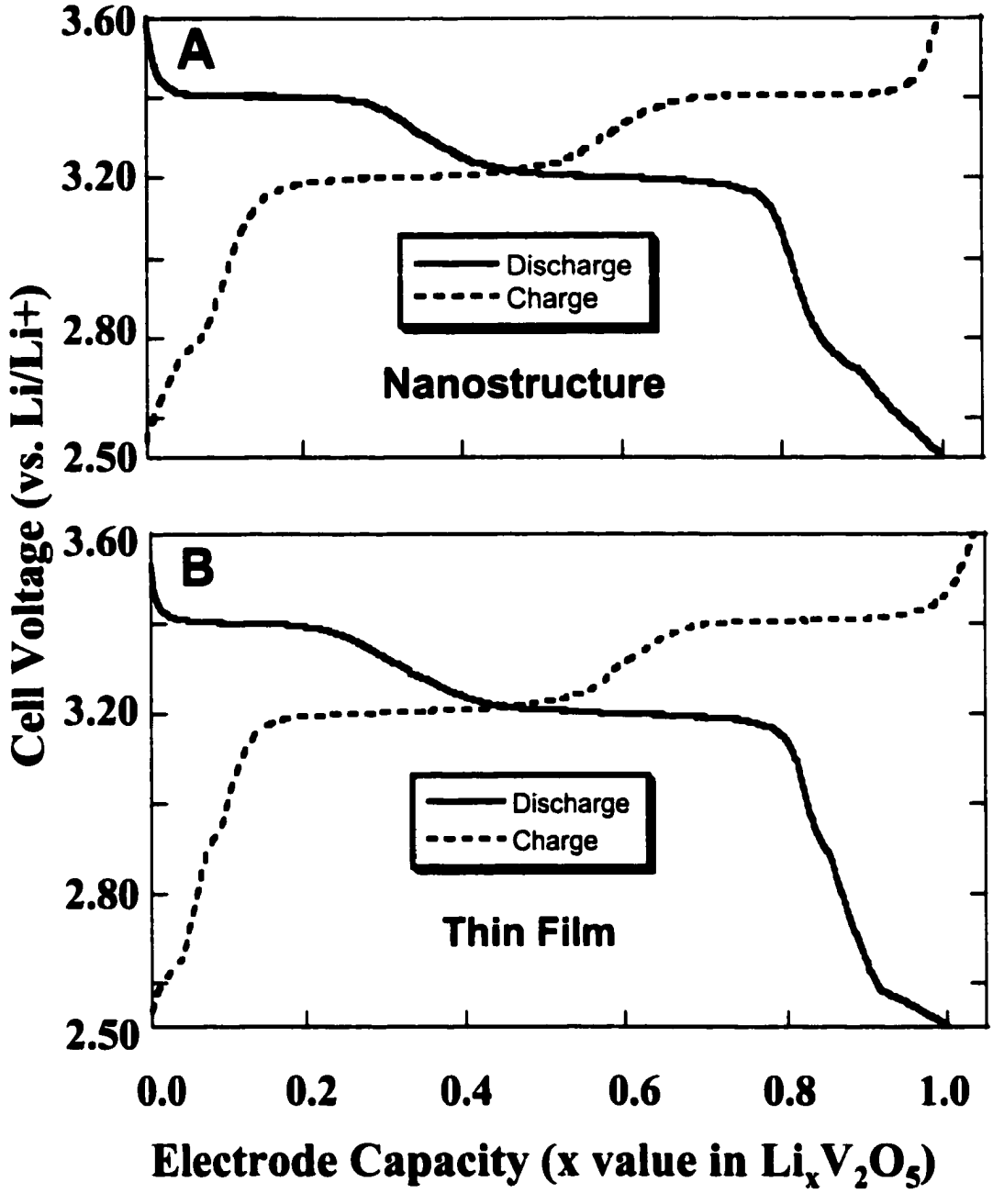

Figure 2. 5. Galvanostatic discharge and charge curves for nanostructured (A) and thin-film (B) V_2O_5 electrodes at C/20.

voltage is related to the chemical potential of Li in V_2O_5 by

$$E = (\mu_o - \mu)/F \qquad (2.3)$$

where E is the measured cell voltage, μ_o and μ are the chemical potentials of lithium at the surfaces of the reference electrode and V_2O_5, respectively, and F is Faraday's constant.[9] According to Equation 2.3, the areas of sloping cell voltage in Figure 4 are caused by a change in Li chemical potential with quantity of Li^+ intercalated. Previous reports[21,22] show that these regions of sloping voltage correspond to $Li_xV_2O_5$ compositions where only a single crystalline phase exists. Therefore, μ and cell voltage change with the activity of Li in the V_2O_5. The plateaus are compositions where two crystalline phases co-exist in equilibrium. Because of the two-phase equilibrium, μ and cell voltage are independent of composition.

Galvanostatic intermittent titration experiments[21] and open-circuit voltage[22] experiments have shown that when a cutoff voltage of 2.50 vs. Li/Li^+ is used, the maximum value of x in Equation 1 for orthorhombic V_2O_5 is $x = 1$. This corresponds to a capacity of 147 mAh g^{-1} V_2O_5. This was confirmed for the electrodes used here by measuring the discharge capacities for five nanostructured electrodes and three thin-film electrodes at low discharge rates (between C/19 and C/23). The means and standard deviations of these results were $x = 1.05 \pm 0.04$ for the nanofibrillar electrodes and $x = 1.01 \pm 0.05$ for the thin film controls.

"C rate" is a method of expressing the charge or discharge rate of an electrochemical cell or battery. C rate normalizes the discharge current according to capacity. This normalization allows the comparison of electrochemical

performance at equivalent ("C") rates of charge or discharge for cells of significantly different capacities. For example, a cell discharging at a C rate "x" will deliver its nominal rated capacity in 1/x hours. For an electrode with a nominal capacity of 2 Ah, discharge at a rate of C/1 corresponds to a discharge current of 2A, a rate of C/10 to 0.2 A and so on. Since battery capacity is a function of discharge rate, it is important to specify the C rate at which the nominal capacity of the battery or cell was determined. For example, a C/10 discharge rate for a battery with a 2 Ah nominal capacity which was rated at 1 A would be shown as $0.1C_{0.5}$.

In order to completely characterize the rate capabilities of these various electrodes, 15 complete charge and discharge cycles, at various rates, were conducted on each electrode. A major concern, however, was that the capacity of the electrode might fade during these 15 charge/discharge cycles.[24] This would make interpretation of the dependence of capacity on discharge rate (Figure 2.8) more difficult. It was determined that the capacity of the first and fifteenth discharge (both performed at low discharge rate) were the same within experimental error.

To further explore this issue of capacity fade, cyclic voltammetric experiments were done on a second set of nanostructured and thin-film electrodes. These electrodes were cycled at a scan rate of 1.00 mV s^{-1} between the limits of 3.80 V and 2.50 V. After each scan, the potential was held at 3.80 V until the current decayed to the first scan value. The data obtained are shown in Figure 2.6. After 40 complete discharge/charge cycles, the nanostructured electrode had 93% of its initial (first-cycle) capacity. The thin-film electrode retained 89% of its initial capacity. Electrode rate capability was studied by following discharge capacity with

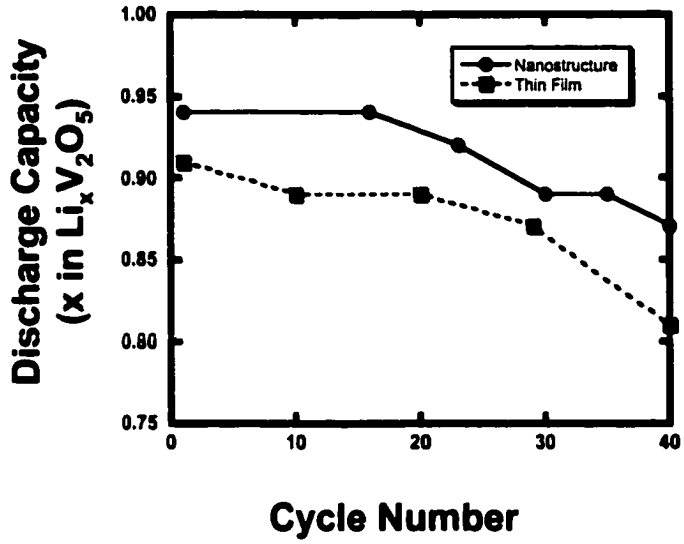

Figure 2.6. Electrode discharge capacity as a function of cycle number. Data were obtained via cyclic voltammetry as explained in the text.

increasing discharge rate, Figure 2.7. Figure 2.7 shows electrode capacity vs. cell voltage at various discharge rates for the nanostructured electrode (2.7A) and the thin-film control electrode (2.7B). The current densities used for the nanostructured electrode were from 0.47 μA cm^{-2} (C/20) to 13.3 mA cm^{-2} (1361C) and for the thin film electrode were from 0.48 μA cm^{-2} (C/20) to 11.4 mA cm^{-2} (1190C). Both the nanofibrillar and thin-film control electrodes show the experimental maximum capacity of x = 1 at low discharge rates (C/20). However, Figure 2.7 also shows that increasing the discharge rate reduces the degree of lithium insertion and thus the discharge capacity of the electrodes. In general, the data show that the discharge capacity of the nanostructured electrode remains higher, at high discharge rate, than the discharge capacity of the thin-film electrode. As has been discussed in our previous work,[2,3] this is due to the shorter Li^+ diffusion distance

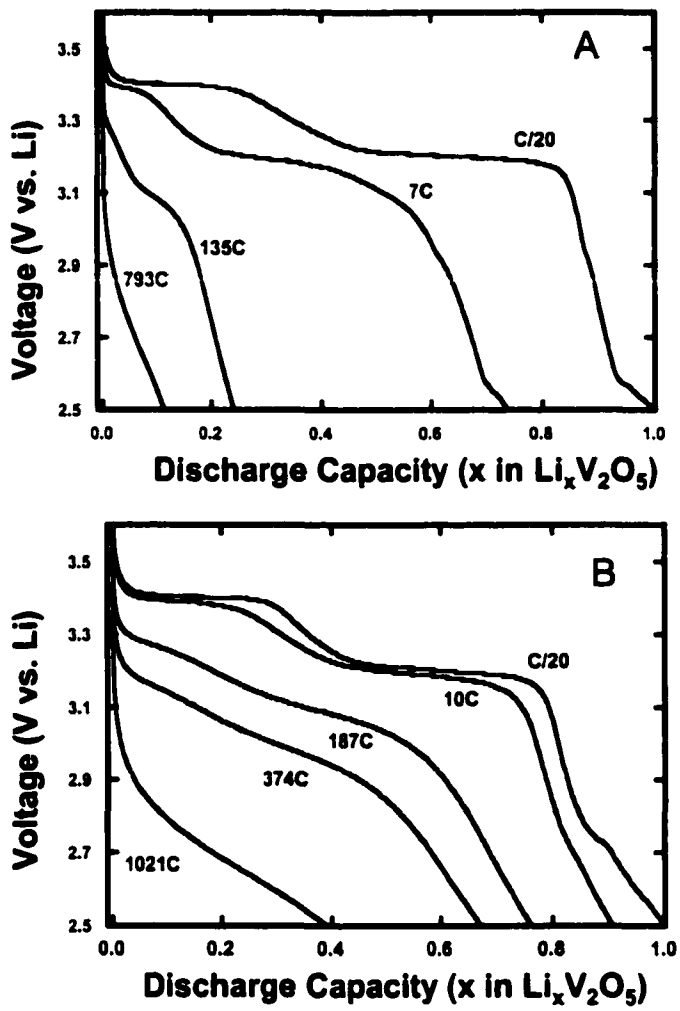

Figure 2.7. Cell voltage vs. capacity for nanostructured (7A) and thin-film (7B) electrodes at various discharge rates. $Li_{1.0}V_2O_5$ is equivalent to a discharge capacity of 147 $mAhg^{-1}$

and higher surface area (Table I) of the fibrillar material relative to the thin-film control. Higher surface area is important because it lowers Li^+ insertion-rate density during the discharge process. This lower insertion rate delays the capacity loss associated with concentration polarization to higher discharge currents.

In order to conduct multiple experiments, the electrodes were "recharged" after each discharge experiment. This was accomplished using a positive voltammetric scan from the open circuit potential to 3.80 V (vs. Li) at a sweep rate of 0.20 mV s^{-1}. The electrode was held at this potential until the current decreased to the first scan value. In all experiments the anodic capacity measured during the voltammetric sweep was equivalent to the discharge capacity. This shows that the discharge capacity was 100% faradaic.

A more direct comparison of the rate capability of the nanostructured and thin-film electrodes is shown in Figure 2.8. The data points shown in this figure were obtained from the discharge capacity values shown in Figure 2.7 at a voltage cutoff of 2.50 V. The capacity of the nanofibrillar electrode is approximately 3 times higher at a discharge rate of 200C and increases to 4 times higher at discharge rates between 500 and 1190C. Figure 2.8, then, clearly shows the rate capability advantages of the nanostructured electrode due to higher surface area and smaller diffusion distances

CONCLUSION

This work demonstrates a simple and efficient template synthesis method for the preparation of nanofibrillar, orthorhombic V_2O_5 electrodes. Investigation of the rate capabilities of these electrodes shows that the nanofibrillar electrodes can deliver higher capacities, at high discharge currents, relative to a thin-film control electrode. The ultimate goal for battery and electrode performance is high energy output at both low and high power. At low specific power (22 mW g^{-1} V_2O_5), the

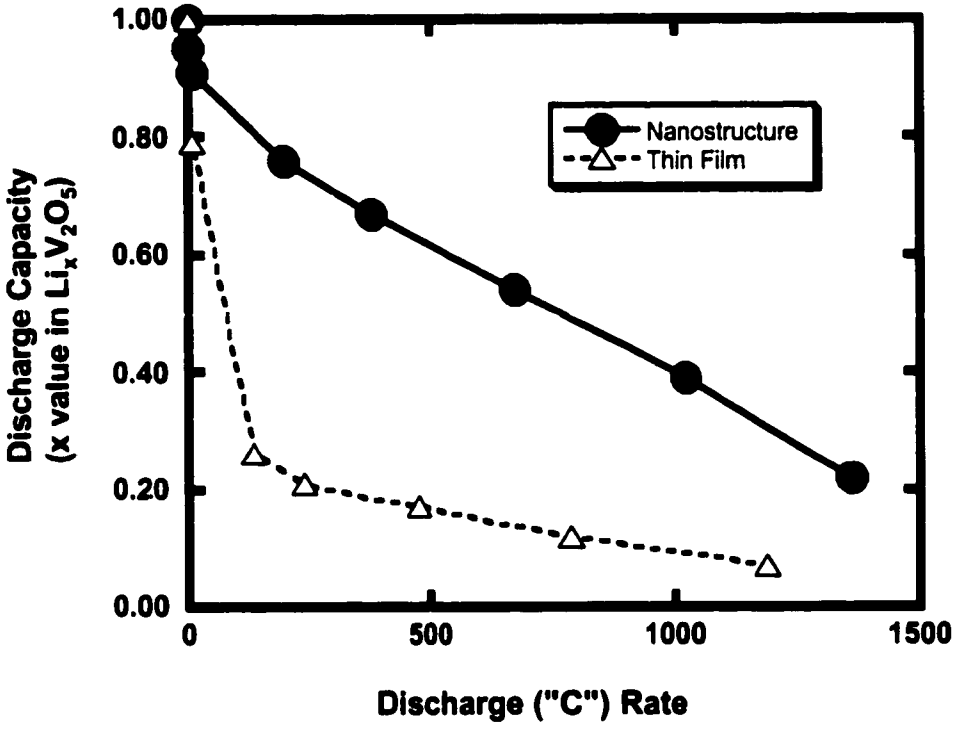

Figure 2.8. Discharge capacity of typical nanostructured and thin-film electrodes as a function of galvanostatic discharge rate.

nanostructured electrode shown here delivered the expected maximum specific energy of approximately 467 mWh g^{-1} V_2O_5. These values were calculated from the results of a constant current experiment where the discharge rate was C/21 (700 nA), the mean discharge voltage was 3.167 V, the electrode capacity was $Li_{1.0}V_2O_5$ and the cutoff voltage was 2.500 vs. Li/Li^+. At extremely high power (534 W g^{-1} V_2O_5) the energy output was 85 mWh g^{-1} V_2O_5. The discharge rate for this experiment was 1361C (20 mA) and the mean discharge voltage was 2.662 V. These results show that the nanostructured V_2O_5 is capable of useful specific energy even at extremely high specific power.

In addition to useful specific energy at high specific power, a practical battery electrode must also have high volumetric energy density. From this point of view, the electrodes prepared here must be viewed as experimental systems meant to explore the specific power capabilities of the nanostructured electrode concept. This is because these nanostructured electrodes were prepared from template membranes with low porosity and, therefore, low fibril density. It is important to point out, however, that nanostructured electrodes with 30 to 50 times higher volumetric energy density could be prepared using template membranes with higher porosity. For example, the templates used for this fundamental study contain a total pore volume that is approximately 1.2% of the volume of the membrane. We have prepared template membranes in our lab with porosities as high as 30%.[25] In addition, templates have been reported in the literature with porosities of approximately 50%.[26] The next phase of this project will use such high porosity membranes to prepare nanostructured electrodes with higher V_2O_5 volumetric densities.

REFERENCES FOR CHAPTER 2

1. Auborn, J. J.; Barberio, Y. L. *J. Electrochem. Soc.* **1987**, *134*, 638-641.

2. Che, G.; Jirage, K. B.; Fisher, E. R.; Martin, C. R. *J. Electrochem. Soc.* **1997**, *144*, 4296-4302.

3. Nishizawa, M.; Mukai, K.; Kuwabata, S.; Martin, C. R.; Yoneyama, H. *J. Electrochem. Soc.* **1997**, *6*, 1923-1927.

4. Tipton, A. L.; Passerini, S.; Owens, B. B.; Smyrl, W. H. *J. Electrochem. Soc.* **1996**, *143*, 3473-3477.

5. Tran, T. D.; Feikert, J. H.; Pekala, R. W.; Kinoshita, K. *J. Appl. Electrochem.* **1996**, *26*, 1161-1167.

6. Martin, C. R. *Science* **1994**, *266*, 1961-65.

7. Martin, C. R. *Accounts of Chemical Research* **1995**, *28*, 61.

8. Scrosati, B. *J. Electrochem. Soc.* **1992**, *139*, 2776-2781.

9. Owen, J. R. *Chem. Soc. Rev.* **1997**, *26*, 259-267.

10. Livage, J.; Henry, M.; Sanchez, C. *Prog. Solid St. Chem.* **1988**, *18*, 259-341.

11. Lakshmi, B. B.; Dorhout, P. K.; Martin, C. R. *Chem. Mater.* **1997**, *9*, 857-862.

12. Nabavi, M.; Sanchez, C.; Livage, J. *Eur. J. Solid State Inorg. Chem.* **1991**, *28*, 1173-1192.

13. Schonenberger, C.; Zande, B. M. I. v. d.; Fokkink, L. G. J.; Henny, M.; Schmid, C.; Kruger, M.; Bachtold, A.; Huber, R.; Birk, H.; Staufer, U. *J. Phys. Chem. B* **1997**, *101*, 5497-5505.

14. Wang, L.; Yu-Zhang, K.; Metrot, A.; Bonhomme, P.; Troyon, M. *Thin Solid Films* **1996**, *288*, 86-89.

15. Liu, P.; Zhang, J.-G.; Turner, J. A.; Tracy, C. E.; Benson, D. K.; Bhattacharya, R. N. *Solid State Ionics* **1998**, *111*, 145-151.

16. Jones, S. D.; Akridge, J. R. *Solid State Ionics* **1996**, *86-88*, 1291-1294.

17. Bates, J. B.; Gruzalski, G. R.; Dudney, N. J.; Luck, C. F.; Yu, X.-H.; Jones, S. D. *Solid State Technology* **1993**, *36*, 59-64.

18. Brunauer, S.; Emmett, P. H.; Teller, E. *J. Am. Chem. Soc.* **1938**, *60*, 309-319.

19. *Index to the X-ray Powder Data File*; American Society for Testing and Materials.: Philadelphia, 1962; Vol. card# 9-387.

20. Livage, J. *Chem. Mater.* **1991**, *3*, 578-593.

21. Delmas, C.; Cognac-Auradou, H.; Cocciantelli, J. M.; Menetrier, M.; Doumerc, J. P. *Solid State Ionics* **1994**, *69*, 257-264.

22. Dickens, P. G.; French, S. J.; Hight, A. T.; Pye, M. F. *Mat. Res. Bull.* **1979**, *14*, 1295-1299.

23. Vivier, V.; Farcy, J.; Pereira-Ramos, J.-P. *Electrochimica Acta* **1998**, *44*, 831-839.

24. Bates, J. B.; Gruzalski, G. R.; Dudney, N. J.; Luck, C. F.; Yu, X. *Solid State Ionics* **1994**, *70/71*, 619-628.

25. Foss, C. A.; Hornyak, G. L.; Stockert, J. A. *J. Phys. Chem.* **1994**, *98*, 2963-2971.

26. Masuda, H.; Fukuda, K. *Science* **1995**, *268*, 1466-1468.

CHAPTER 3

IMPROVING THE VOLUMETRIC CAPACITIES OF NANOSTRUCTURED V_2O_5 ELECTRODES PREPARED USING MEMBRANE-BASED TEMPLATE SYNTHESIS

INTRODUCTION

The power performance of Li ion battery electrodes depends on the size of the particles making up the electrodes and on electrode surface area.[1-7] To better understand these effects, we have been investigating the rate properties of Li-insertion electrodes prepared with monodisperse nanoscopic particles.[1,3,4,6] These electrodes were prepared using a method called membrane-based template synthesis,[8,9] which entails deposition of the material of interest, or a suitable precursor, within the nanometer-sized pores of a porous template membrane. This method yields electrodes that consist of nanometer-diameter fibrils or tubules of the insertion material which protruded from a current collector like the bristles of a brush. [1,3,4,6] Such nanostructured electrodes have higher rate capabilities than thin-film control electrodes composed of the same material. This is because the distance Li^+ must diffuse in the nanoparticle is smaller and because the surface area of the nanostructured electrode is larger. Both effects

delay concentration polarization to higher discharge currents, resulting in better rate capabilities and higher electrode capacity at high discharge rates.[1,3,4,6]

While the template-prepared electrodes have exceptional rate capabilities, the volumetric energy densities of these electrodes are low. This is because the porosity of the template membranes used is low. For example, the porosity of the membranes used to prepare the nanostructured V_2O_5 electrodes described previously[6] was only 1.2%. Low porosity means that the density of the V_2O_5 nanofibrils protruding from the current collector surface is low. We have developed a simple approach for improving the volumetric energy densities of template prepared nanostructured electrodes. This method entails chemically etching the membrane prior to template synthesis to increase the porosity of the membrane. In addition, we have found that volumetric energy density can be further improved by depositing additional V_2O_5 onto the nanostructured V_2O_5 prepared using these etched template membranes. Results of investigations of these new higher volumetric energy density nanostructured V_2O_5 electrodes are presented here.

EXPERIMENTAL

Materials. The template membranes were commercially available polycarbonate filters (Osmonics, Livermore, CA) having either 50 nm or 400 nm diameter pores with thicknesses of 6 and 10 μm, respectively. The V_2O_5 precursor was triisopropoxyvanadium (V) oxide (99.5% Strem Chemical) and the electrolyte was 1 M $LiClO_4$ (99.99% Aldrich) in a 7:3 (v/v) mixture of diethyl

carbonate (99% Aldrich) and ethylene carbonate (battery grade, Ferro Corp.). All materials were used as received.

Membrane Etching. Template synthesis of the nanostructured V_2O_5 electrodes was done using chemically-etched polycarbonate template membranes. Etching was accomplished by immersing the as-received membranes in 6 M NaOH which had been heated to 65 °C. Membranes with 50 nm diameter pores were immersed for 2 minutes, while the 400 nm pore-diameter membranes were immersed for 6 minutes. After the immersion period, the membrane and NaOH solution (≈ 30 mL) were transferred to 1 L of deionized water to quench the etch process. The membrane was then washed with three, 1 liter portions of deionized water, rinsed in running deionized water for 30 seconds, and then dried under vacuum at room temperature for 1 hour on a PTFE sheet. The immersion times of 2 and 6 minutes represent the time limits beyond which the membranes are no longer mechanically stable enough to be used for template synthesis.

Template synthesis method. The template synthesis procedure that was used to prepare electrodes from the etched polycarbonate template membranes was described in our previous work.[6] Briefly, a section of the etched polycarbonate template membrane was placed on a 2 x 3 cm Pt foil current collector in an argon-filled glove box containing less than 10 ppm water and oxygen. The dimensions of the membranes were varied to control the geometric area of the V_2O_5. The liquid V_2O_5 precursor, triisopropoxyvanadium (V) oxide (TIVO), was applied to the top of the membrane using a 2 μL syringe. The

amount of precursor used was 0.6 μL cm^{-2} for the etched 50 nm membranes and 0.80 μL cm^{-2} for the etched 400 nm diameter membranes. The reason for the difference in applied TIVO volume is the larger thickness of the 400 nm pore-diameter membranes.

The precursor/membrane/current collector composite was then put into the antechamber of the glovebox. The precursor was hydrolyzed in the antechamber at water levels between 100 to 200 ppm H_2O for 10 hours. Antechamber water level was controlled by briefly opening the outer door. A humidity sensor located in the antechamber was used to monitor the water level. Because of its rapid hydrolysis rate, "mud cracking" of the TIVO gel will occur if the water level is too high during this initial hydrolysis period. After hydrolysis in the antechamber, the Pt foil outside of the membrane area was cleaned of the gelled precursor with a damp cotton swab. This was necessary because the liquid precursor spreads out from the membrane onto the surrounding Pt foil. The composite was heated in air at 70 °C for 2 hours and then placed in an oxygen plasma (15 W rf power, 2 hours, 250 mTorr net O_2 pressure) to remove the polycarbonate membrane. Next, the nanostructured gel was heated from ambient temperature to 200 °C over a 3 hour period. Then, after 6 hours at 200 °C, the electrode was heated at 400 °C in 40 psi O_2 for 5 hours to dehydrate and condense the precursor to crystalline V_2O_5. Hereafter, nanostructured electrodes prepared from etched membranes with as-received pore diameters of 50 nm and 400 nm will be referred to as "50 nm" and "400 nm" electrodes, respectively.

Adding more V_2O_5 to the nanostructured electrodes. To further improve volumetric energy density, additional TIVO was applied to the surface of the nanostructured V_2O_5 electrodes prepared as described above. The total amount of TIVO applied was 3.0 μL per cm^2 of V_2O_5 area to the 50 nm electrodes and 4.0 μL per cm^2 of V_2O_5 area to the 400 nm electrodes. The reason for the difference in amount of TIVO is the larger cross-sectional thickness of the 400 nm electrode. The additional TIVO was applied in two equal increments. Each increment was applied to the center of the V_2O_5 area on the nanostructured electrode. The liquid quickly wet the crystalline V_2O_5 as indicated by a change in color from yellow-orange (crystalline V_2O_5) to light brown. The precursor-wet electrode was then hydrolyzed in the glove box antechamber as before, cleaned of gelled precursor around the V_2O_5, and then heated at 70 °C for 2 hours. For the second increment of TIVO, the electrode was reinserted in the glovebox and the process repeated. Following the second increment, the electrode was thermally processed at 200 and 400 °C as for the parent electrodes. Hereafter electrodes prepared by adding TIVO to the 50 nm and 400 nm electrodes will be referred to as "50 nm + TIVO" and "400 nm + TIVO" electrodes, respectively.

Preparation of the thin-film control electrodes. Thin-film V_2O_5 electrodes were prepared by adding liquid TIVO to the surface of the Pt current collector in the glove box. The precursor wets the surface of the Pt and forms a thin, liquid film. Two microliters of precursor were added to a 2 x 3 cm piece of Pt foil. The thin-film of TIVO was then hydrolyzed in the antechamber for 12 hours at a water level between 100 and 200 ppm and then thermally processed

in the same way as for the nanostructured electrodes, except that these electrodes were not exposed to the oxygen plasma. To obtain the desired geometric area, the gelled TIVO was removed from selected areas of the Pt foil between the hydrolysis and thermal treatment using a water-wet cotton swab. Film thickness was controlled by adding more TIVO, in 1 μL increments, after heating at 200 °C for 6 hours.

Electrochemistry Electrochemistry was performed using a three electrode cell with lithium-foil counter and reference electrodes in an argon filled glove box with less than 10 ppm water. Discharge experiments at low current were performed using a computer-controlled EG&G 263A potentiostat/galvanostat. For experiments requiring discharge times of less than 5 seconds (high discharge rates) an EG&G PAR 273 was interfaced to a Nicolet 310 digital oscilloscope to capture the voltage and current transients. Anodic charge capacity was determined using either a voltammograph (BioAnalytical Systems, CV-27) equipped with a digital coulometer or the computer controlled 263A. Electrode morphology was examined using a JEOL 6400 scanning electron microscope.

Because of the high discharge currents used (up to 250 mA), it was desired to minimize solution resistance. This was done by close placement of the working and reference electrodes through the use of a Luggin-Haber capillary.[10] The separation distance between the V_2O_5 working electrode and the capillary was between 3 and 5 mm. The working and counter electrode distance was typically 1.5 cm, and the lithium foil counter electrode was a

minimum of 20 cm^2 total surface area. This cell geometry was adopted to prevent, as much as possible, variations in uncompensated cell solution resistance from complicating interpretation of the rate capability data.

RESULTS AND DISCUSSION

Membrane etching. Figure 3.1 shows scanning electron micrographs of as-received polycarbonate filtration membranes with nominal pore diameters of 50 nm (1A) and 400 nm (1C). The nominal pore densities for these membranes (from the manufacturer) was 6 x 10^8 and 1 x 10^8 pores cm^{-2} for the 50 nm and 400 nm pore-diameter membranes, respectively. The calculated porosities were 1.2% (50 nm membranes) and 12.6% (400 nm membranes). These membranes were selected for this work because they represent the maximum pore density (50 nm membranes) and porosity (400 nm membranes) of the polycarbonate membranes that are available.

The pores in these membranes are produced using the track/etch process.[11] This process entails passing high energy nuclear fission fragments through a nonporous polycarbonate sheet to create damage tracks within the polymer. The polymer is then chemically etched along these damage tracks creating the cylindrical pores. As explained in the Experimental section, NaOH was used here to continue the etching process and increase pore diameter and membrane porosity. Figures 3.1B and 3.1D show the 50 nm and 400 nm membranes, respectively, after etching in 6M NaOH. Using these images, the pore diameter at the membrane surface was determined to be 250 nm ± 50 nm

for the etched 50 nm membranes and 610 nm ± 180 nm for the etched 400 nm membranes.

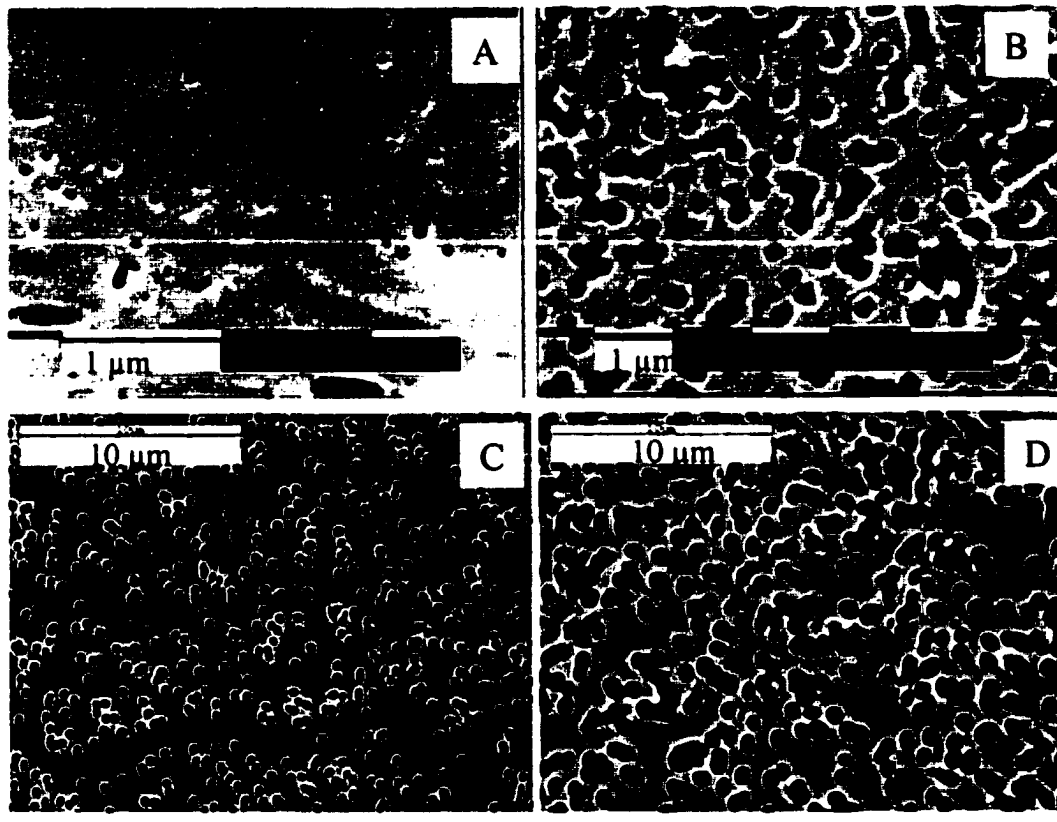

Figure 3.1. Scanning electron micrographs of as-received 50 nm (A) and 400 nm (C) pore diameter polycarbonate template membranes. Micrographs B and D show the 50 nm and 400 nm membranes, respectively, after etching in 6M NaOH.

Electrode Morphology. The scanning electron micrographs (SEMs) in Figure 3.2 show normal and cross-sectional views of the 50 nm (3.2A and 3.2B) and 400 nm (3.2C and 3.2D) electrodes. Figure 3.2 shows that both electrodes consist of V_2O_5 fibrils which protrude from the Pt foil current collector. The diameter of the fibrils was determined to be 250 nm ± 110 nm (50 nm electrode) and 700 nm ± 150 nm (400 nm electrode). These fibril diameters are, within the

standard deviation, identical to the pore diameters of the etched templates as described above. The cross-sectional images (Fig 3.1B and 3.1D) show that the

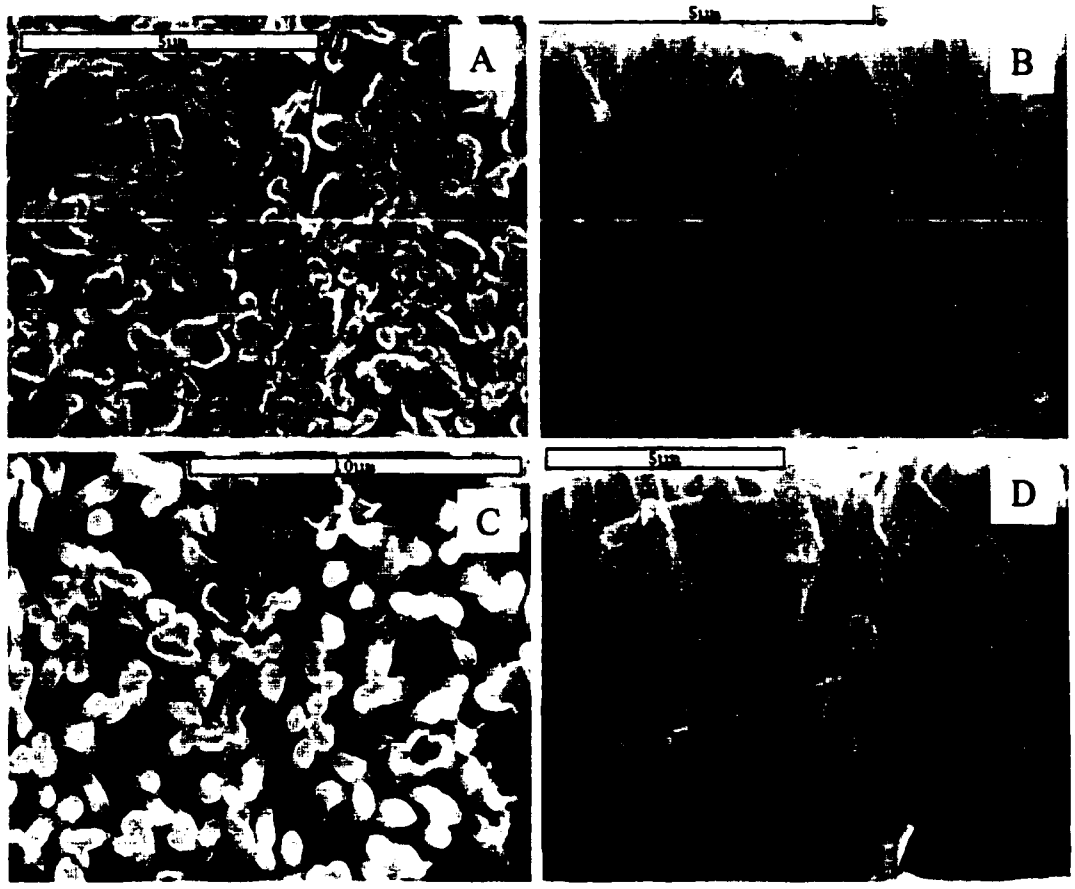

Figure 3.2. Scanning electron micrographs of template-synthesized electrodes prepared from etched 50 nm (A and B) and 400 nm (C and D) polycarbonate template membranes. A and C show the tops of the V_2O_5 fibrils (normal view) while B and D show the cross sections of these electrodes.

50 nm and 400 nm electrodes are 5 and 8 μm thick, respectively. These values are close to the reported thicknesses of the unetched template membranes.

Figure 3.3 shows SEMs of the 50 nm + TIVO (Fig. 3.3A-B) and 400 nm + TIVO (Fig. 3.3C-D) electrodes. Images of the electrode surfaces (Figs 3.3A and 3.3C) show that the fibrils are encased in a surrounding matrix of V_2O_5 due to the

addition of the V_2O_5 precursor to the parent electrodes. The cross-sectional images (3.3B and 3.3D) show that the thicknesses are the same as for the parent

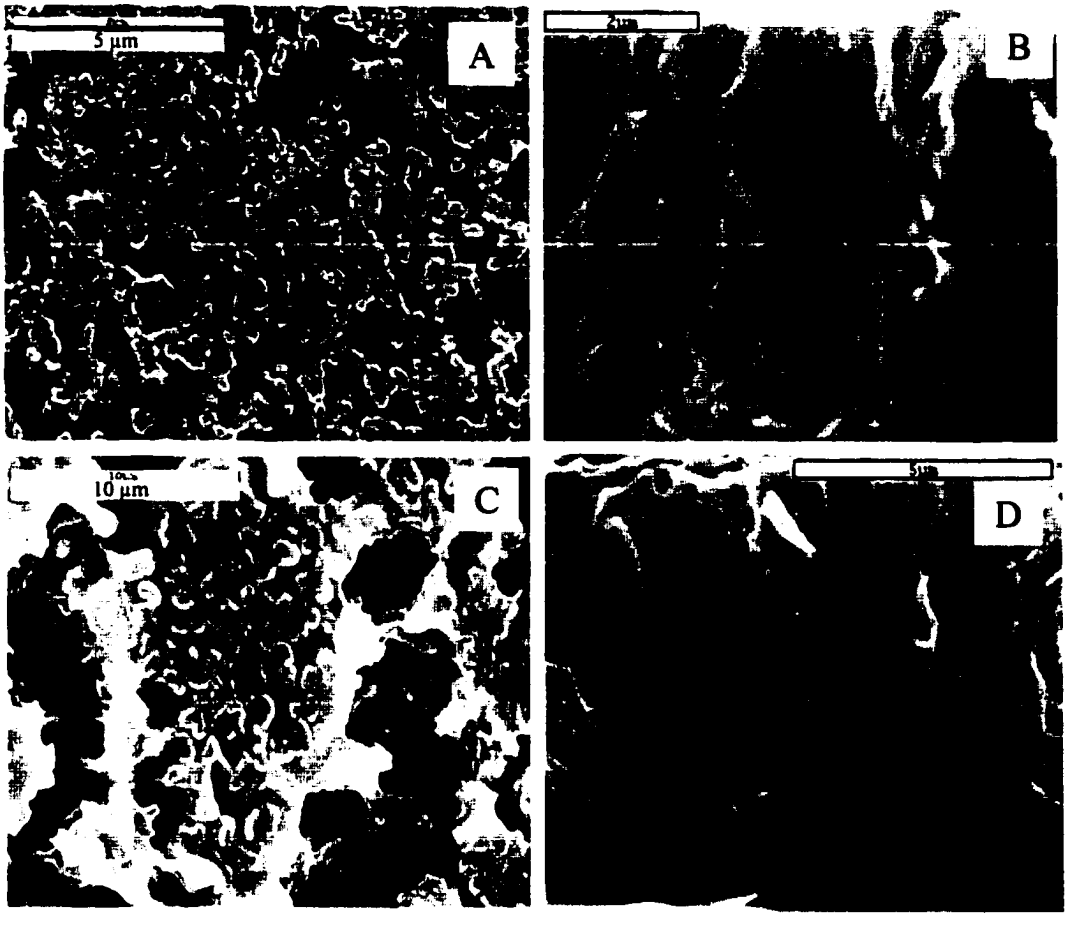

Figure 3.3. Scanning electron micrographs showing the 50 nm + TIVO (A-B) and 400 nm + TIVO (C-D) electrodes prepared by adding the V_2O_5 precursor to the parent nanofibrous electrodes. A and C show the tops of the electrodes where the V_2O_5 fibrils are surrounded with V_2O_5. B and D show the cross sections of the electrodes.

electrodes and also that the morphologies of these two electrodes differ significantly from each other. Figure 3.3B shows that the 50 nm + TIVO electrode contains a fibrillar structure similar to that for the 50 nm and 400 nm parent electrodes. Figure 3.3D shows that the cross section of the 400 nm + TIVO electrode has a much lower surface-area morphology than for the other

electrodes. This electrode consists of smooth "vanes" of V_2O_5 emanating from the V_2O_5 which surrounds the original template-prepared nanofibrils. Further, the V_2O_5 surrounding the nanofibrils appears to be porous as shown by the holes on the left side of Figure 3.3D. The difference in morphology between the 400 nm + TIVO and the other electrodes is important because the 400 nm + TIVO electrode appears to have a lower V_2O_5 surface area, and this should affect the rate capability of the electrode. This will be discussed in the section on Rate Capability.

Figure 3.4 shows an SEM of the thin-film control electrode. This electrode is a continuous film of crystalline V_2O_5 of uniform thickness. SEM crossectional images were obtained at 10 different areas of the thin film to determine the average film thickness. This was done after the electrochemistry experiments by bending the Pt current collector in order to fracture the thin film and expose the cross section. Results show that the average thickness of the film was 2.40 ± 0.22 μm.

The electrodes studied here have very different morphologies and surface areas. In order to compare their rate capabilities, all of the electrodes studied had approximately the same capacity. For the template synthesized electrodes, this was accomplished by controlling the area of the template membrane used. For the thin-film electrode, geometric area was controlled by trimming the gelled TIVO with a cotton swab after removal from the antechamber (see Experimental section).

Electrode Capacities. Figure 3.5 shows the low rate (ca. C/20)

discharge curves of the 50 nm and thin-film electrodes to a voltage cutoff of 2.5 V vs. the lithium reference electrode.

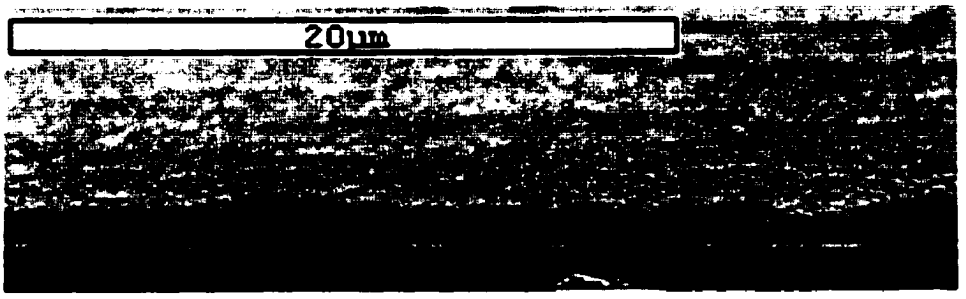

Figure 3.4. Scanning electron micrograph of the thin-film control electrode. The film thickness is approximately 2.4 μm.

The discharge and charge reactions for V_2O_5 can be written as follows

$$xLi^+ + xe^- + V_2O_5 \underset{\text{charge}}{\overset{\text{discharge}}{\rightleftharpoons}} Li_xV_2O_5$$

It is well known that when the voltage cutoff is 2.5 V vs. a Li reference electrode, the maximum capacity of orthorhombic α-V_2O_5 is x = 1 (147 mAh g^{-1}).[12] We previously showed that this maximum capacity can be obtained for nanostructured and thin-film electrodes of α-V_2O_5 by discharging at rates between C/19 and C/23.[6] Thus, the capacities of the electrodes used for this work were determined using a similar procedure, e.g. discharge rates between C/20 and C/24 and a voltage cutoff of 2.5 V (Figure 3.5). The presence of the plateaus at 3.4 and 3.2 V indicates that the unlithiated electrode material is crystalline α-V_2O_5.[13] In addition, we[6] and others[14] have reported that heating

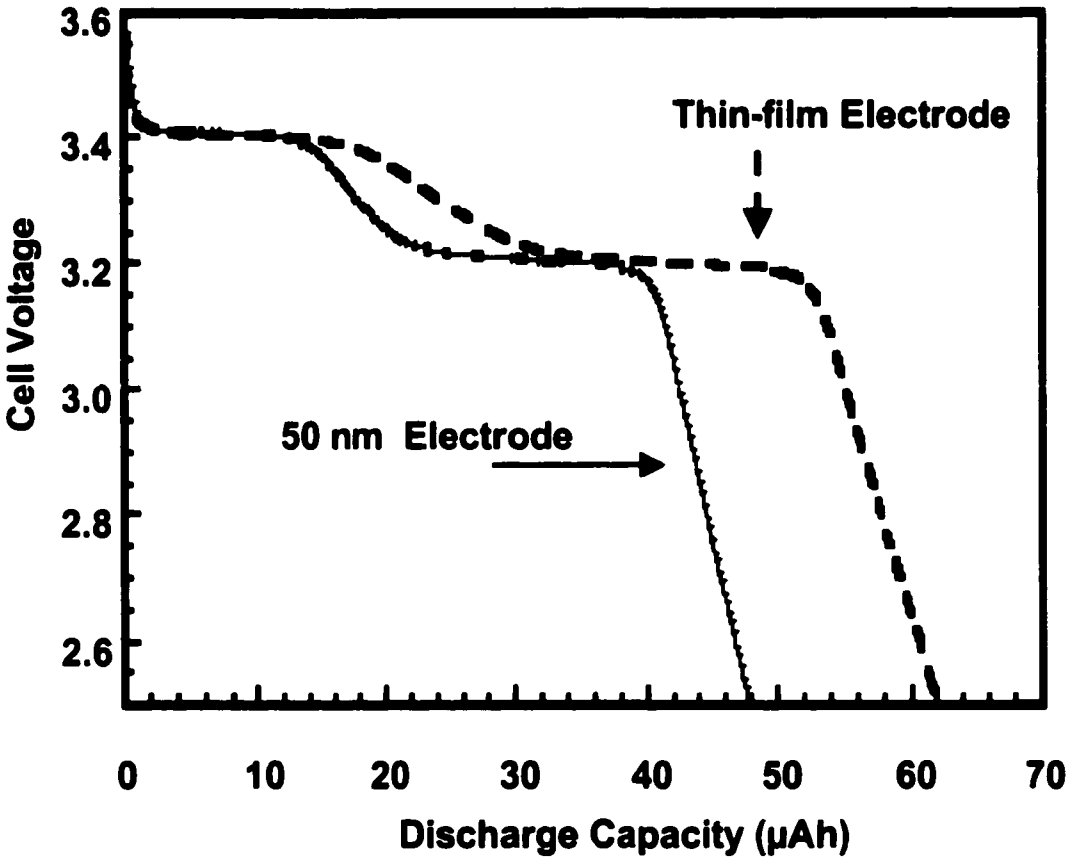

Figure 3.5. Constant current (ca. C/20) discharge curves for the 50 nm and thin-film electrodes showing capacities at a voltage cutoff of 2.5 V vs. Li. Such low rate discharge experiments were used to determine theoretical electrode capacity.

TIVO in oxygen to 400 °C results in the formation of orthorhombic α-V_2O_5.

The volumetric electrode capacities shown in Table 3.1 were calculated using data in columns 1 through 3. Shown in parentheses is the capacity of each electrode relative to the thin-film control. The 50 nm and 400 nm electrodes have a similar volumetric capacity. The data also show that the volumetric capacities of the 50 nm + TIVO and 400 nm + TIVO electrodes are almost twice as high as the parent nanostructured electrodes. This demonstrates the main premise of

this paper that volumetric capacity can be improved by adding V_2O_5 to the to the nanostructured electrodes.

Table 3.1. Electrode Capacities

Electrode Description	Measured Capacity (μAh)	V_2O_5 Geometric Area (cm^2)	Electrode Thickness (μm)	Volumetric Capacity (μAh $cm^{-2}μm^{-1}$)	Geometric Capacity (μAh cm^{-2})
50	48	1.00	5	9.6 (22%)	48
50 + TIVO	57	0.70	5	18 (42%)	82
400	51	0.59	8	11 (26%)	86
400 + TIVO	51	0.32	8	20 (47%)	159
Thin Film	62	0.60	2.4	43 (100%)	103

Column 6 (Table 3.1) shows the geometric capacities of the electrodes used in this study. This data shows the range of electrode capacities that result from the differences in membrane thickness (50 nm vs. 400 nm electrodes) and the addition of more V_2O_5 to the parent electrodes. These data show that the geometric capacities of the template-synthesized electrodes are competitive with that for the thin film. This has implications where the overall thickness of the electrode is not critical so that the nanostructure might be substituted for the thin film.

A common method for showing electrode discharge current is C rate, which is expressed as I = n x C, where I is the discharge current in A, C is the

rated capacity in Ah and n is the multiple of the C rate (essentially the number of discharges in one hour).[15] For this work, "n" values (e.g. C rates) were calculated using the measured (rated) capacities shown in Table 3.1 and the various discharge currents used in the rate capability experiments. For example, a discharge current of 10 mA for the 50 nm electrode was calculated to be a discharge rate of 208C ($0.01A/48x10^{-6}$ Ah).

Rate Capability. Rate capability was determined by measuring electrode discharge capacity at increasing discharge rate (Fig. 3.6). As shown in Figure 3.6, the electrode capacities in these rate capability experiments were determined at a voltage cutoff of 2.6 volts vs. Li. This more positive cutoff voltage was used to avoid the possibility of over discharging the V_2O_5. Over discharge is a problem because at high discharge rates, stopping the discharge at 2.5 V was difficult due to the short time scales of the experiments (for some experiments less than 2 seconds). Discharging the electrodes to potentials less than 2.5 V would cause a change in V_2O_5 crystal structure and result in capacity fading[16] during the 10 to 15 discharge/charge cycles required to determine electrode rate capability.

After each discharge experiment (Fig. 3.6), the electrode was charged at 100 μA from the open circuit potential to 3.80 V and then equilibrated at this voltage with the voltammograph until the current decayed to the first scan value. In all cases the charge and discharge capacities were equivalent showing that the discharge capacity was 100% faradaic. Complete characterization of the rate capability of each electrode required up to 15 discharge / charge cycles. Here

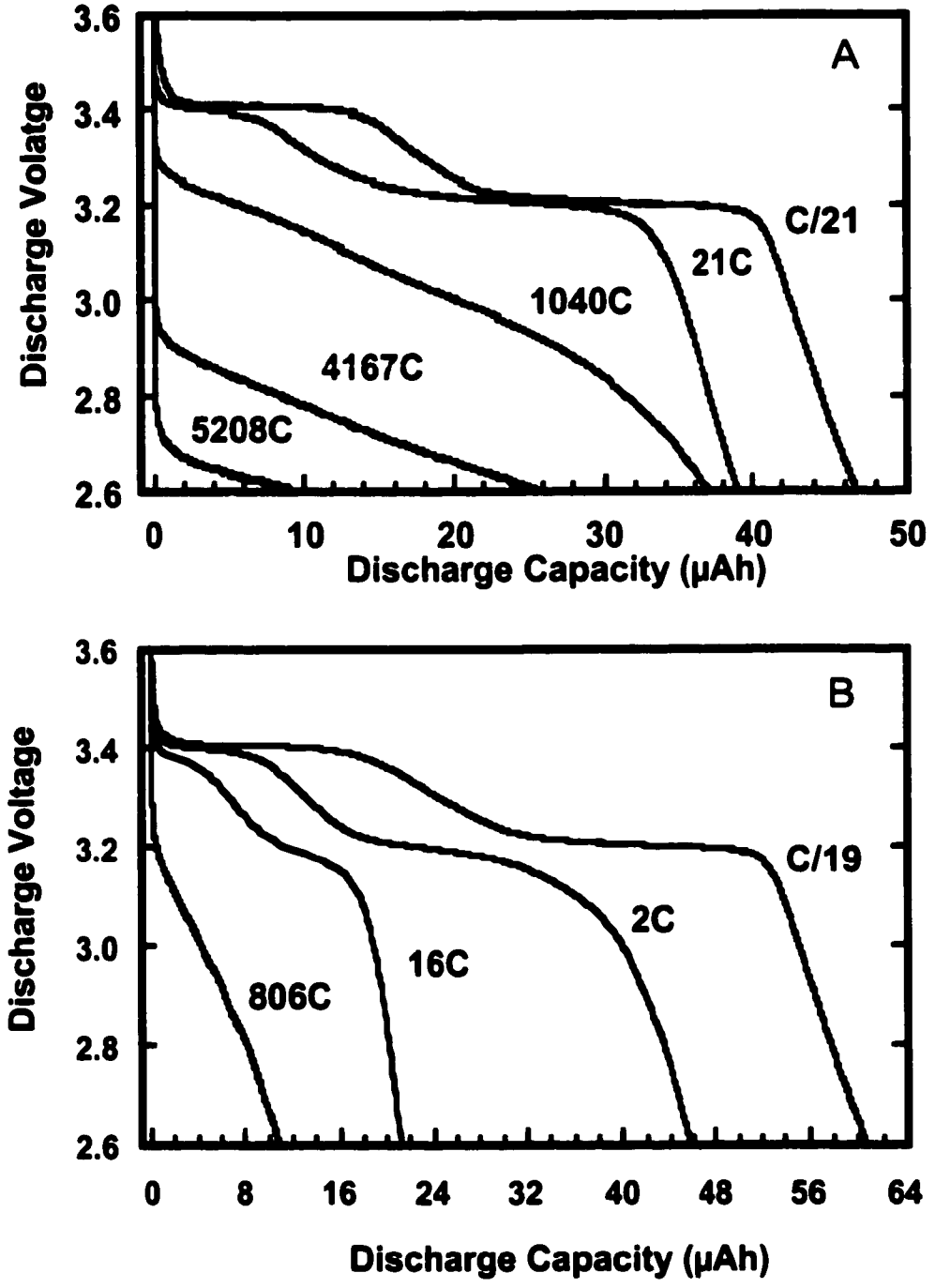

Figure 3.6. Cell voltage vs. capacity for 50 nm (A) and thin-film (B) electrodes at various discharge rates.

also, we were concerned that the capacity of the electrodes could fade with increasing cycle number and complicate the interpretation of the rate capability

data.[17] It was determined that the capacities of the first and last discharge experiments, performed at low discharge rate, were the same within experimental error.

Figure 3.6 shows electrode capacity vs. discharge rate for the 50 nm (Fig. 3.6A) and thin-film control (Fig. 3.6B) electrodes. The curves in Figure 3.6 show that, in general, the capacities of the 50 nm and thin-film electrodes decrease with increasing discharge rate. However, the capacity of the nanostructured electrode remains higher, at high discharge currents, than for the thin-film control electrode. Figure 3.7 shows plots of discharge capacity vs. discharge rate for all of the electrodes studied here. (The experimental data are shown as the points and the lines are drawn just to aid the eye.) At the lowest discharge rates all of the electrodes reach the maximum theoretical capacity for a cutoff voltage of 2.6V. The currents (and C rates) used in these lowest-discharge-rate experiments were 2.4μA (C/20), 2.4 (C/24), 2.3 (C/22), 2.3 (C/22) and 2.8 μA (C/22) for the 50 nm, 50 nm + TIVO, 400 nm, 400 nm + TIVO and thin-film control electrodes respectively. The discharge capacities at these rates were between $x = 0.96$ and 0.98 (141 to 144 mAh g^{-1}).

Figure 3.7 shows that, at high discharge rates (> 10C), the Li^+ storage capacity of the template-synthesized electrodes is higher than for the thin-film control electrode. As discussed in our previous reports[1,3,4,6], this is because of the shorter Li^+ diffusion distances and higher surface areas for the template-synthesized electrodes compared to the thin-film electrode. Shorter diffusion distances decrease the time necessary for Li^+ diffusion through the electrode

material. In addition, shorter diffusion distances result in higher electrode material surface areas and, therefore, in lower Li^+ insertion-rate (current)

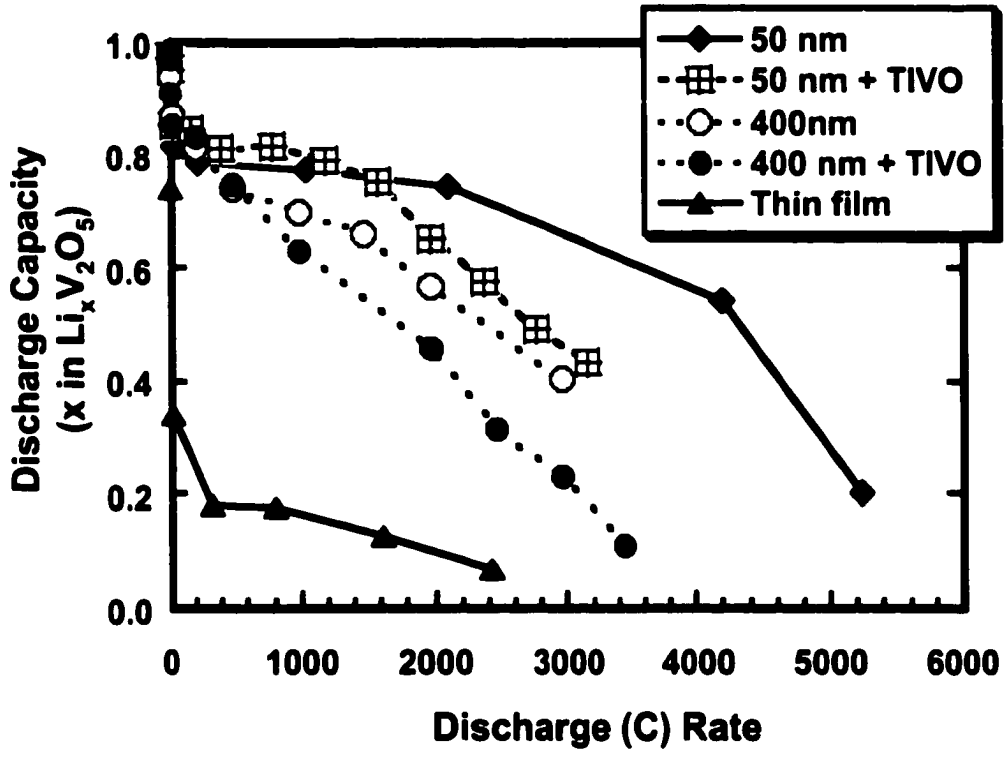

Figure 3.7. Comparison of Li^+ ion storage capacity vs. discharge rate for the template-synthesized and thin-film electrodes.

densities. Both of these effects delay concentration polarization to higher discharge currents, resulting in higher electrode capacities.

Figure 3.7 shows that the electrode utilization of the 50 nm electrode is higher, at high discharge currents, than for the other electrodes. Electron microscopy (Fig. 3.2) shows that this electrode contains the smallest diameter fibrils and therefore the shortest Li^+ diffusion distances. The 50 nm + TIVO and

400 nm electrodes also show very good rate capabilities. The cross-sectional SEM images (Figs 3.3B and 3.2D) show a fibrillar, high surface area morphology for these electrodes which explains their good rate capabilities. The 400 nm + TIVO electrode has the poorest rate capability of the template-synthesized electrodes (but still much better than the control electrode). SEM images (Fig. 3.3C-D) suggest that the Li^+ diffusion distances are higher, and the V_2O_5 surface area lower, than for the other template-synthesized electrodes. This results in lower electrode utilization at high discharge rates.

Volumetric rate capability is important where electrode volume is a critical issue and high discharge rates are needed. Table 3.1 shows that, at low discharge rates (ca. C/20), the volumetric discharge capacity of the thin-film electrode is higher than for the template synthesized electrodes. Figure 3.8A compares the volumetric capacity at various discharge rates for the 50 nm, 50 nm + TIVO, and the control electrodes; analogous data for the 400 nm and 400 nm + TIVO electrodes are shown in Figure 3.8B. The volumetric capacity of the thin-film control electrode decreases rapidly to 35% of the theoretical value at 160 C and 18% (7.5 μAh cm-2 μm-1) at 240 C. While the 50 nm electrode has the lowest theoretical volumetric capacity (Table 3.1), because of it's high surface area and short diffusion distances this electrode loses little capacity even at high discharge rates. The theoretical volumetric capacity of the 50 nm + TIVO is nearly twice that of the parent 50 nm electrode (Table 3.1). Combined with its high rate capability (Fig. 3.7), this higher volumetric capacity results in over twice

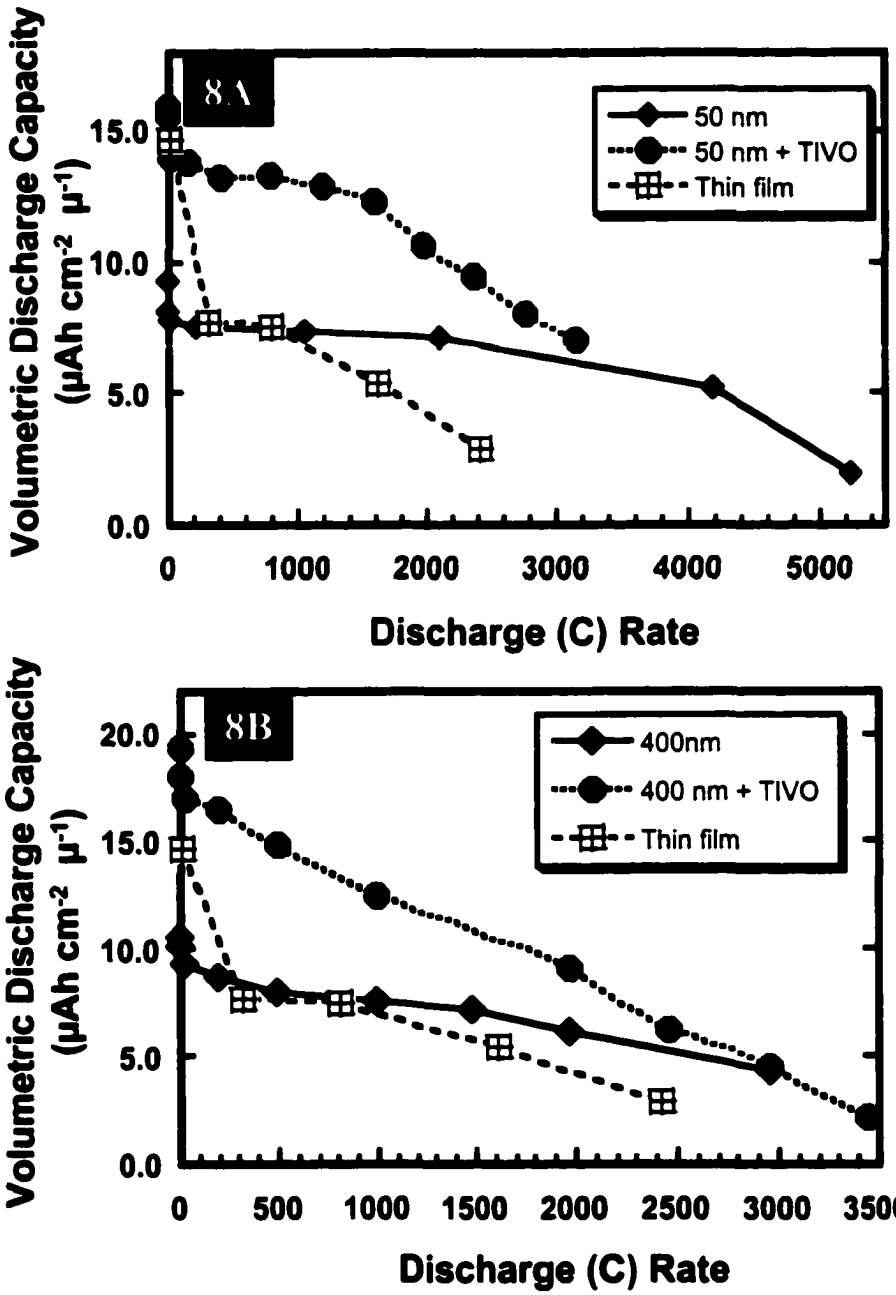

Figure 3.8. Volumetric capacity vs. discharge rate for the 50 nm, 50 nm + TIVO and thin-film electrodes (A) and for the 400 nm, 400 nm + TIVO and thin-film electrodes (B).

the volumetric rate capability of the thin-film electrode at discharge rates greater than 200C.

The results for the 400 nm and 400 nm + TIVO electrodes show a similar trend (Fig. 3.8B). The theoretical volumetric capacity of the 400 nm electrode is 26% of the thin-film control electrode value. However, its high rate capability results in a volumetric capacity equivalent to the thin-film capacity at high discharge rates (Fig. 3.8B). The 400 nm + TIVO electrode posses the highest volumetric capacity of the template-synthesized electrodes and better rate capability than the thin-film (Fig. 3.7). The result is 2 times higher volumetric capacity at discharge rates > 200C. These results on volumetric rate capability show, again, the value of higher surface area and shorter diffusion distances with respect to electrode rate capability. In addition, they show the volumetric rate capability advantage obtained by adding TIVO to the 50 nm and 400 nm electrodes.

The geometric rate capabilities of the electrodes are shown in Figure 3.9. Because of the higher cross-sectional thicknesses, the template-synthesized electrodes have measured geometric capacities as much as 50 % higher than the thin-film control electrode (Table 3.1). Due to the better rate capabilities demonstrated in Figure 3.7, the template-synthesized electrodes can deliver up to 5 times more capacity per square centimeter of V_2O_5 area than the thin-film control electrode at discharge rates > 1C (Figs. 3.9 A-B).

While the geometric capacity of the thin film, at low discharge rate, could be improved by making it thicker, this would make the rate capability of this electrode even worse. Indeed, at high discharge rate, capacity is limited by the

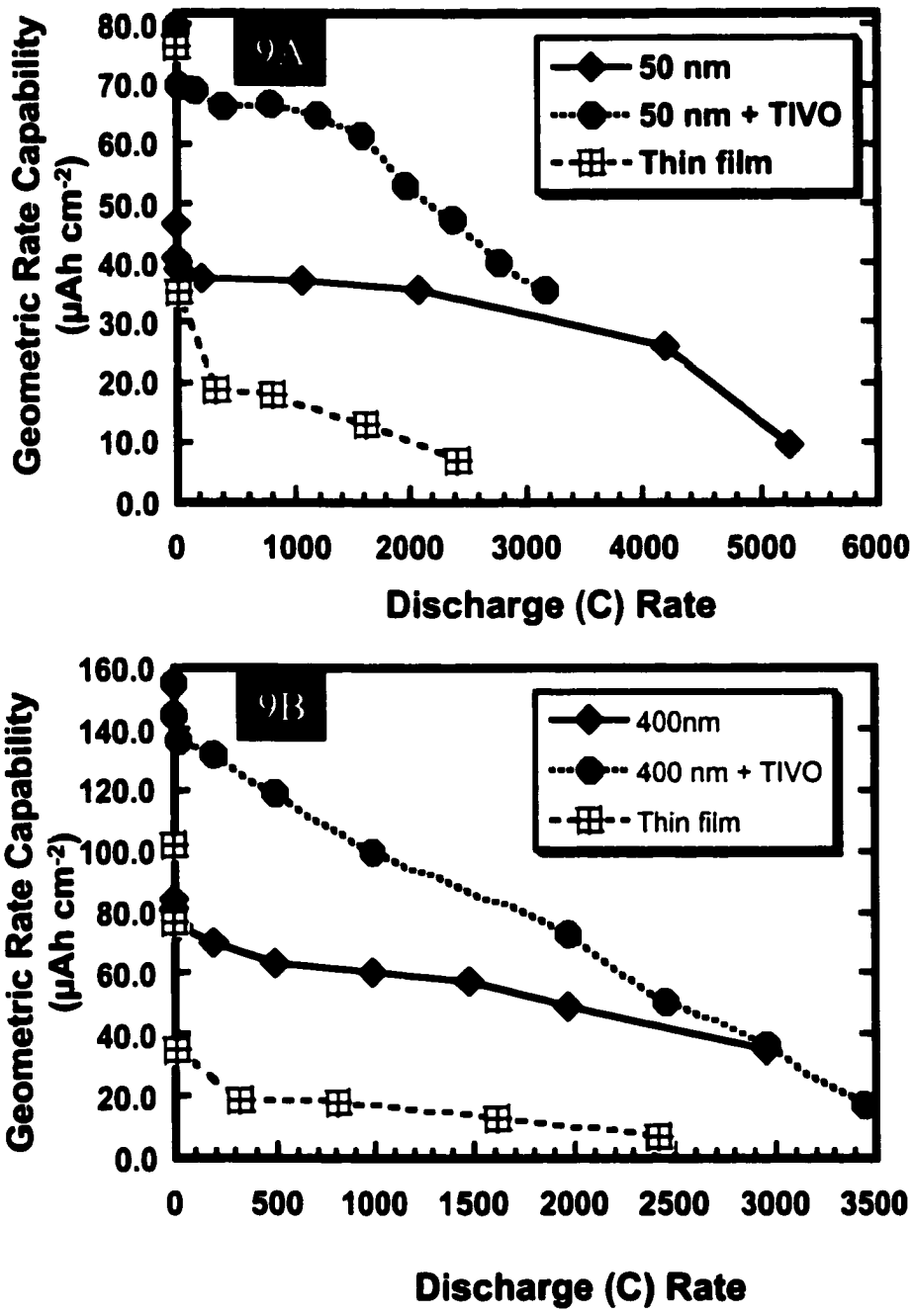

Figure 3.9. Geometric capacity vs. discharge rate for the 50 nm, 50 nm + TIVO and thin-film electrodes (A) and for the 400 nm, 400 nm + TIVO and thin-film electrodes (B).

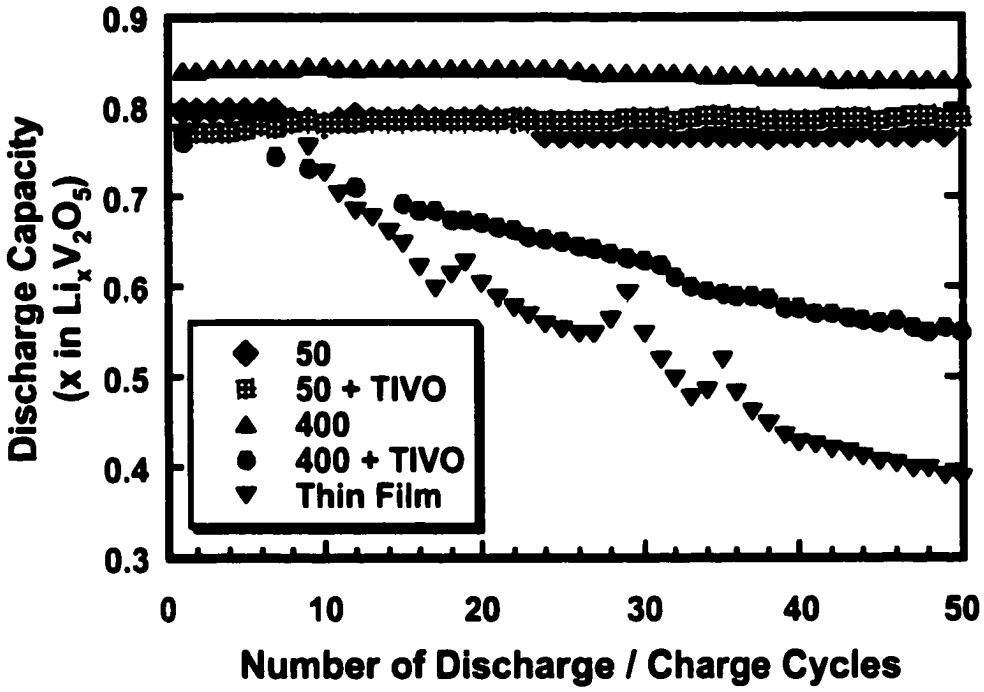

Figure 3.10. Electrode discharge capacity as a function of cycle number.

distance Li^+ diffuses within the film, and not by film thickness. Hence, at high rates, making the film thicker would not improve geometric capacity.

Figure 3.10 shows electrode discharge capacity for 50 discharge/charge cycles. The depth of discharge was approximately the same for all the electrodes (x values were between 0.76 and 0.84). Each cycle consisted of a constant current discharge to a voltage cutoff of 2.60 V vs. Li. This was followed by a low current charge (100 μA) to 3.80 V and then equilibration at 3.80 V. The current was allowed to decay to first scan conditions before the next cycle was initiated. The data in Figure 3.10 show that the 50 nm, 50 nm + TIVO and 400 nm electrodes maintained better than 95% of their original discharge capacities after 50

discharge/charge cycles. These data are contrasted with the cycling performance of the 400 nm + TIVO and thin-film electrodes, which show capacity losses of 28% and 49% respectively after 50 cycles. The reason for the capacity fade of the thin film was loss of the electrode mass which was detected visually as the V_2O_5 film exfoliated from the current collector during cycling. The 400 nm + TIVO electrode showed a similar loss in electrode material which was manifested by small pinholes in the electrode material and were detected with an optical microscope after cycling.

One mechanism that has been proposed to account for capacity fading in Li-insertion electrodes is expansion of the atomic lattice that occurs during Li insertion.[17,18] The result of expansion is loss of contact between the insertion material particles and irreversible capacity loss. The V_2O_5 atomic lattice undergoes expansion in the *c* direction during Li insertion and this could explain the exfoliation and poor cycling performance of the thin-film and 400 nm + TIVO electrodes. In contrast, Besenhard and coworkers[18] have shown that a nanostructured Li-insertion electrode has improved cycling performance versus a more densely-packed electrode with larger particles. The reason given was that the nanoparticles are loosely spaced and these spaces can accommodate particle expansion during Li insertion. It is possible, with the nanostructured electrodes shown here, that solvent evaporation during hydrolysis results in void spaces within the V_2O_5 fibrils and better cycling performance for the nanofibrous electrodes

CONCLUSIONS

We have demonstrated a sol-gel based template-synthesis procedure for the preparation of crystalline V_2O_5 electrodes. These electrodes show high volumetric and geometric rate capabilities compared to a thin-film control electrode. The template-synthesized electrodes have approximately 25 and 45 % of the volumetric capacity of a thin film electrode at low discharge rates (C/20). As shown here and in our previous studies,[1,3,4,6] the template-synthesized electrodes have better rate capability than the thin-film electrode because of shorter Li^+ diffusion distances and higher V_2O_5 surface areas. As a result, they deliver up to 2 times higher volumetric capacity at discharge rates greater than 200C and up to 5 times higher geometric capacities at rates greater than 1C compared to the thin-film control electrode. We also demonstrated two approaches for improving volumetric capacity for template-prepared nanostructured electrodes. The first entails etching the membrane to increase porosity. The second entails adding additional V_2O_5 to a template-prepared nanostructured electrode to increase the amount of electrode material.

REFERENCES FOR CHAPTER 3

1)Che, G.; Jirage, K. B.; Fisher, E. R.; Martin, C. R. *J. Electrochem. Soc.* **1997**, *144*, 4296-4302.

2)Goodenough, J. B. *General Concepts*; Goodenough, J. B., Ed.; Wiley-VCH: New York, 1998, pp 1-25.

3)Li, N.; Patrissi, C. J.; Che, G.; Martin, C. R. *J. Electrochem. Soc.* **2000**, *147*, In Press.

4)Nishizawa, M.; Mukai, K.; Kuwabata, S.; Martin, C. R.; Yoneyama, H. *J. Electrochem. Soc.* **1997**, *6*, 1923-1927.

5)Passerini, S.; Ressler, J. J.; Le, D. B.; Owens, B. B.; Smyrl, W. H. *Electrochim. Acta.* **1999**, *44*, 2209-2217.

6)Patrissi, C. J.; Martin, C. R. *J. Electrochem. Soc.* **1999**, *146*, 3176-3180.

7)Tran, T. D.; Feikert, J. H.; Pekala, R. W.; Kinoshita, K. *J. Appl. Electrochem.* **1996**, *26*, 1161-1167.

8)Hulteen, J. C.; Martin, C. R. *J. Mater. Chem.* **1997**, *7*, 1075-1087.

9)Martin, C. R. *Science* **1994**, *266*, 1961-1966.

10)Bard, A. J.; Faulkner, L. R. *Electrochemical Methods*; Bard, A. J.; Faulkner, L. R., Ed.; John Wiley & Sons: New York, 1980, pp 128-130.

11)Fleischer, R. L.; Price, P. B.; Walker, R. M. *Nulcear Tracks in Solids*; University of California Press: Berkely, 1975.

12)Dickens, P. G.; French, S. J.; Hight, A. T.; Pye, M. F. *Mat. Res. Bull* **1979**, *14*, 1295-1299.

13)McKinnon, W. R.; Haering, R. R. *Physical Mechanisms of Intercalation* In Modern Aspects of Electrochemistry; Ralph White, E; Bockris, J. O'M.; Conway, B. E. Eds.; Plenum Press: New York, 1983; Vol. 15, pp 235-304.

14)Davies, A.; Hobson, R. J.; Hudson, M. J.; Macklin, W. J.; Neat, R. J. *J. Mater. Chem.* **1996**, *6*, 49-56.

15)Linden, D. *Basic Concepts* in Handbook of Batteries; Linden, D., Ed.; McGraw-Hill: New York, **1995**, pp 1.3-1.11.

16)Braithwaite, J. S.; Catlow, C. R. A.; Gale, J. D.; Harding, J. H. *Chem. Mater.* **1999**, *11*, 1990-1998.

17)Arora, P.; White, R. E.; Doyle, M. *J. Electrochem. Soc.* **1998**, *145*, 3647-3667.

18)Besenhard, J. O.; Yang, J.; Winter, M. *J. Power Sources* **1997**, *68*, 87-90.

CHAPTER 4

CHANGES IN THE SHAPE AND OPTICAL PROPERTIES OF GOLD NANOPARTICLES CONTAINED WITHIN ALUMINA MEMBRANES DUE TO LOW-TEMPERATURE ANNEALING

Introduction We[1-6] and others[7-9] have been studying the properties of nanoscopic metal particles deposited within the pores of porous alumina template membranes. Special interest has been devoted to the optical properties of Au nanoparticle/alumina membrane composites.[1,3-6] The important feature of this template approach for preparing Au nanoparticles is that both the diameter and aspect ratio (length/diameter) of the particle can be varied at will. In previous work, we demonstrated that when the diameter of the Au nanoparticle was decreased, there was a blue shift in the wavelength of maximum absorption intensity of the plasmon resonance band, λ_{max}, of the Au nanoparticle/alumina composite. Also, when the aspect ratio of the nanoparticle was decreased, a red shift in the λ_{max} was observed. These effects have been modeled using Maxwell-Garnett (MG) effective medium theory.[3,5] More recently, we have developed a *dynamic* Maxwell-Garnett (DMG) effective medium theory for the prediction of optical properties of nanometallalumina membrane composites.[1,6] This dynamic

modification of the conventional MG theory allows for more accurate modeling of the nanoparticle plasmon resonance band when the diameter of the nanoparticle is not infinitely small (i.e., when the nanoparticle diameter is approximately between 20 and 100 nm).

While investigating the thermal stability of these composite membranes, it was discovered that heating the Au nanoparticle/alumina composite to temperatures well below the Au melting point sometimes resulted in dramatic changes in the optical properties (i.e., color) of the membranes. There has been a large number of studies investigating the effects of annealing on the structural and optical characteristics of nanosized metals,[10-14] semiconductors,[15] and inert gas crystallites[16] at temperatures significantly below their bulk melting point. Most of the prior work on the metal nanostructures has been carried out on island films.[10-12,14] Studies of these metal island films have shown diffusion and coalescence of the metal nanoparticles resulting in changes in nanoparticle shape, size, and optical properties. Such changes can occur at extremely low temperatures ranging from 400 °C down to room temperature. However, it is very difficult, if not impossible, to follow changes in the plasmon resonance band solely as a function of particle shape for island films because the initial nanoparticles formed at room temperature coalesce into significantly larger nanoparticles after heat treatment.

This work shows, low-temperature-induced Au nanoparticle size and shape changes and the effect of these changes on the optical properties without interference from nanoparticle coalescence. This is possible with the template-

synthesized Au nanoparticle composite membranes because each Au nanoparticle is confined to its own pore. The temperature-induced changes in size and shape were determined using transmission electron microscopy. The corresponding change in optical properties were investigated using UV/Visible absorption spectroscopy.

EXPERIMENTAL

Preparation of Nanoporous Alumina Template Membranes. Nanoporous aluminum oxide template membranes were prepared in-house as described previously.[1,3-6] Briefly, 99.999% purity aluminum was electropolished to a mirror finish in 2:3 (v/v) phosphoric/sulfuric acid solution at 70 °C for 10 min at a current density of 75 mA cm^{-2}. The aluminum was then anodized at a constant potential (30 V) in 15% oxalic acid at a temperature between 0 and 5 °C at a current density between 1 and 2 mA cm^{-2}. This process results in the growth of a porous aluminum oxide film on the surface of the aluminum. Detachment of this alumina film from the aluminum substrate is accomplished via voltage reduction and subsequent immersion of the alumina/aluminum composite in 25% phosphoric acid.[5] The approximately 25 μm thick nanoporous alumina template was then washed thoroughly with ultrapure water (obtained by passing distilled water through a Millipore water purification system) and dried at room temperature in air. These alumina template membranes contained *ca.* 45 nm diameter pores, as determined using transmission electron microscopy.

Gold Nanoparticle Electrodeposition. The Au nanoparticle/alumina composites were fabricated via the electrodeposition of gold within the pores of

the alumina template. This procedure is described in detail elsewhere.[1,5] Briefly, Ag is first thermally evaporated onto one face of the alumina template membrane. This silver layer functions as a cathode for the constant current electrodeposition of silver "nanoposts" which extend several microns into the pores of the template. Gold nanoparticles are subsequently electrodeposited on top of these silver posts using a commercial Au plating solution (Orotemp 24, Technic, Inc.). The silver posts ensure that the gold particles are formed well into the template pores where pore diameter is more uniform. The silver is then dissolved away by immersion in concentrated nitric acid, leaving an Au nanoparticle within each pore of the alumina membrane.

The aspect ratio of the Au nanoparticles is determined by the number of coulombs of charge used during the electrodeposition.[1,6] In this work, Au nanoparticles were prepared by electrodepositing 0.40, 0.20, and 0.08 Coulombs of Au over a geometric template surface area of 3.54 cm^2. An EG&G Princeton Applied Research Model 173 potentiostat equipped with a PAR Model 176 digital coulometer was used for the electrodeposition.

Spectral Characterization. UV/visible absorption spectra were acquired using a Hitachi U-3501 spectrophotometer. The template membranes were oriented perpendicular to the incident beam such that the diameter of the Au nanoparticles was aligned parallel with the electric field vector of the light. To study the effects of temperature on the optical properties of the Au/alumina composites, the membranes were heated to the desired temperature, held at this temperature for 1 h, and then cooled to room temperature. An absorption

spectrum of each Au nanoparticle/alumina composite was measured before and after each heat treatment. The heating temperatures used ranged from 40 to 400 °C.

Transmission Electron Microscopy *(TEM).* The dimensions of the Au nanoparticles were characterized using a JEOL 2000 transmission electron microscope. This was accomplished by dissolving the alumina template and collecting the Au nanoparticles on a carbon-coated copper TEM grid (Ted Pella, Inc.). This procedure involved placing a section of composite on the grid in a 1 mL plastic container. The container was filled with 1 M NaOH. After a 2 h immersion period, the NaOH was removed carefully so as not to disturb the gold particles. The container was then refilled with ultrapure water and drained again. After two additional rinse cycles, the grid was dried in air at room temperature and imaged with the TEM.

RESULTS AND DISCUSSION

All of the Au nanoparticles investigated here were obtained by electrodepositing Au within a nanoporous alumina membrane with 45 nm diameter pores. Au nanoparticles with varying aspect ratios were obtained by electroplating three different amounts of Au within the pores of the template membrane. TEM images of these Au nanoparticles before and after heating the Au/alumina composite to a temperature of 400 °C are shown in Figure 4.1.

Figure 4.1A,B shows images of the Au nanoparticles obtained after passing the largest amount of charge (0.40 C) during the Au electrodeposition.

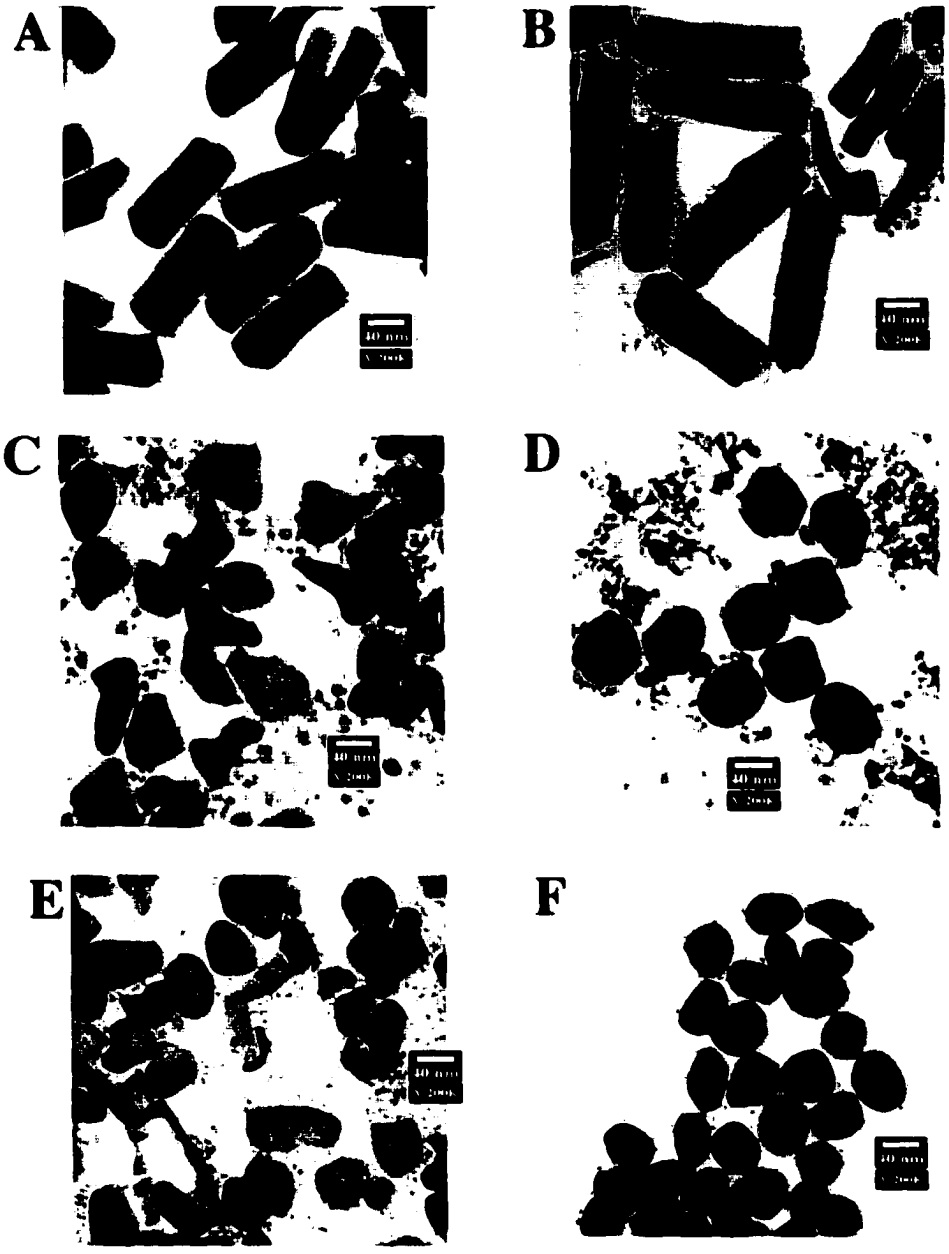

Figure 4.1. Transmission electron micrographs of Au nanoparticles before (A, C, E) and after (B, D, F) heating the membrane containing the particles to 400 °C. Particles having three different aspect ratios are shown. The aspect ratio was varied by varying the number of Coulombs used to electrochemically deposit the Au within the template membrane. The number of Coulombs used was 0.40 C (A, B), 0.20 C (C, D) and 0.08 C (E, F).

As would be expected, these nanoparticles have the highest aspect ratio (*ca.* 3) of any of the nanoparticles investigated in this study. A comparison of the images Figures 4.1A and 1B shows that neither the size nor the shape of these Au nanoparticles changes upon heating to 400 °C. Electron diffraction patterns before and after heating showed no discernible changes, indicating that there are no major changes in crystallinity of these Au nanoparticles.

This lack of temperature-induced change in the size and shape of these aspect ratio = 3 Au nanoparticles is reflected in the optical absorption spectra. Membranes containing these Au nanoparticles were heated at various temperatures up to 400 °C, and the optical absorption spectra were obtained after each heat treatment, Figure 4.2. Note that the position of the plasma resonance band does not change with temperature. This is further illustrated in Figure 4.3 (curve A), which shows a plot of the λ_{max} for the plasmon resonance band versus the temperature at which the membrane was heated. These data clearly show that the λ_{max} is insensitive to applied temperature for the membranes containing these highest aspect ratio particles.

The Au nanoparticles in Figure 4.1 C,D were obtained by depositing 0.20 C of Au within the pores of the alumina membrane. Looking first at the TEM image obtained after heating to 400 °C, Figure 4.1D, these Au nanoparticles have, as expected, a lower aspect ratio than the 0.40 C nanoparticles discussed previously. More interesting, however, there is now a change in the shape of the Au nanoparticles before versus after heating to 400 °C. After heating, the Au nanoparticles have a uniform, almost spherical shape with the expected *ca.* 45

nm diameter. In contrast, before heating, the Au nanoparticles have very irregular shapes and sizes, Figure 4.1C. Some of the particles appear like thin skins, as if

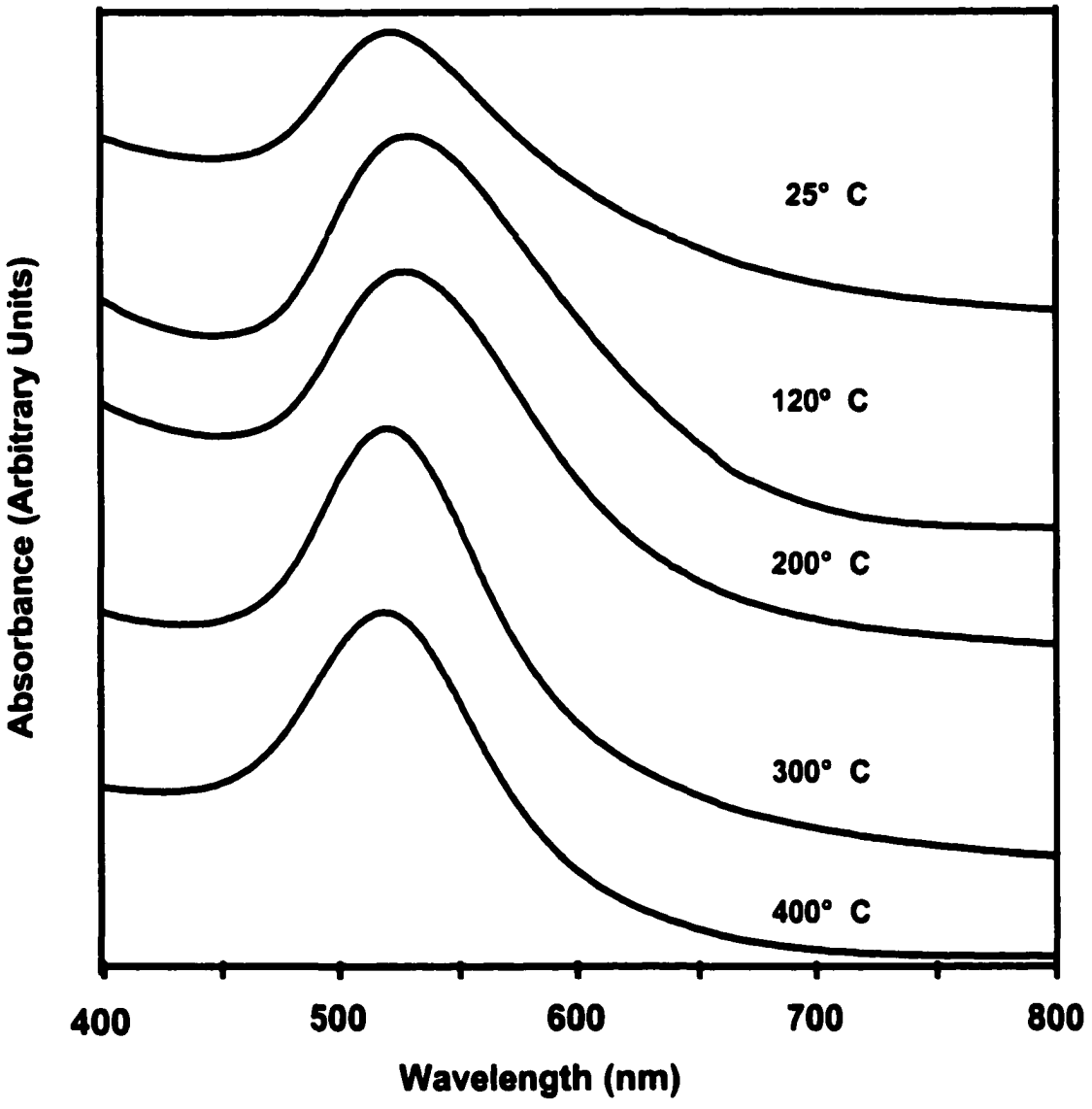

Figure 4.2. Absorption spectra obtained before and after heating the 0.40 C Au nanoparticle/alumina composite. The temperatures used are as indicated.

some of the Au deposited preferentially along the pore wall. This skin-like interpretation is reinforced by the electron transparency of some of the particles in this image. However, after heating, the nanoparticles are electron opaque.

This change in shape of the 0.20 C Au nanoparticles upon heating is reflected in the optical absorption spectra, Figure 4.4. Note that in contrast to the higher aspect ratio particles, there is now a small blue shift in the λ_{max} of the

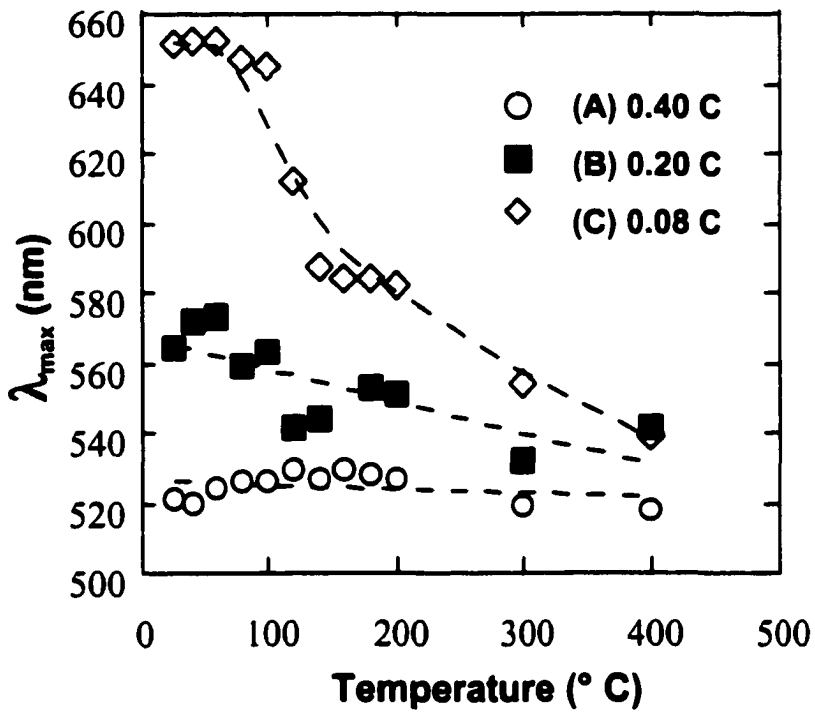

Figure 4.3. Plot of λmax for the plasmon resonance band of the three different Au/alumina composites versus the temperature at which the Au nanoparticle/alumina composite was heated: (A) 0.40 C, (B) 0.20 C, and (C) 0.08 C.

plasmon band with increasing temperature. This is illustrated in Figure 4.3 (curve B), which shows a plot of λ_{max} for the plasmon resonance band versus temperature at which the membrane was heated. This change in λ_{max} is more easily seen with the eye as the membranes go from blue before heating to pink after heating.

In addition to the shift in λ_{max} for the plasmon resonance band, the band also becomes significantly more narrow after heating, Figure 4.4. This narrowing reflects the uniformity in nanoparticle size and shape after thermal treatment, as indicated in the TEM images. The unheated 0.20 C particles begin as an

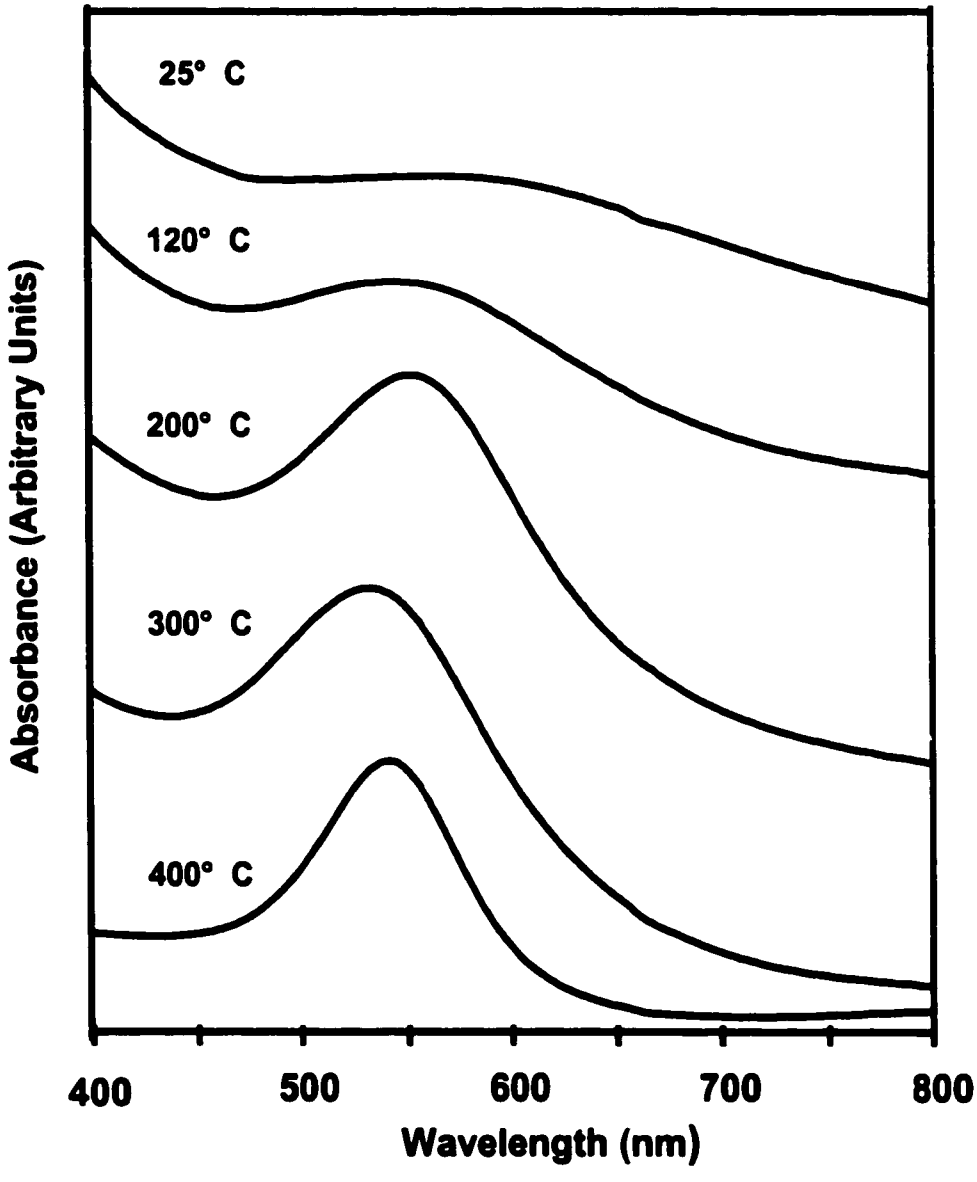

Figure 4.4. Absorption spectra obtained before and after heating the 0.20 C Au nanoparticle/alumina composite. The temperatures used are as indicated.

ensemble of irregular sizes, shapes, and aspect ratios, and as a result, the plasmon absorption is very broad. However, after thermal treatment, the particles adopt a uniform size and shape, and the plasmon band narrows.

Finally, the Au nanoparticles in Figure 4.1E,F were obtained from membranes that were plated with a much lower amount of Au, 0.08 C. Even more evident than with the 0.20 C particles, the unheated form of these 0.08 C particles is irregularly shaped and is apparently quite thin, as indicated by the electron transparency of the particles, Figure 4.1E. After heating, these particles appear to have a uniform, mostly spherical shape with a diameter of *ca.* 35 nm, Figure 4.1F. With less Au electrodeposited within the pores, the final annealed nanoparticles are definitely smaller than the previously discussed particles.

This change in shape of the 0.08 C Au nanoparticles upon heating is reflected in the optical absorption spectra, Figure 4.5. There is now a dramatic blue shift in the position of the plasmon band with increasing temperature. This is clearly illustrated in the plot of λ_{max} versus membrane annealing temperature, Figure 4.3 (curve C). Once again, the plasmon resonance band of the 0.08 C particles becomes significantly more narrow after heating, Figure 4.5. As before, this narrowing reflects the uniformity in nanoparticle size and shape after thermal treatment, as indicated in the TEM images.

As previously mentioned, studies of metal island films have shown diffusion and coalescence of metal nanoparticles resulting in changes in nanoparticle shape, size, and optical properties at low temperatures ranging from 400 °C down to room temperature.[10-12,14] In addition, it has been well

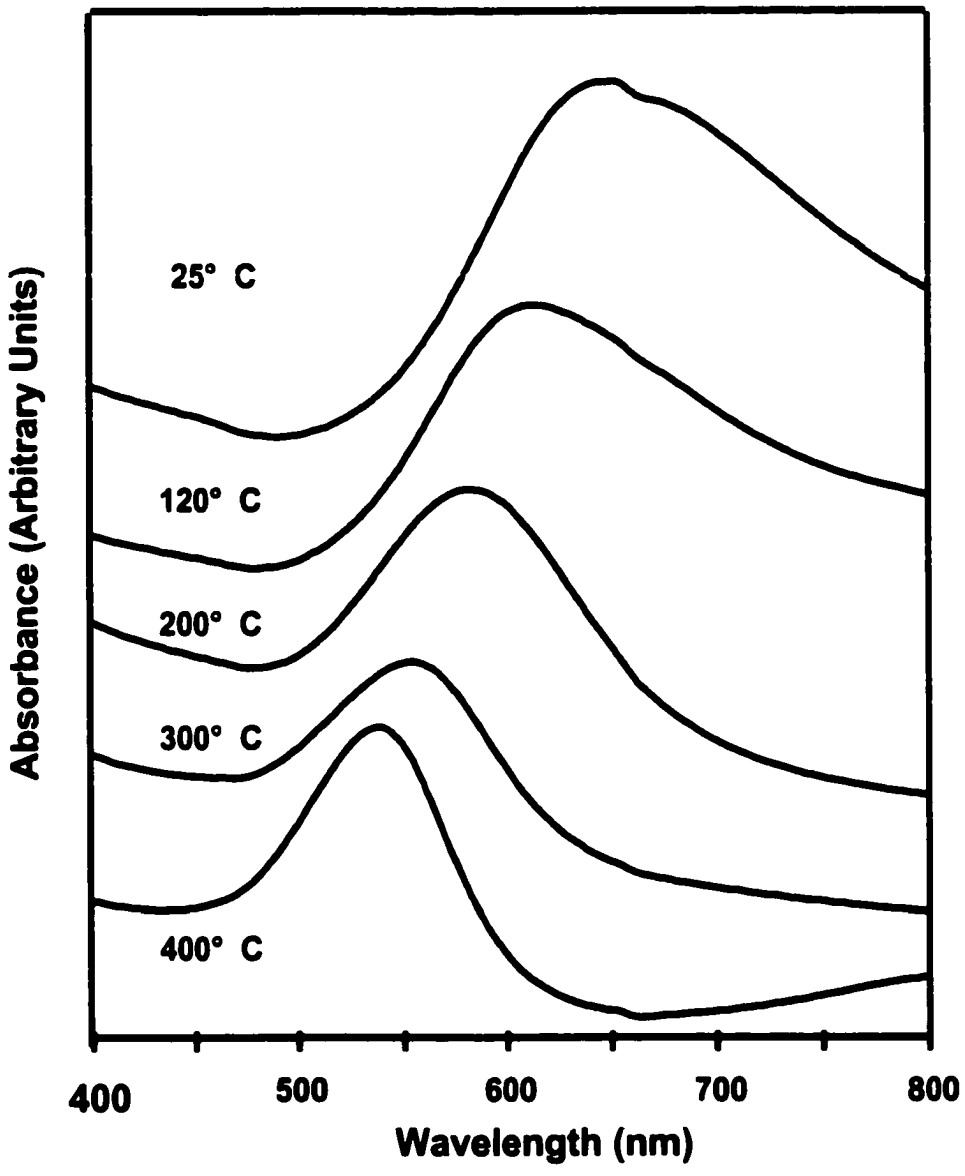

Figure 4.5. Absorption spectra obtained before and after heating the 0.08 C Au nanoparticle/alumina composite. The temperatures used are as indicated.

established that the activation energy for diffusion of Au surface atoms (versus bulk Au) is sufficiently low that these Au atoms have high mobilities at temperatures well below the bulk melting point.[17-20] Such surface diffusion

processes are most likely responsible for the shape changes of the low aspect ratio Au nanoparticles investigated here. It is of interest to note, however, that the aspect ratio = 3 nanoparticles did not change shape upon heating. This is undoubtedly due to the lower surface area of these particles relative to the flake-like particles obtained from the 0.20 and 0.08 C depositions. Furthermore, since these aspect ratio = 3 nanoparticles fill the entire diameter of the pore, there is no free space within the pore for rearrangement of the particle shape. With respect to the changes in the optical properties of these membranes, we have recently reported on the optical properties of Au nanoparticles with aspect ratios less than unity (i.e., oblate or pancake-like particles).[6] We found that as the aspect ratio went from below unity (pancake-like) to unity (sphere-like), there was a blue shift in the λ_{max}. These experimental observations were found to be in agreement with the predictions made via the DMG effective medium theory.[1] These results provide an explanation for the spectral changes observed in this report for the 0.20 and 0.08 C Au nanoparticles. As shown in the TEM images, the as-deposited particles are thin skins and flakes (pancake-like). Prior studies[1] indicate that such particles with aspect ratios from 0.7 to 0.3 would have a λ_{max} between 560 and 670 nm (i.e., the membrane would be blue in appearance). The observed absorption maxima for these as-deposited 0.20 and 0.08 C nanoparticles fall within this range, Figure 4.3. After heating, all these irregularly shaped, flat particles become significantly more spherical, resulting in the aspect ratio of the nanoparticles increasing to *ca.* unity. Our previous studies[1,6] show

that these annealed nanoparticles should have a λ_{max} of *ca.* 540 nm (i.e, the membrane would appear red), which is observed, Figure 4.3.

CONCLUSIONS

We have found that low aspect ratio Au nanoparticles (0.08 and 0.2 C used in the electrodeposition) start out as irregularly shaped skins or flakes of Au within the pores, but after heat treatment at surprisingly low temperatures, they anneal to become dense, roughly spherical particles. The visual color of these membranes started out blue but turned pink after this thermal treatment. In contrast, the 0.4 C nanoparticles (aspect ratio = 3) exhibited no change in optical absorption characteristics, gold particle shape, or electron opacity after exposure to the prescribed heating treatment. This membrane was initially red and did not change color with heating.

REFERENCES FOR CHAPTER 4

1. Hornyak, G. L.; Patrissi, C. J.; Martin, C. R. *J. Phys. Chem. B* **1997**, *101*, 1548-1555.

2. Martin, C. R. *Science* **1994**, *266*, 1961-1966.

3. Foss, C. A., Hornyak, G. L.; Stockert, J. A.; Martin, C. R. *J. Phys. Chem.* **1992**, *96*, 7497.

4. Foss C. A., Tierney, M. J.; Martin, C. R. *J. Phys. Chem.* **1992**, *96*, 9001.

5. Foss C. A., Hornyak, G. L.; Stockert, J. A.; Martin, C. R. *J. Phys. Chem.* **1994**, *98*, 2963.

6. Hornyak, G. L.; Martin, C. R. *Thin Solid Films* **1997**, *303*, 84.

7. Moskovits, M. J.; Routkevitch, D.; Bigioni, T. *J. Phys. Chem.* **1996**, *100*, 14037.

8. Masuda, H.; Kazuyuki, N.; Noboyushi, B. *Thin Solid Films* **1993**, *223*, 1.

9. Huber, C. A.; Huber, T. E.; Sadoqi, M.; Lubin, J. A.; Manelis, S.; Prater, C. B. *Science* **1994**, *263*, 800.

10. Schimmel, T.; Bingler, H.-G.; Franzel, D.; Wokaum, A. *Adv. Mater.* **1994**, *6*, 303.

11. Semin, D. J.; Rowlen, K. L. *Anal. Chem.* **1994**, *66*, 4324.

12. Duyne, R. P. V.; Hulteen, J. C.; Treichel, D. A. *J. Chem. Phys.* **1993**, *99*, 2101.

13. Buffat, P.; Borel, J.-P. *Phys. Rev. A* **1976**, *13*, 2287.

14. Schlegel, V. L.; Cotton, T. M. *Anal. Chem.* **1991**, *63*, 241.

15. Goldstein, A. N.; Echer, C. M. *Science* **1992**, *256*, 1425.

16. Briant, C. L.; Burton, J. J. *J. Chem. Phys.* **1975**, *63*, 2405.

17. Ercolessi, F.; Andreoni, W.; Tosatti, E. *Phys. Rev. Lett.* **1991**, *66*, 911.

18. Gobel, H.; Blanckenhagen, P. v. *Surf. Sci.* **1995**, *331/333*, 885.

19. Bardotti, L.; Jensen, P.; Aires, F. C. S. *Surf. Sci.* **1996**, *367*, 276.

20. Yu, X.; Duxbury, P. M. *Phys. Rev. B* **1995**, *52*, 2102.

CHAPTER 5

CONCLUSIONS

Membrane-based template synthesis is both a precise and general method for the preparation of nanomaterials. The method is general because template membranes are available with a range of pore diameters, compositions, and thicknesses. This makes it suited for a wide variety of studies and applications. In addition, the uniformity of membrane pore diameter permits precise control over particle size and shape, which is important for quantitative studies on nanomaterial morphology / property relationships.

For example, the objective in Chapter 2 was to combine nanomaterials and Li-ion battery research to study the effects of Li-insertion material particle size and surface area on the rate properties of a Li-ion battery electrode. For this work, membrane based template synthesis was combined with a V_2O_5 sol-gel precursor for the preparation of a nanofibrous Li-insertion electrode of crystalline V_2O_5. The resulting electrode contained an array of V_2O_5 nanofibers protruding from a current collector. The results of this study showed that the short Li^+ ion diffusion distances and high V_2O_5 surface area of the nanostructured electrode result in extremely high specific power performance compared to a thin-film control electrode. However, the low volumetric capacity of the nanostructured

electrodes was a disadvantage in the practical sense and was due to the low porosity of the polycarbonate template membrane.

Work toward a practical lithium-insertion electrode (Chapter 3) with both high rate capability and high capacity capitalized on these earlier results, namely, that high surface area and small Li^+ ion diffusion distances result in high rate capability. To prepare insertion electrodes high rate capability and higher volumetric capacity, the template membranes used in Chapter 3 were chemically etched to increase their porosities. The resulting electrodes have higher volumetric and geometric capacities than a more conventional, thin-film electrode at high discharge currents. In addition, the nanostructured electrodes also show better cycling performance than electrodes with lower surface areas. This was an unexpected result which shows another benefit of nanostructured morphology. As a result, the nanoengineered electrodes would make an interesting candidate for Li microbatteries where high power is required.

Finally, the membrane-based template synthesis was used to prepare nanogold/aluminum oxide composites (Chapter 4). This allowed us to prepare nanoscopic gold particles of varying aspect ratios inside a porous aluminum oxide host. Using these gold/alumina composites, we observed how particle size and shape affect the melting characteristics of nanogold. It was found that the low aspect ratio particles start out as flakes of Au within the pores. However, after heat treatment at temperatures well below the melting point of bulk gold, the particles changed shape to become nearly spherical and with higher densities. This was observed with transmission electron microscopy and also optically,

through change in the color of the membrane from blue (before heat treatment) to red (after heating). In contrast, composites with larger aspect ratio particles exhibited no change in color or gold particle shape after exposure to the same heating program. The alumina host was critical to the success of this study because it allowed precise control of gold particle size, it was thermally stable, and optically transparent. In addition the alumina supported the nanoparticles in a rigid framework such that the nanoparticles were easy to deposit (electrochemically) and they remained electrically isolated during the study.